Marchuk Institute of Numerical Mathematics of the Russian Academy of Sciences

As a manuscript

Pavel Aleksandrovich Perezhogin

Stochastic and deterministic subgrid parameterizations of two-dimensional turbulence and their use in ocean circulation models

Specialty 05.13.18 ”—
«Mathematical modeling, numerical methods and software complexes»

Dissertation submitted in partial fulfilment of the requirements for the degree of Candidate of Physical and Mathematical Sciences

Research supervisor:
Doctor of Physical and Mathematical Sciences
Andrey Vasilyevich Glazunov

Moscow ”— 2020

Contents

P.

Introduction

The aim of the dissertation is to improve the reproduction of ocean dynamics by modern numerical models with the help of "subgrid" parameterizations of mesoscale eddies. Below we describe the main properties of oceanic flows in the mesoscale range, their close connection with model problems of quasi-two-dimensional turbulence, and we review approaches to constructing LES (Large Eddy Simulation, [9]) parameterizations of subgrid quasi-two-dimensional turbulence.

Oceanic flows are characterized by a wide range of scales that interact with each other in a nonlinear way. Over a large interval of spatial scales, from the planetary scale (thousands of kilometres) down to the scale equal to the fluid depth (several kilometres), the flows can be considered quasi-two-dimensional (i.e. vertical velocities are small compared with horizontal ones). This property allows the dynamical equations of global ocean models to be formulated under the hydrostatic approximation. Interaction with smaller scales (a few tens of metres) in such models is represented by RANS (Reynolds-Averaged Navier–Stokes, [9]) parameterizations of three-dimensional turbulence in the boundary layers near the surface and the bottom.

Quasi-two-dimensional flows in the ocean differ in their properties depending on the horizontal scale under consideration. On the planetary scale, wave dynamics predominates, characterized by fast inertia–gravity waves which are responsible for the formation of tides and play a key role in the formation of tsunamis. Another manifestation of wave dynamics is the western intensification of currents and the formation of gyres caused by wind stress (the Stommel and Munk problems [10], in which the key role is played by the effect of differential rotation that generates Rossby waves).

These wave motions suppress nonlinear interactions on large scales as follows. From the planetary scale down to about 100 km the slow component of the dynamics (excluding the fast inertia–gravity waves) can be considered geostrophically balanced, i.e. there is an approximate balance between the pressure gradient and the Coriolis force. For these flows one can perform an asymptotic expansion of the dynamical equations in the Rossby number ($Ro = \dfrac{U}{Lf}$, where U and L are characteristic velocity and horizontal scale, f is the Coriolis parameter), the result being the quasi-geostrophic equations [11]. The nonlinear dynamics in these equations depends on the barotropic Rossby deformation radius ($L_0 = \dfrac{\sqrt{gH}}{f}$, where g is the gravitational acceleration and H is the

fluid depth), which for the ocean at mid-latitudes is $L_0 \approx 2000$ km. If the scale of the flow is much smaller than L_0 ($L \ll L_0$), then the single-layer quasi-geostrophic equations are equivalent to the equations of a two-dimensional incompressible fluid; in the opposite case ($L \gg L_0$) the nonlinear interactions become negligible [10]. Rossby waves also weaken nonlinear interactions on large scales, and the associated Rhines scale ($L_{rh} = \sqrt{\frac{U}{\beta}}$, where β is the meridional gradient of the Coriolis parameter) is the scale at which jet currents form [12]. For the mid-latitude ocean the Rhines scale is usually about 300 km and corresponds to the maximum of the spectral density of kinetic energy [13].

The smallest quasi-two-dimensional flows correspond to the submesoscale range (1–100 km, [14]). Such flows are characterized by the predominance of nonlinearity over wave dynamics, which is expressed by large Rossby numbers ($Ro > 1$) and by the breakdown of geostrophic balance. In the submesoscale range an asymptotic expansion in the Rossby number is not possible, which means that such flows cannot be regarded as a two-dimensional incompressible fluid. A decisive role in the dynamics of submesoscale processes can be played by nonlinear interaction with inertia–gravity waves [15].

Thus, in the mid-latitude ocean there exists a range of scales, 100–300 km, in which the dynamics is strongly nonlinear and obeys the laws of geophysical quasi-two-dimensional turbulence [16]. The eddies corresponding to this range are called mesoscale and contain the greater part of the kinetic energy of the ocean [10]. Mesoscale eddies play a significant role in the formation of the general ocean circulation: they perform turbulent mixing of scalars and momentum; they take part in the conversion of available potential energy into kinetic energy, in the formation of nonlinear interactions between scales (the energy cascade), in the formation of decadal variability, and they can accelerate mean currents [17]. Below we describe how geophysical quasi-two-dimensional turbulence is organized, using the single-layer and two-layer quasi-geostrophic equations as examples.

The theoretical description of forced two-dimensional homogeneous turbulence was developed in the works [18—20] (Kraichnan–Leith–Batchelor, KLB). It is assumed that the external forcing has a fixed spatial scale set by the wavenumber k_f, and that there is no dissipation at this scale. In this case two inertial ranges are formed in Fourier space on either side of the forcing scale, along which energy is transferred to large scales and enstrophy to small scales; an expression for the equilibrium kinetic-energy spectrum

is known:

$$E(k) = \begin{cases} C_1 \varepsilon^{2/3} k^{-5/3}, k < k_f & \text{(1а)} \\ C_2 \eta^{2/3} k^{-3}, \quad k > k_f, & \text{(1б)} \end{cases}$$

where an approximate value $C_1 \approx 6$ is known for the constant C_1 [21], and ε and η are the energy and enstrophy fluxes along the corresponding inertial ranges. If one assumes that the external forcing is provided by baroclinic instability, then this model problem is directly relevant to mesoscale turbulence.

A theoretical description of homogeneous two-dimensional turbulence based on the two-layer quasi-geostrophic equations is given in [22]. The flow is decomposed into two components: the vertical average (barotropic mode) and the deviation from the average (baroclinic mode). Owing to the thermal-wind relation [10], the vertical shear of velocity in the geostrophically balanced part of the spectrum is always related to the horizontal density gradient, i.e. to the slope of isopycnal surfaces. Thus the baroclinic mode contains both potential and kinetic energy, and the ratio between them is determined by the internal Rossby deformation radius $L_R = \dfrac{NH}{\pi f}$, where N is the Brunt–Väisälä frequency. At mid-latitudes $L_R = 10$–50 km [13]. In large-scale baroclinic flows, $L > 2\pi L_R$, potential energy predominates, whereas at small scales kinetic energy does. According to the theory, it is assumed that on large scales there is a source of available potential energy caused by the uneven heating of the surface. In addition, there is a sink of kinetic energy on large scales associated with Rayleigh friction. To reach equilibrium, potential energy must be converted into kinetic; however, as shown in [22], direct interaction between the baroclinic and barotropic modes is not possible on large scales because, asymptotically at large scales, the baroclinic mode is advected by the barotropic mode as a passive tracer. In particular, this means that there must exist a direct cascade of baroclinic energy to small scales, which terminates by conversion of the energy into kinetic near the scale $2\pi L_R$. This process is closely connected with baroclinic instability but is not equivalent to it, since the latter is a linear problem. After that, an inverse cascade of kinetic energy is observed with subsequent barotropization of the flow. This process is well described by the single-layer quasi-geostrophic equations. The mechanism just described is the source of energy of mesoscale eddies and is usually considered valid also for the primitive equations of the ocean [13].

The numerical models that participated in the previous Coupled Model Intercomparison Project (CMIP5) had as their ocean component models with a rather coarse horizontal resolution of the order of 1 degree [23]. Such models do not explicitly reproduce

mesoscale eddies on the computational grid and are called “non-eddying”. In models with such a grid step, the effect of subgrid mesoscale eddies on the mean currents and on the temperature and salinity fields is taken into account by means of horizontal mixing parameterizations (e.g. isopycnal diffusion, [24]) and the Gent–McWilliams parameterization [25].

In the current CMIP6 programme the resolution of many ocean models has been increased to $1/4$ degree (see Table A1 in [26]). At such a resolution, mesoscale eddies in mid-latitudes are partially reproduced explicitly. These models are called “eddy-permitting”. However, in eddy-permitting models the eddy dynamics is substantially weakened because of low effective spatial resolution and approximation errors of the numerical schemes. This leads to underestimated values of eddy heat, salt, and momentum transport (in particular, to a weakening of meridional transports), which in turn significantly distorts the mean state of the ocean and the sensitivity of the ocean models to atmospheric forcings. Parameterizations of “subgrid” turbulence designed for coarse models turn out to be inapplicable (see, e.g., [27], where the applicability of the Gent–McWilliams parameterization is discussed). To exploit the available spatial resolution effectively, the development and implementation of fundamentally new “subgrid” closures is required. For example, as the simplest step towards increasing the effective spatial resolution in modern ocean models, it is recommended [27] to increase the order of the dissipation operator in the momentum-evolution equation.

From the point of view of how quasi-two-dimensional turbulence is reproduced, non-eddying ocean models can be regarded as RANS (Reynolds-Averaged Navier–Stokes, [9]) models of quasi-two-dimensional turbulence, in which the effect of mesoscale eddies is represented by the mean Reynolds stress tensor. On the other hand, eddy-permitting models can be regarded as LES (Large Eddy Simulation, [9]) models, that is, they resolve the turbulent eddy field only partially, while the grid scale belongs to the inertial enstrophy range. In both cases an eddy-viscosity model can be used to parameterize the mean effect of explicitly unresolved turbulent fluctuations; however, it has a negative effect on an LES model, since it smooths the explicitly resolved turbulent eddy field near the grid scale, thus lowering the effective resolution of the model.

The present dissertation is devoted to constructing subgrid turbulence models intended for use in ocean models that partially resolve mesoscale eddies, i.e. belonging to the LES class. The way of constructing subgrid closures in LES models is well studied for three-dimensional turbulence [9]; however, the two-dimensional case has received

much less attention in the literature. In particular, the LES approach must take into account the essentially nonlocal (in Fourier space) nature of the interactions and the possibility of energy transfer from small scales to large ones: as shown in [28; 29], the most energetically important process in two-dimensional turbulence—the inverse cascade of energy—is sustained by interactions with Fourier modes located near the forcing scale. The presence of numerical discretizations of advection in actual computations is a separate difficulty when constructing subgrid closures [30]: the discretization plays the role of an additional "filtering" of the equations of motion.

Numerical discretizations can play a special role in the dynamics of a two-dimensional fluid at finite spatial resolution. The equations of an ideal two-dimensional fluid possess a wide class of conservation laws: momentum, energy, vorticity, enstrophy, as well as an infinite number of Casimirs (arbitrary powers of vorticity, [31]). According to the MRS theory (Miller–Robert–Sommeria, [32]), the influence of the conservation laws for the Casimirs should manifest itself in the formation of large-scale coherent structures in an ideal fluid. Numerical discretizations of advection can exactly conserve various sets of the above conservation laws. The Arakawa schemes [33] make it possible to conserve the first moments of the solution and various sets of second moments. There also exist discretizations that allow the entire set of Casimirs to be conserved at the discrete level: the Lagrangian "Hamiltonian particle-mesh method" [34] and a special form of discrete equations in Fourier space [35]. In [36; 37] it is shown that the statistically equilibrium states of finite-dimensional approximations of the equations of an ideal two-dimensional fluid depend on the presence of the conservation law for the third Casimir (vorticity cubed). In [38] the role of discrete analogues of the conservation laws of the equations of an ideal two-dimensional fluid is shown for the problem of data assimilation.

In the present dissertation we assume that the role of numerical discretizations of advection must also be taken into account when constructing subgrid LES parameterizations. In particular, due to the nonlinear nature of the equations, numerical errors can be present on all scales. Aliasing errors provide an example. Even if numerical errors are concentrated at small scales, then, as pointed out in [39], these errors can over time be transferred along the spectrum to large scales by nonlinear interactions. In the case when the time of such a transfer is shorter than the characteristic time of the energy-significant processes, the energy distribution along the spectrum can be disturbed. The presence or absence of conservation laws in the advection scheme can affect the form of the numerical errors and their distribution across scales.

In what follows we will call “subgrid forces” the total contribution of the scales unresolved by the grid together with the forces that have to be introduced to correct the approximation errors of the numerical scheme. To construct the subgrid forces explicitly, one must perform a computation at high spatial resolution, separate the scales into resolved and unresolved by means of spatial filtering, and compute their interaction, as done in [40] for three-dimensional turbulence and in [41] for two-dimensional. The way of accounting for the numerical discretizations of advection when constructing the subgrid forces is given in [30]. It is also possible to construct subgrid forces in the case when the spatial and temporal discretization cannot be performed independently: in [42] subgrid forces are constructed for a semi-Lagrangian method. Statistical characteristics of the subgrid forces can be constructed without performing a high-resolution computation by using EDQNM-type (Eddy-Damped Quasi-Normal Markovian) models for the subgrid scales [43].

There are many approaches to constructing LES parameterizations in two-dimensional turbulence; however, the majority of parameterizations have not yet been tested in modern ocean models because of algorithmic complexity or because of the large number of assumptions made (e.g. the assumption of homogeneous turbulence). We give an overview of the most modern parameterizations of two-dimensional and three-dimensional subgrid turbulence, while in the dissertation we will focus on the simplest algorithms.

The simplest models describing the subgrid forces have the form $(-1)^{n+1}\Delta^n\omega$ and are called eddy-viscosity models. Such models introduce enstrophy dissipation at the smallest scales and prevent its accumulation at the grid scale. However, these models have an obvious drawback: together with enstrophy, energy is also dissipated, although according to KLB theory there is no direct cascade of energy. The Scale-Similarity Model (SSM, [44]) is known for having, unlike dissipative models, a high correlation with the subgrid forces [45]. The result of expanding the scale-similarity model in a Taylor series is the nonlinear gradient model [45]. In [46] it is shown that such a model provides a high correlation with the subgrid forces in quasi-two-dimensional turbulence. It is usually assumed that SSM models and their analogues do not provide enough dissipation, so they cannot be used without additional regularization [45]. It is possible to use SSM models together with eddy-viscosity models (mixed models, [45]). In [47] an attempt is made to regularize the scale-similarity model by projecting it onto dissipative directions. A similar technique was studied for two-dimensional turbulence [48]. It is also possible to estimate the eddy-viscosity co-

efficient from the values of the momentum-flux tensor for the scale-similarity model (dynamic models, [45]). In recent works dynamic models have been investigated in the quasi-geostrophic equations [49] and in the primitive equations of the ocean [50]. The main problem of using dynamic models is the large variance of the computed eddy-viscosity coefficient. Thus, [49] uses averaging over space (i.e. information about the local properties of turbulence is lost), and in [50] the eddy-viscosity coefficient is assumed to be positive. In this way information about the backward propagation of energy from subgrid scales, which should play a decisive role in quasi-two-dimensional turbulence, is lost. The highest correlation with the subgrid forces can be achieved by using machine-learning methods and neural networks. Such models were constructed for three-dimensional turbulence in [51] and for two-dimensional in [52]. The main problem remains, as for scale-similarity models, the numerical stability of the algorithm. In both cases a projection onto dissipative directions was used. An additional problem of such parameterizations is poor generalization: the weights of the neurons must be updated when the resolution or the model problem is changed. There are also models in which "subgrid" eddies are reconstructed on the coarse grid by means of a defiltering procedure ("Deconvolution models", [53]). Such a procedure was carried out for two-dimensional turbulence both approximately ("Approximate deconvolution model", [54]) and with the help of neural networks [55]. The main problem of such models is again numerical stability: it is necessary to use additional regularization in the form of eddy viscosity.

As follows from the above review, the construction of subgrid models having a high correlation with the subgrid forces is usually accompanied by problems of numerical stability. There exists another way of constructing parameterizations—the statistical one. In this case the physical properties of subgrid turbulence are taken into account, but correlation with the subgrid forces is not guaranteed. In [56], within the three-layer quasi-geostrophic equations, a stochastic model of the subgrid forces is constructed which reproduces the spatial correlation depending on the spatial point, takes into account the vertical correlation of the tendency and reproduces the characteristic shape of the autocorrelation function (in time). It is shown that the most important characteristic of the temporal autocorrelation function is its integral, which determines the amount of returned energy. Another important characteristic is the negative spatial correlation of the stochastic tendency, neglect of which enhances the mean currents. In [57] it is shown that the use of a long series of subgrid forces (but not correlated with the solution) allows the decadal variability of the coarse model to be recovered.

In [58] (MTV, “Majda–Timofeyev–Vanden”) it was proposed to replace the nonlinear interaction of the unresolved scales with themselves by a stochastic process, which, under the assumption of a separation of time scales for the resolved and unresolved flows, makes it possible to obtain stochastic equations for the resolved scales. The drawback of this approach is an additional nonlinear interaction among the resolved flows that engages all basis functions involved in the expansion. Constructing such a parameterization is possible only for a small number of basis functions. In [59] a stochastic “superparameterization” of the unresolved flows is proposed. As in the previous work, the nonlinear interaction of the unresolved scales with themselves is replaced by a stochastic process. The difference is that a covariance matrix is introduced for the subgrid scales, for which the equilibrium spectral density of kinetic energy corresponding to the enstrophy range is also used. The advantage of this approach is the possibility to statistically describe the baroclinic instability that is not resolved on the coarse-model grid.

In [60] it is proposed to model the dynamics of finite-dimensional Hamiltonian systems by a stochastic perturbation of the coarse model along a constant-energy surface, which can be carried out by means of multiplicative noise. This approach was extended to the quasi-geostrophic equations in [61; 62]. A drawback of the approach is that the theory does not provide recommendations on the choice of the spatial correlation of the noise; in particular, in the most recent works, noises constructed on the first EOF (“Empirical Orthogonal Function”) and DMD (“Dynamic Mode Decomposition”) vectors are investigated.

In [63] the equation of Lagrangian transport of potential vorticity is considered. The assumption is made that the unresolved scales can perturb the trajectory of a Lagrangian particle, and that this process can be described by introducing a stochastic advection field. Such models belong to the “stochastic advection” class and at present are mainly being developed to correctly reproduce the characteristics of the ensemble of solutions.

In [64] it is proposed to tune the parameters of a stochastic parameterization so that the first and second moments of the solution are correctly reproduced at every point in space. To this end an iterative process is organized, where each iteration is a run of the model for several years with subsequent averaging of statistical characteristics. The iterative procedure makes it possible to find the noise variance and the constant forcing as functions of the coordinates. This work shows that it is possible to find an optimal parameterization, but its search is very expensive.

In [65] it is shown that if the Laplace operator is applied to the Lagrangian derivative of the potential vorticity, the resulting expression will have a high correlation with the subgrid forces. For each value of this expression a conditional distribution of the subgrid forces is constructed. The resulting parameterization, consisting of a deterministic and a stochastic part, was tested in the three-layer quasi-geostrophic equations in [66]. It is shown that both the deterministic and the stochastic additions improve the reproduction of the mean flow. The deterministic part of the parameterization can be expanded in a series in powers of the Laplace operator [66].

The simplest variant of subgrid models that restores the energy balance in the coarse model in a statistical way is the kinetic-energy backscatter (KEB, [67]) class of models. The parameters of such parameterizations can be estimated from the spectral characteristics of the subgrid forces [41], or in a phenomenological way—by assuming energy conservation of the total subgrid model ("energetically consistent backscatter", [68]). In the present dissertation we mainly consider parameterizations belonging to the KEB class.

One of the possible ways of modelling KEB is stochastic excitation of the resolved scales, "stochastic backscatter" [69]. The first works on stochastic parameterizations were carried out for three-dimensional turbulence [40; 67; 70]. In LES models of three-dimensional small-scale turbulence in the atmospheric boundary layer, stochastic subgrid forcing was first applied in [71]. Stochastic parameterizations in LES are one of the possible ways to improve the reproduction of first and second moments near the surface, where the model has a deliberately coarser grid than is needed for an explicit description of the part of the inertial range with the direct energy cascade [72; 73]. Later, stochastic parameterizations were adapted to quasi-two-dimensional flows [41; 43; 74; 75] on the basis of simplified quasi-geostrophic equations. In [76; 77] stochastic parameterizations were used to broaden the ensemble in an ensemble weather-forecasting model. In particular, the use of such parameterizations makes it possible to recover the spectral density of kinetic energy of atmospheric turbulence, which is characterized by a $k^{-5/3}$ spectral slope in the mesoscale range.

In [68] it was proposed to enhance mesoscale eddies in ocean models by combining a KEB parameterization with a parameterization of turbulent viscosity that uses a Laplace operator raised to a high power. In the recent works [78] and [79] KEB parameterizations are applied to model problems of atmospheric dynamics (Held–Suarez test [80]) and ocean dynamics (in the "zonal channel" approximation), respectively. In a global ocean model the KEB parameterization was investigated for the first time in

2020 [81]. KEB parameterizations are capable of improving the mean state of the model solution [68; 82; 83], the kinetic-energy spectrum [68; 82], the eddy heat flux [84], and the global thermohaline circulation [82]. Most of the works mentioned above were carried out with simplified numerical models of the dynamics of a two-dimensional and quasi-two-dimensional fluid. The intrinsic dynamics of such idealized models possesses the properties of large-scale two-dimensional and quasi-geostrophic turbulence characteristic of the ocean; however, many processes specific to the real ocean are not taken into account.

At present it is appropriate, using the accumulated experience, to adapt KEB parameterizations to ocean circulation models. On this path there is a number of problems. Parameterizations constructed for the quasi-geostrophic equations, by definition, modify only the geostrophically balanced part of the flow. As noted in [13; 83], to construct analogous parameterizations in models based on the primitive equations one must modify not only the momentum equation but also the equations for the active tracers, and in a consistent way. Another open question concerns the vertical structure of the parameterizations. Thus, in [68; 82; 84] the parameterizations are independent of the vertical coordinate (the layer number), while in [77—79] the parameters of the parameterization vary with height.

For real-ocean models the construction of complex subgrid parameterizations based on the a priori analysis of the subgrid forces presents a certain difficulty, since the statistical properties of the modelled quasi-two-dimensional turbulence vary across space, depth and seasons; the flows consist of both an eddy component and mean currents; the definition of the subgrid forces will inevitably include baroclinic processes, which possess different properties depending on the scale (mesoscale and submesoscale turbulence); there are peculiarities in the near-wall region (western intensification of the currents); and subgrid models based on the Fourier transform are expensive and difficult to implement in practice. Nevertheless, it is possible to construct a kinetic-energy generation spectrum produced by the subgrid forces averaged over the domain, depth and seasons. Although such a characteristic does not take into account many inhomogeneities of the eddy field, it makes it possible to study how the scale and the amount of returned energy in the studied parameterizations correlate with those in the subgrid forces. Such an analysis is carried out in the **sixth** chapter of the dissertation for the NEMO ocean model [85] in the Double Gyre configuration.

In view of the growth of computer power, the resolution of ocean models will steadily increase. Nevertheless, the results of the present work, aimed at improving

the reproduction of mesoscale eddies, will remain in demand. Mesoscale eddies have a horizontal size proportional to the internal Rossby deformation radius, which decreases with increasing latitude. Thus, KEB parameterizations will be useful for modelling the ocean at high latitudes and for regional modelling of the Arctic. Consequently, the development of KEB parameterizations for subgrid quasi-two-dimensional turbulence is a **topical task**.

The aim of the dissertation is to improve the quality of reproduction of ocean dynamics by modern numerical models by means of subgrid parameterizations of mesoscale eddies.

To achieve the aim formulated in the work, the following **tasks** were solved. In the **first** and **second** chapters of the dissertation the role of the numerical approximations of advection in the formation of large-scale coherent structures in an ideal two-dimensional fluid and of the inverse energy cascade in forced two-dimensional turbulence is investigated. In the **third** chapter an analysis of the subgrid forces in the problem of modelling the inverse energy cascade is carried out, and scheme-dependent KEB parameterizations are constructed. It is shown that the use of KEB parameterizations allows the inverse energy cascade to be recovered. Furthermore, second-order finite-difference schemes possess similar spectral characteristics of the subgrid forces. For this reason, in the remaining three chapters only one second-order scheme is studied. In the **fourth** chapter the role of subgrid parameterizations in the problem of barotropic instability of a jet flow is investigated. In the **fifth** chapter KEB parameterizations are studied in the NEMO ocean model [85] in the Double Gyre configuration. In the **sixth** chapter, in the Double Gyre configuration, a spectral analysis is carried out of the influx of kinetic energy from the subgrid forces, and a comparison is performed with the influxes produced by the constructed subgrid parameterizations.

The scientific novelty consists in the following original results:

1. The role of discrete analogues of conservation laws and of various approximations of the equations of an ideal two-dimensional fluid in the formation of the inverse energy cascade is demonstrated.
2. It is proposed to model KEB by means of the scale-similarity model. However, this result has not yet found application in the NEMO ocean model.
3. The role of subgrid closures in the formation of the development of the instability of a barotropic jet flow is demonstrated in the statistical sense.
4. A comparison between stochastic and deterministic approaches to modelling KEB in the primitive equations of the ocean is carried out.

5. A spectral analysis of the subgrid forces in the primitive equations of the ocean is carried out, on the basis of which it is shown that the scale of backward redistribution of kinetic energy does not depend on the resolution of the coarse model and is determined by the scale of blocking of the inverse energy cascade.

Practical significance. The application of specialized KEB parameterizations will make it possible to increase the effective resolution of the simulated quasi-two-dimensional turbulence, which in turn will make it possible to perform long-time climate simulations with insignificant expenditure of computational resources.

Statements to be defended:

1. The role of discrete analogues of the conservation laws inherent in the equations of an ideal two-dimensional fluid in the formation of the inverse energy cascade is established. The absence of a conservation law for the integral vorticity leads to a spurious energy cascade to the scale set by the size of the domain, while the absence of a conservation law for enstrophy leads to a weakening of the inverse energy cascade.
2. The scale-similarity model reproduces the spectral influx of energy from the subgrid forces. For this reason it can be used as a KEB parameterization for recovering the inverse energy cascade, provided that the tendency is filtered in the small-scale dissipative range.
3. It is shown that subgrid parameterizations are able to accelerate the transition to a turbulent flow regime in the problem of modelling barotropic instability of a jet flow. The mechanism by which the subgrid models work is different: a negative-viscosity parameterization prevents smoothing of the mean flow; the scale-similarity model modifies the linearized system and increases the growth rates of the unstable modes; the stochastic parameterization excites the unstable modes.
4. It is shown that modelling of KEB in the primitive equations of the ocean can be carried out both in a stochastic and in a deterministic way. Both parameterizations recover the level of eddy energy, the eddy meridional heat flux, and the meridional overturning circulation.
5. It is shown that the scale of energy return by the subgrid forces in the Double Gyre problem in the NEMO model does not depend on the resolution of the coarse model and is determined by the scale of blocking of the inverse energy cascade. The amount of returned energy (relative to the dissipated one) de-

creases with increasing resolution, which is due to the gradual resolution on the computational grid of the mesoscale and submesoscale eddies.

Approbation of the work. The main results of the work were reported at the following international and Russian conferences: 58th, 59th, 60th, 61st, 62nd MIPT Scientific Conferences, Moscow, Russia, 2015–2019; International Young Scientists' School and Conference on Computational Information Technologies for Environmental Sciences: "CITES-2017", 2017, and "CITES-2019", 2019, Moscow, Russia; 21st All-Russian School-Conference of Young Scientists "Composition of the Atmosphere. Atmospheric Electricity. Climatic Processes" (SatEP-2017), Borok, Russia, 2017; International Symposium Topical Problems of Nonlinear Wave Physics (NWP-2017), Nizhny Novgorod, Russia, 2017; International Union of Geodesy and Geophysics 32nd IUGG Conference on Mathematical Geophysics, Nizhny Novgorod, Russia, 2018; International conference dedicated to the 100th anniversary of the birth of Academician A.M. Obukhov "Turbulence, Atmospheric and Climate Dynamics", Moscow, Russia, 2018; All-Russian forum Supercomputer Technologies and Artificial Intelligence, Nizhny Novgorod, Russia, 2018; International conference "Topical Problems of Computational and Applied Mathematics 2019" (APCAM-2019), Novosibirsk, Russia, 2019; Winter school "Physics and Mathematics of Turbulent flows at different scales", Les Houches, France, 2019; Summer school "Mathematics for Climate and the Environment", Cargèse, Corsica, France, 2019; Workshop on Novel Approaches in Observations and Modeling of Geophysical Turbulence, Moscow, 2019; EGU General Assembly 2020, Vienna, Austria, 2020.

Personal contribution. The results presented in the dissertation were obtained personally by the author. The author took part both in the formulation of the problems and in the performance of numerical experiments and in the interpretation of the results.

Publications. The main results on the subject of the dissertation are presented in 8 printed publications [1—8], 7 of which [1—7] were published in journals recommended by the VAK (Higher Attestation Commission of the Russian Federation).

Volume and structure of the work. The dissertation consists of an introduction, six chapters, a conclusion and four appendices. The total volume of the dissertation is 139 pages, including 49 figures and 9 tables. The reference list contains 155 entries.

The work was supported by grants from the Russian Science Foundation (14-27-00126, 17-17-01210), grants from the Russian Foundation for Basic Research (19-35-90023, 18-05-60184, 16–55–12015, 18-05-60126), the Presidential grant NSh-9836.2016.5 and by the research centre "Moscow Centre for Fundamental and Applied

Mathematics" (under financial support of the Ministry of Science and Higher Education of the Russian Federation, agreement No. 075-15-2019-1624).

Chapter 1. Investigation of coherent structures in an ideal (inviscid) fluid and in forced turbulence

The problem of studying two-dimensional turbulence is very important in geophysical fluid dynamics, since the atmosphere and the ocean are quasi-two-dimensional. In geophysical fluid dynamics there are two key problems: weather forecasting and climate-change prediction. From the mathematical point of view, the first problem is connected with the investigation of the behaviour of the solution of the system on a finite time interval, and to justify it global solvability theorems and convergence theorems for the solutions of finite-dimensional approximations to the solution of the differential problem are quite sufficient. For the two-dimensional equations of both the ideal and the viscous fluid such theorems exist [86—89]. However, the convergence constants, if they are determined, as a rule depend exponentially on the time interval on which the problem is studied, and as this interval tends to infinity these theorems become meaningless. Such situations arise when we study problems of climate modelling on an arbitrarily large time interval. Consequently, the problem of studying the dynamics of a two-dimensional fluid on an arbitrarily large time interval is a key one in climate theory. This dynamics is of course different for a viscous fluid (dynamics on the attractor) and for an ideal fluid. In the asymptotic case, when one investigates the dynamics of a two-dimensional fluid at very small viscosity (so-called decaying turbulence), the two-dimensional fluid on sufficiently large time intervals behaves as an ideal one (see, e.g., [1; 2; 90; 91]).

In real problems of weather forecasting and climate theory we deal with a quasi-two-dimensional fluid in the presence of forcing and dissipation, and the problems of the ideal two-dimensional fluid from this point of view seem quite academic. However, this is far from being so if one bears in mind that, for example, in modelled distributions of energy along the spectrum there are the so-called inertial intervals where dissipation and forcing are small and the fluid behaves as an ideal one [18]. Characteristic features of the behaviour of an ideal fluid can be observed also in other characteristics of a viscous fluid, which we shall discuss below. From this point of view, studying the dynamics of an ideal fluid is a problem that is not only academic but also essentially useful in practice. Since the practical problems of weather forecasting and climate theory can be solved only numerically, the problem of investigating the properties of finite-dimensional approximations of the original differential problem appears very

important [92—95]. In the investigation of approximations of the equations of an ideal two-dimensional fluid a natural condition (besides the conditions of approximation and stability) is that they belong to the class of systems of hydrodynamic type. Recall that in [96] A.M. Obukhov defined the finite-dimensional system

$$\frac{du_i}{dt} = F_i(u),\ u|_{t=0} = u^0 \tag{1.1}$$

with respect to the unknown $u = [u_1, u_2, ..., u_n]$ as a system of hydrodynamic type if it satisfies three requirements:

1. The system (1.1) is quadratically nonlinear.
2. The phase flow is incompressible:

$$\sum_i \frac{\partial F_i}{\partial u_i} = 0. \tag{1.2}$$

3. The system has at least one quadratic conservation law $(Su, u) = \text{const}$, where S is a positive-definite symmetric matrix.

The task of the present chapter is to investigate the statistical properties of finite-dimensional approximations of the equations describing the dynamics of an ideal two-dimensional fluid that belong to the class of systems of hydrodynamic type according to the above definition.

Before proceeding to the specific formulation of this problem, let us briefly recall the fundamental properties of the systems of equations describing the dynamics of a two-dimensional ideal fluid. We write the original equations of the dynamics of a two-dimensional ideal incompressible fluid in terms of vorticity and streamfunction:

$$\frac{\partial \omega}{\partial t} + J(\psi, \omega) = 0, \tag{1.3}$$

here $\omega = \triangle\psi$ is the vorticity, ψ is the streamfunction, $J(\psi,\omega) = -\frac{\partial \psi}{\partial y}\frac{\partial \omega}{\partial x} + \frac{\partial \psi}{\partial x}\frac{\partial \omega}{\partial y}$ is the Jacobian. We consider the system (1.3) in a doubly periodic channel D in Cartesian coordinates, so that $\int_D \omega dD = 0$. It is well known [97] that the system (1.3) has the energy conservation law

$$E = -\frac{1}{2}\int_D \psi\omega dD = \text{const} \tag{1.4}$$

and an infinite number of invariants (Casimirs) of the form

$$\int_D F(\omega) dD = \text{const}. \tag{1.5}$$

If we set $F(\omega) = \frac{1}{2}\omega^2$, then we have the enstrophy conservation law

$$\overline{\omega^2} = \frac{1}{2}\int_D \omega^2 dD = \text{const.} \tag{1.6}$$

From (1.4) and (1.6) there follows the conservation law for the energy-averaged squared wavenumber:

$$\overline{k^2} = \frac{\overline{\omega^2}}{E} = \text{const.} \tag{1.7}$$

The infinite number of conservation laws (1.5) is equivalent to the conservation of the area distribution of vorticity [98], given by the formula

$$\frac{dD}{D} = \rho(\omega)d\omega, \tag{1.8}$$

i.e. $\rho(\omega)$ is an invariant. If we introduce the notion of information entropy [99], then it follows that the entropy

$$S = -\int_{-\infty}^{+\infty} \rho \ln \rho \; d\omega, \;\; \rho \equiv \rho(\omega) \tag{1.9}$$

is also invariant.

Since any finite-dimensional approximation, even one belonging to the class of systems of hydrodynamic type, cannot have an infinite number of invariants, the investigation of the behaviour of the area distribution density of vorticity $\rho(\omega)$ appears to be a very interesting and promising problem not only for the ideal fluid but also in the case of the real atmosphere [99].

Below we shall need one more definition of entropy [100]:

$$S = -\int_D dD \int_{-\infty}^{+\infty} \rho \ln \rho \; d\omega, \;\; \rho \equiv \rho(x,y,\omega), \tag{1.10}$$

where $\rho(x,y,\omega)$ is used to define the ensemble in the Miller–Robert–Sommeria (MRS) mean-field theory [32; 101] and denotes the area distribution depending on the point in space. A review of MRS theory can be found in [1; 100].

We now turn to other characteristics of the quasi-equilibrium state of the ideal two-dimensional fluid. These characteristics have been studied by various authors [90; 91; 93; 95]. According to MRS theory, the energy in the quasi-equilibrium state is concentrated in a large-scale coherent structure determined by the stationary solution of the system (1.3), see [100]:

$$\overline{\omega} = F(\overline{\psi}), \tag{1.11}$$

where the overbar denotes ensemble averaging, which makes it possible to dispense with the explicit description of the contribution of small-scale non-stationary flows. If one uses the variational principle of maximizing the entropy (1.10) at given energy E and enstrophy $\overline{\omega^2}$, then the function F will be linear with a slope corresponding to the smallest in absolute value eigenvalue of the Laplace operator $\lambda_{\min}$ [100]:

$$\triangle\psi_1 = -|\lambda_{\min}|\,\psi_1. \tag{1.12}$$

Since a sufficient condition for the stability of the stationary solution is [97]

$$\frac{\partial F}{\partial\overline{\psi}} > -|\lambda_{\min}|,$$

we can conclude that the stability criterion of the resulting stationary solution (1.12) corresponds in this case to the limiting point of the stability test.

Thus, the main problems considered in the present work are:

1. Investigation of the area distribution of vorticity reproduced by various approximations of the equations of the dynamics of an ideal two-dimensional incompressible fluid that belong to the class of systems of hydrodynamic type.
2. Investigation of the quasi-equilibrium coherent structures reproduced by these finite-dimensional approximations.
3. Comparison of these coherent structures with the structures arising in a viscous fluid with random forcing.

1.1 Difference schemes and methods of solution

As the subject of investigation we take three difference schemes approximating the equations (1.3) and belonging to the class of systems of hydrodynamic type. The schemes are constructed on the basis of different representations of the Jacobian $J(\psi,\omega)$. It is well known that the Jacobian J can be written in three representations:

$$J_1 = \frac{\partial\psi}{\partial x}\frac{\partial\omega}{\partial y} - \frac{\partial\psi}{\partial y}\frac{\partial\omega}{\partial x} \quad \text{– advective form,} \tag{1.13}$$

$$J_2 = \frac{\partial}{\partial y}\left(\frac{\partial\psi}{\partial x}\omega\right) - \frac{\partial}{\partial x}\left(\frac{\partial\psi}{\partial y}\omega\right) \text{ – first divergent form,} \tag{1.14}$$

$$J_3 = \frac{\partial}{\partial x}\left(\frac{\partial\omega}{\partial y}\psi\right) - \frac{\partial}{\partial y}\left(\frac{\partial\omega}{\partial x}\psi\right) \text{ – second divergent form.} \tag{1.15}$$

On the basis of these three forms one can, using symmetric approximations of derivatives on a uniform grid, construct spatial approximations that conserve enstrophy, energy, or both energy and enstrophy (the Arakawa scheme [33]). The incompressibility of the phase flow (1.2) for the given approximations is proven in [94].
The scheme conserving energy **E** has the form

$$J^h = \frac{1}{2}\left[J_1^h(\psi_h,\omega_h) + J_3^h(\psi_h,\omega_h)\right], \tag{1.16}$$

where J_1^h, J_3^h are the approximations of J_1 and J_3.
The scheme conserving enstrophy **Z**:

$$J^h = \frac{1}{2}\left[J_1^h(\psi_h,\omega_h) + J_2^h(\psi_h,\omega_h)\right], \tag{1.17}$$

and the scheme conserving energy and enstrophy **ZE**:

$$J^h = \frac{1}{3}\left[J_1^h(\psi_h,\omega_h) + J_2^h(\psi_h,\omega_h)) + J_3^h(\psi_h,\omega_h)\right]. \tag{1.18}$$

If for the approximation of equation (1.3) one uses the Crank–Nicolson scheme together with the spatial approximations (1.16), (1.17), (1.18), then all the above-listed conservation laws are satisfied at every time step [94]. The resulting time-integration procedure consists in solving a system of nonlinear algebraic equations with quadratic nonlinearity of the following form:

$$\frac{\omega_h^{n+1}-\omega_h^n}{\Delta t} + J^h\left(\frac{\psi_h^{n+1}+\psi_h^n}{2}, \frac{\omega_h^{n+1}+\omega_h^n}{2}\right) = 0, \tag{1.19}$$

where n denotes the time-layer index. To find the numerical solution of this system the method of simple iterations is used, described in detail in [1]. The number of iterations is equal to 5, and this ensures conservation of the quadratic invariants with a relative accuracy from 10^{-4} to 10^{-3}.

1.2 Results of numerical experiments with the schemes approximating the equations of the ideal fluid

Before proceeding to the discussion of the results of the numerical experiments, we make several remarks.

1. In the case of infinite-dimensional spaces (differential formulation of the problem), we have an analogue of the embedding theorem [97]:

$$E = -\frac{1}{2}(\psi,\omega) \leqslant \frac{1}{|\lambda_{\min}|}\frac{(\omega,\omega)}{2} \equiv \frac{1}{|\lambda_{\min}|}\,\overline{\omega^2},$$

where $\lambda_{\min}$ is the smallest in absolute value eigenvalue of the Laplace operator. For finite-dimensional space, in the case of a uniform square grid, the relations between energy and enstrophy can be obtained as follows. Let

$$E_h = -\frac{1}{2}\big(\psi_h,\omega_h\big)_h,\ \overline{\omega_h^2} = \frac{1}{2}\big(\omega_h,\omega_h\big)_h,$$

where $(\cdot,\cdot)_h$ is the scalar product in the finite-dimensional space. Let S_h be a symmetric negative-definite approximation of the Laplace operator. Consider the pair of subspaces orthogonal to a constant, $(\omega_h,1)_h = 0$ and $(\psi_h,1)_h = 0$, on which S_h acts bijectively. Then $\omega_h = S_h\psi_h$ and $\psi_h = S_h^{-1}\omega_h$. From here we obtain the two-sided estimate of the energy level:

$$\frac{1}{|\lambda^h_{\max}|}\,\overline{\omega_h^2} \leqslant E_h \leqslant \frac{1}{|\lambda^h_{\min}|}\,\overline{\omega_h^2}, \tag{1.20}$$

where the eigenvalues of the matrix S_h depend on the parameters of the problem as follows:

$$|\lambda^h_{\max}| = \frac{\alpha}{h^2},\ \alpha = \text{const},\ h - \text{grid step}$$
$$|\lambda^h_{\min}| = \beta,\ \beta - \text{constant determined by the size of the domain.}$$

Thus, if we consider a scheme that conserves only enstrophy, then the energy will be bounded above by a constant independent of the grid step:

$$E_h \leqslant \frac{1}{\beta}\,\overline{\omega_h^2}. \tag{1.21}$$

Moreover, the generation of energy, if it occurs, takes place at large scales, since the energy-averaged squared wavenumber $\overline{k_h^2} = \frac{\overline{\omega_h^2}}{E_h}$ should in this case decrease. In addition, an almost complete dissipation of energy is possible [94].

If a scheme conserving only energy is considered, then the enstrophy will satisfy

$$\overline{\omega_h^2} \leqslant \frac{\alpha}{h^2}E_h. \tag{1.22}$$

This relation means that the energy-averaged squared wavenumber $\overline{k_h^2} = \frac{\overline{\omega_h^2}}{E_h} \leqslant \frac{\alpha}{h^2}$ can grow without bound as $h \to 0$, i.e. in this scheme a cascade of energy to high wavenumbers is possible.

2. The relations corresponding to the smallest in absolute value eigenvalue of the Laplace operator acting on functions defined on a doubly periodic channel are degenerate, since to this eigenvalue there corresponds an eigensubspace of dimension 2. This means that the form of the coherent structure forming in this subspace and satisfying relation (1.12) is not uniquely determined.
3. Generally speaking, the results of the quasi-equilibrium distributions depend on the configuration of the initial state, in particular on the mean wavenumber [92]. If the initial state is chosen such that $\overline{k^2} = \overline{\omega^2}/E \gg |\lambda_{\min}(\triangle)|$, then, as shown in [1; 94; 95], the quasi-equilibrium area distributions for systems of hydrodynamic type will be determined by the fluctuations around the mean state. This distribution should be close to the normal one, since the entropy (1.9) is maximized on the normal distribution in the presence of a quadratic invariant (see, e.g., [102]).
4. Convergence to the quasi-equilibrium state in a system of hydrodynamic type must take place provided that the definition of convergence includes a "filtering", e.g. spatial averaging $\overline{\omega}$ (we shall average over cells consisting of $n \times n$ grid points), or time averaging $\langle\omega\rangle = \frac{1}{T}\int_0^T \omega dt$ (Cesàro convergence). A detailed theory of Cesàro convergence is given in [103]. In our numerical experiments we shall always specify which procedure is used.

Numerical experiments for all schemes (E, Z, ZE) were carried out with the following parameters. The doubly periodic channel D has size $[0,2\pi) \times [0,2\pi)$, the resolution of the computational grid is 512×512 points. The initial vorticity field consists of 8×8 square patches on which the vorticity is constant and takes randomly one of the values $\{-1+a, -1+3a, ..., 1-a\}, a = 1/64$, each value being chosen exactly once. Similar initial data were used in [104] to simplify the theoretical analysis of the equilibrium states and are called "vortex patches". The mean squared wavenumber for such initial data equals $\overline{k^2} = \overline{\omega^2}/E = 4.4 > |\lambda_{\min}(\triangle)| = 1$. The computation was carried out over a long time interval $t \in (0,50000)$. Full statistical equilibrium for all schemes is reached no later than at the moment $t \approx 10000$.

A typical form of the solutions for the inviscid fluid (scheme ZE) after spatial averaging is shown in Figure 1.1, in comparison with the viscous fluid. The figure is

taken from [1; 2], not included in the dissertation, and differs in that the number of square patches with constant vorticity in the initial data is different.

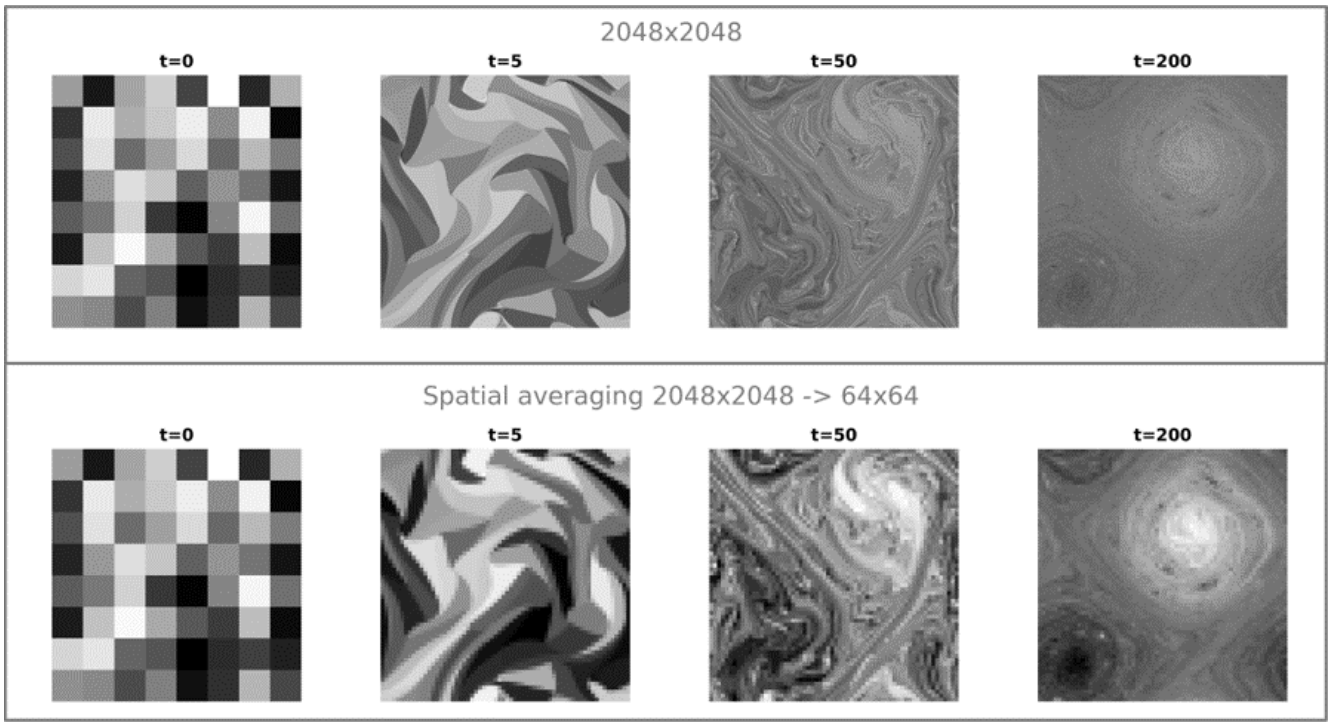

Figure 1.1 — Evolution of vorticity in the experiment without viscosity (top row) and in the experiment with viscosity (bottom row). In the inviscid experiment spatial averaging is performed. The experiments are shown for illustration and are described in detail in [1; 2], not included in the dissertation.

We first present the results for the scheme with two invariants (ZE), and then compare this scheme with the other two (Z, E).

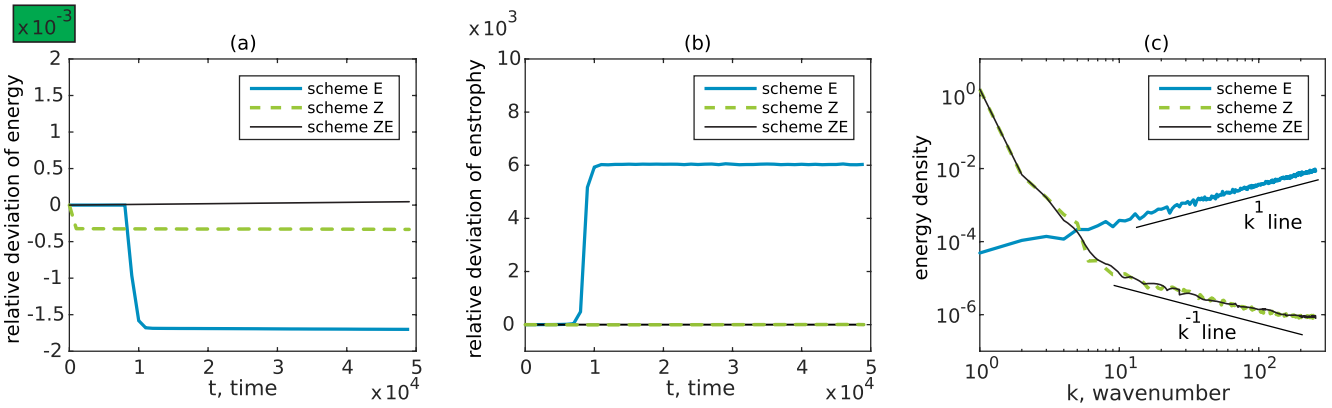

Figure 1.2 — Relative deviation of energy and enstrophy from initial values (a), (b); and the spectral distribution of energy (c) at the last moment of time $t = 50000$ for three schemes (E, Z, ZE). Note that the scale of panels (a) and (b) differs by six orders of magnitude.

In the computation with the ZE scheme the energy and the enstrophy are conserved with a relative accuracy of 10^{-4} over the whole time of the computation, see Figures 1.2a and 1.2b. Figure 1.3 shows the area distribution of vorticity $\rho(\omega)$ at the final moment of time. It follows from the figure that the distribution has a Gaussian form. The variance of the distribution is determined by the initial data and equals $2\overline{\omega^2}/D$. We make use of the kurtosis coefficient $\gamma = \frac{\int \omega^4 \rho d\omega}{(\int \omega^2 \rho d\omega)^2}$ to determine the closeness of the area distribution $\rho(\omega)$ to a Gaussian one (for the standard normal distribution $\gamma = 3$). Figure 1.4 shows the kurtosis coefficient as a function of time at three different resolutions (the standard resolution 512×512 and two more: 128×128 and 2048×2048). On the time interval $t \in (0,50)$ a sharp growth of this coefficient is observed, related to the establishment of statistical equilibrium at small scales. Further, on the long interval $t \in (50,10000)$ the large scales also come to full statistical equilibrium, and the kurtosis coefficient becomes practically equal to 3 for all resolutions (not shown). As a characteristic time for the establishment of small scales we take the time during which the kurtosis coefficient first reaches the value 3. The characteristic time grows slowly with increasing resolution ($T \sim N^{0.3}$, where N is the number of nodes along one direction), see Figure 1.4. This is an illustration of the convergence theorem: the higher the resolution of the computational grid, the longer the initial distribution $\rho(\omega)$ is preserved.

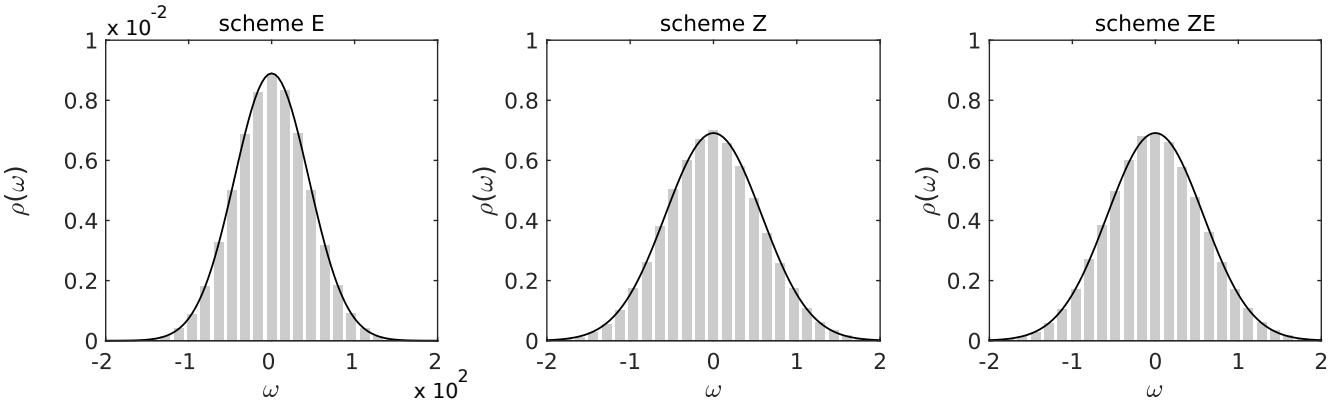

Figure 1.3 — Histogram of the area distribution of vorticity at the final moment of time $t = 50000$ for three schemes (E, Z, ZE). The number of histogram bins is 25. The black curve is the Gaussian distribution with equivalent variance.

Let us describe the properties of the statistical equilibrium state for the Arakawa ZE scheme. The theory implies that at small scales enstrophy must be equally distributed among the Fourier modes [1], and this is confirmed by the numerical experiment: the energy spectrum has a decreasing power-law dependence $E(k) \sim k^{-1}$ at small scales, see Figure 1.2c. From the same figure it follows that most of the energy accumulates at large scales, as a result of which large-scale coherent structures are

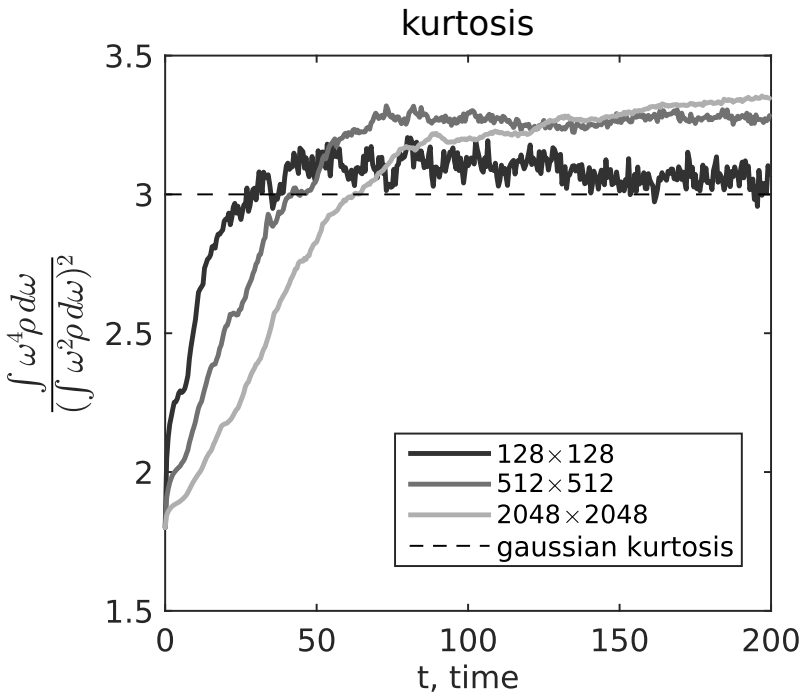

Figure 1.4 — Kurtosis coefficient of the distribution $\rho(\omega)$ for the computation with the ZE scheme at three different resolutions.

formed having a characteristic size comparable to the size of the domain, see Figure 1.5. Two large vortices form by time $t \approx 200$, after which slow processes of equilibration follow. The large vortices are close to stationary solutions of the equations of the ideal fluid: the scatter diagram $\langle\psi\rangle - \langle\omega\rangle$ is described by a certain functional dependence, see Figure 1.6. This functional dependence is close to the linear one (1.12), and at large values of the streamfunction deviations from the linear dependence are observed, thus qualitatively confirming formula (1.11).

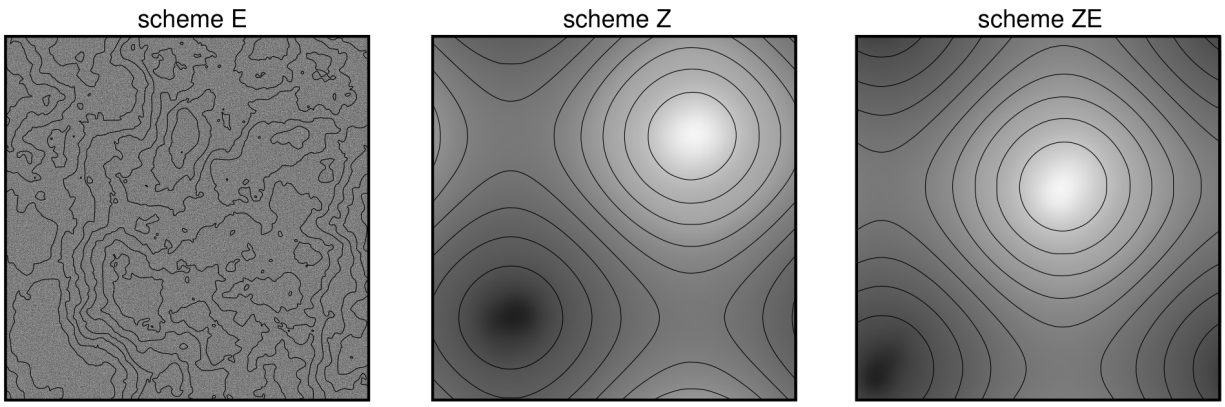

Figure 1.5 — Vorticity (shown in colour) and streamfunction (shown by lines), preliminarily averaged over the time interval $t \in (20000,50000)$.

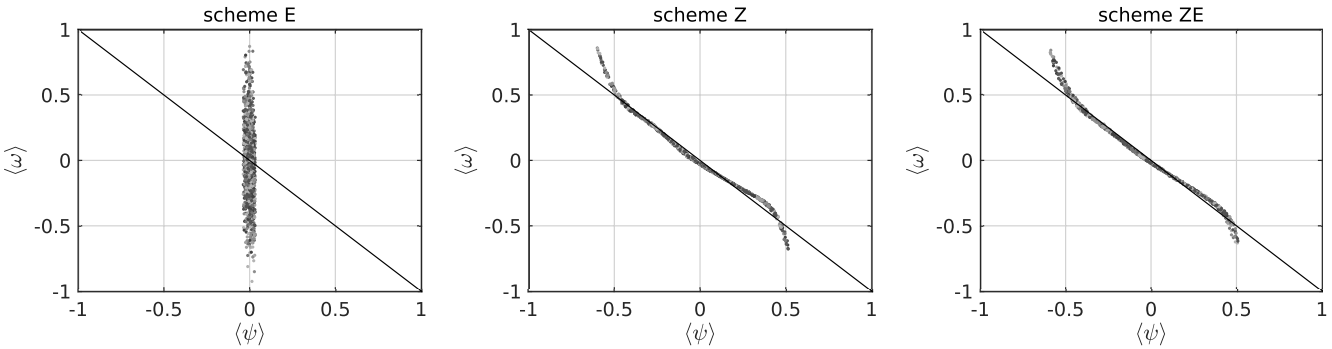

Figure 1.6 — Scatter diagram $\langle\psi\rangle - \langle\omega\rangle$, where angular brackets denote averaging over the time interval $t \in (0{,}50000)$. The black line corresponds to the relation $\langle\omega\rangle = -\langle\psi\rangle$: the theoretical prediction (1.12) with $|\lambda_{\min}| = 1$.

The scheme with a single quadratic invariant—enstrophy (Z)—gives results similar to the ZE scheme, see Figures 1.2, 1.3, 1.5, 1.6. In this case approximate conservation of energy is observed throughout the computation, see Figure 1.2a. An analogous result is given in [105]. We note that other systems of hydrodynamic type with the enstrophy invariant can dissipate energy, in which case no coherent structures are observed [94].

As shown above, for the scheme with a single quadratic invariant—energy (E)—an unbounded generation of enstrophy is possible, and this is what happens in the numerical experiment: during the equilibration the level of enstrophy increases by a factor of 6000, see Figure 1.2b. The excess enstrophy accumulates at small scales, and this leads to the energy cascading into the region of high wavenumbers, where energy equipartition over the Fourier modes is observed (after angular integration in Fourier space, $E(k) \sim k$), see Figure 1.2c. As a consequence, coherent structures at large scales are not formed, see Figures 1.5, 1.6. As a result of the enstrophy generation, the variance of the area distribution $\rho(\omega)$ significantly increases compared with schemes ZE and Z, see Figure 1.3; however, the functional form of the distribution does not change: it remains Gaussian.

1.3 Large-scale structure and area distribution of vorticity in the two-dimensional equations with dissipation and forcing

Consider the two-dimensional equations of a viscous fluid in a doubly periodic channel:

$$\frac{\partial \omega}{\partial t} + J(\psi,\omega) = f - \alpha\omega + \mu \triangle \omega, \tag{1.23}$$
$$\omega|_{t=0} = \omega^0,$$

where $\omega = \triangle\psi$, f is the external forcing, α is the coefficient of Rayleigh friction, μ is the viscosity coefficient. The asymptotic properties of this equation are considered in numerous works (see [97] and the references therein). Let

$$\frac{\partial \omega_h}{\partial t} + J^h(\psi_h,\omega_h) = f_h - \alpha\omega_h + \mu \triangle_h \omega_h, \tag{1.24}$$
$$\omega_h|_{t=0} = \omega_h^0$$

be some finite-difference approximation of (1.23), in which the system (1.24) at $f = 0$, $\alpha = 0$, $\mu = 0$ is a system of hydrodynamic type. The central question we consider in this section is the following: in what sense are the asymptotic (statistical) properties of (1.24) determined by the asymptotic (statistical) properties of the corresponding system of hydrodynamic type?

The equations for energy and enstrophy in the system (1.23) have the form

$$\frac{\partial E}{\partial t} = -(f,\psi) - 2\alpha E - 2\mu\overline{\omega^2} \tag{1.25}$$
$$\frac{\partial \overline{\omega^2}}{\partial t} = (f,\omega) - 2\alpha\overline{\omega^2} + \mu(\triangle\omega,\omega). \tag{1.26}$$

Averaging (1.25) and (1.26) over time we obtain the mean values of energy $\langle E\rangle$ and enstrophy $\langle\overline{\omega^2}\rangle$:

$$\langle E\rangle = \frac{-\langle(f,\psi)\rangle - 2\mu\langle\overline{\omega^2}\rangle}{2\alpha} \tag{1.27}$$
$$\langle\overline{\omega^2}\rangle = \frac{\langle(f,\omega)\rangle + \mu\langle(\triangle\omega,\omega)\rangle}{2\alpha}. \tag{1.28}$$

The relations (1.27), (1.28) express the principal difference between the systems (1.3) and (1.23): in the first case $\langle E\rangle$ and $\langle\overline{\omega^2}\rangle$ are determined by the initial data, whereas

in the second they (asymptotically) do not depend on the initial data. When solving the equations (1.23) it turns out to be useful to employ schemes that do not allow the growth of enstrophy. According to the relation (1.27), an increase of the enstrophy level leads to a decrease of the energy level and, as a consequence, to a growth of the mean squared wavenumber. This effect will be demonstrated in the next chapter of the dissertation 2, where the distribution of energy along the spectrum is studied in detail for various schemes of solving the equations (1.23).

As in the case of the ideal fluid, we shall be interested in such characteristics of the system (1.23) as large-scale coherent structures and the area distribution of vorticity. Let the forcing be set on such spatial scales that the formation of two inertial intervals associated with the energy and enstrophy cascades is possible [18]. In these intervals, by definition, dissipation must not significantly affect the formation of the energy distribution over scales, i.e. the fluid must behave as an ideal one. This can be achieved if the scale of dissipation due to viscosity is chosen much smaller than the forcing scale, and the time scale of Rayleigh friction is much greater than the time scale of energy transfer along the spectrum. Both conditions are satisfied at sufficiently small coefficients μ and α. In [1] it was shown that at sufficiently small μ the quasi-equilibrium states of the viscous fluid are close to the corresponding states of the ideal fluid, see Figure 1.1.

Two numerical experiments were carried out for the problem (1.23), solved with the Arakawa ZE scheme, with the following parameters (all parameters are non-dimensional): resolution 1024×1024, $\mu = 4.69 \cdot 10^{-6}$, computation time $t = 15000$. The random δ-correlated forcing is set at wavenumber 45 and provides an energy influx per unit surface per unit time $\varepsilon = 1.534 \cdot 10^{-4}$. The algorithm for constructing the external forcing is given in Appendix A. The difference between the two experiments lies in the different scale of blocking of the inverse energy cascade, set by the Rayleigh friction coefficient: $\alpha = 0.012$ and $\alpha = 0.0003$.

Figure 1.7 shows the energy distribution along the spectrum in the two experiments. From the figure it is seen that in the case of a large Rayleigh friction $\alpha = 0.012$ the energy cascade in the region of low wavenumbers is blocked at approximately the wavenumber $k = 5$, and no quasi-stationary coherent structure is observed. At the small coefficient $\alpha = 0.0003$ coherent structures close to those observed in the ideal fluid have already formed; compare Figures 1.7 and 1.5. The scatter diagram $\overline{\psi} - \overline{\omega}$ is shown in Figure 1.8. As in the ideal fluid, at small Rayleigh friction a functional dependence $\overline{\omega} = F(\overline{\psi})$ is observed, which is close to the linear one (1.12) at small $\overline{\psi}$. In both cases the area distribution of vorticity is close to the Gaussian one, see Figure 1.8.

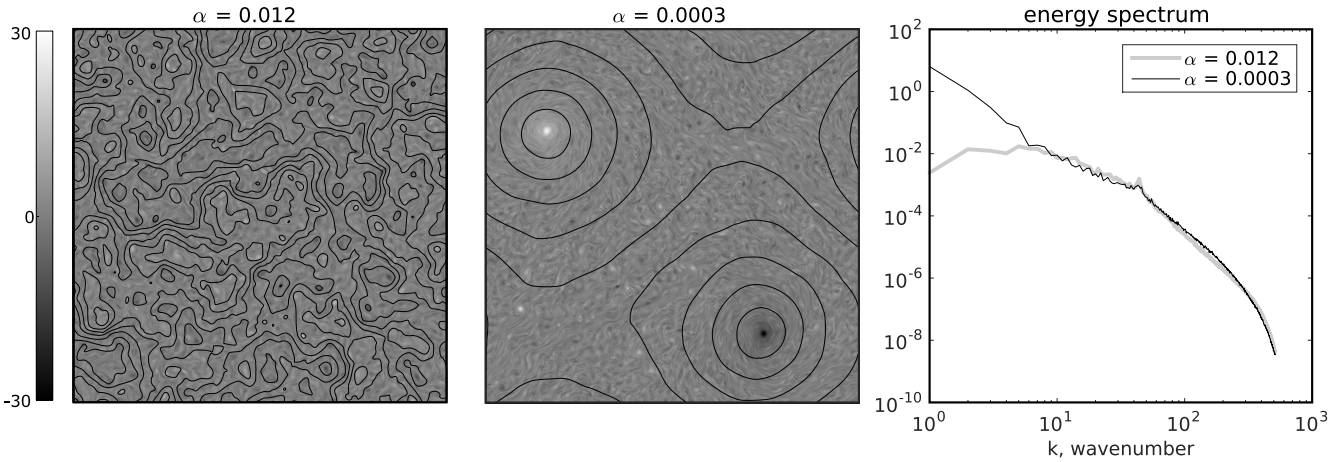

Figure 1.7 — Vorticity (shown in colour) and streamfunction (shown by lines) – left; energy spectrum – right. The figures correspond to the final moment of time $t = 15000$.

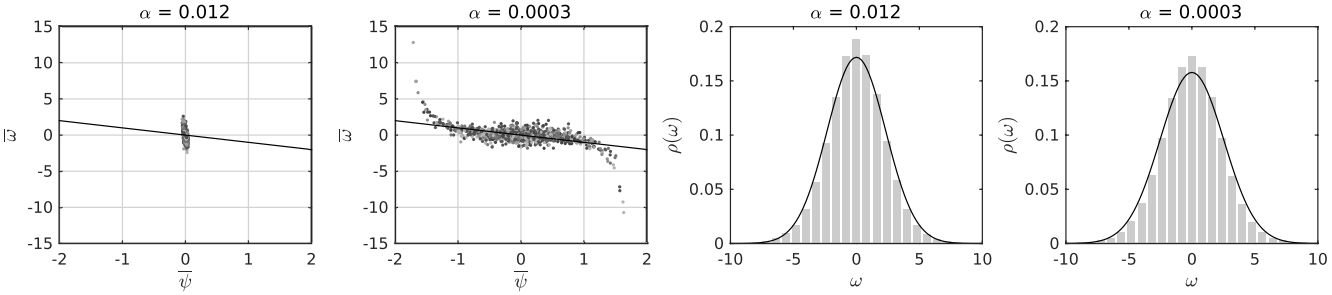

Figure 1.8 — Left – scatter diagram $\overline{\psi} - \overline{\omega}$, where the overbar denotes averaging over cells of 32×32 grid points. The black line corresponds to the linear relation (1.12). Right – area distribution of vorticity, 25 histogram bins, the black curve corresponds to the Gaussian distribution with equivalent variance. The figures correspond to the final moment of time $t = 15000$.

It is worth noting that area distributions of vorticity close to a Gaussian one have been observed also in computations from real data in the atmosphere (500 hPa surface) [99].

1.4 Conclusions

In this chapter we have investigated the statistical properties of three difference schemes approximating the equations of an ideal two-dimensional incompressible fluid and belonging to the class of systems of hydrodynamic type introduced by A.M. Obukhov. It was shown that even in the presence of a convergence theorem on a finite time interval for one of the difference schemes (the Arakawa scheme, which has two quadratic invariants—energy and enstrophy), when an arbitrarily large time interval is considered, the schemes in principle cannot reproduce certain properties of the ideal two-dimensional fluid, in particular the conservation of the area distribution of vorticity, the reproduction of which requires an infinite number of invariants (Casimirs). At the same time, the time interval on which the initial area distribution of vorticity is approximately conserved grows slowly with increasing resolution, which is nonetheless consistent with the convergence theorem.

The scheme conserving only energy does not reproduce other essential properties of the ideal fluid either: the formation of a stationary quasi-equilibrium state satisfying a linear relation between vorticity and streamfunction when a certain averaging procedure is performed (e.g., consideration of Cesàro convergence), and the energy distribution along the spectrum. As for the scheme conserving only one quadratic invariant—enstrophy—the results of modelling with it the quasi-equilibrium states of the ideal fluid differ little from the results obtained with the Arakawa scheme, which is explained by the presence of the embedding theorem prohibiting an energy cascade to high wavenumbers.

The question arises: is it necessary to take into account the reproduction of the fundamental properties of the ideal two-dimensional fluid when modelling a viscous quasi-two-dimensional fluid with external forcing? In the case of a viscous fluid there are a global solvability theorem and convergence theorems of the solutions of difference schemes to the solution of the differential problem in which, when the viscosity coefficient and the forcing tend to zero, only one quadratic invariant—the energy—exists (a “bad” scheme from the point of view of reproducing the statistical properties of the ideal fluid). However, it should be noted that the constants in all these theorems (if they are determined), as a rule, depend exponentially on the time interval, and thus the theorems are practically of no help to us in investigating the above-mentioned problem. In this chapter we have shown that at small Rayleigh friction coefficients, i.e. in

the case where there is no dissipation and generation of energy in the large region of wavenumbers associated with the inertial interval of the inverse energy cascade, the following properties of systems of hydrodynamic type manifest themselves in viscous forced turbulence: quasi-stationary coherent structures are formed, and also a Gaussian area distribution of vorticity is observed. In this chapter differences between the schemes were not found in the problem of modelling forced turbulence. As shown in the next chapter, the differences begin to manifest themselves at coarser spatial resolutions of the computational grid.

Chapter 2. Investigation of the influence of numerical advection schemes on the reproduction of the inverse energy cascade

In the previous chapter it was shown that the statistically equilibrium states arising in systems approximating the equations of the ideal fluid can strongly depend on the choice of approximation of the advective term. Moreover, certain properties of the ideal fluid—such as the formation of quasi-stationary large-scale coherent structures and the Gaussian area distribution of vorticity—can also be observed in a more realistic problem, namely forced turbulence. In this chapter it is proposed to clarify how the choice of the numerical advection scheme affects the reproduction of the inverse energy cascade for various ratios between the scale of the external forcing and the step of the computational grid. In the ideal fluid, the scheme with a single invariant (energy) generates enstrophy almost without bound. This effect impedes the propagation of energy to large scales and, as a consequence, the formation of a large-scale coherent structure. In forced turbulence the generation of enstrophy is suppressed by viscosity, which limits the scheme errors in the short-wave range; nevertheless, as shown in this chapter, the inverse energy cascade can be weakened when the scale of the external forcing is chosen close to the grid step (such situations arise in eddy-permitting ocean models that poorly resolve the internal Rossby deformation radius on the grid).

2.1 Equations and model parameters

We consider the dynamics of a two-dimensional incompressible fluid on the square $(x_1,x_2) \in [0,2\pi) \times [0,2\pi)$ with periodic boundary conditions in Cartesian coordinates. Numerical schemes are considered both in velocity–pressure variables and in vorticity–streamfunction variables.

In the natural velocity–pressure variables $(\mathbf{u},p)$ the equations of motion are written in the following form:

$$\begin{cases} \dfrac{\partial \mathbf{u}}{\partial t} + (\mathbf{u} \cdot \nabla)\mathbf{u} = -\nabla p - \nu\Delta^2\mathbf{u} - \alpha\mathbf{u} + \mathbf{f} & \text{(2.1а)} \\ \nabla \cdot \mathbf{u} = 0. & \text{(2.1б)} \end{cases}$$

Here $\mathbf{u} = (u_1, u_2)$ is the velocity, p is the pressure, $\mathbf{f}$ is the forcing (the external force acting on the flow) described in Appendix A, $\alpha > 0$ is the Rayleigh friction coefficient. As the basic model for describing subgrid turbulence, the biharmonic operator with coefficient $\nu > 0$ is chosen. This choice corresponds to the general practice of suppressing numerical noise in models of atmospheric and ocean dynamics, where dissipative terms acting predominantly on the short-wave part of the spectrum are often used.

In the streamfunction–vorticity variables (ψ, ω) we have the following form of the equations:

$$\begin{cases} \dfrac{\partial \omega}{\partial t} + (\mathbf{u} \cdot \nabla)\omega = -\nu\Delta^2\omega - \alpha\omega + f & \text{(2.2а)} \\ \Delta\psi = \omega, & \text{(2.2б)} \end{cases}$$

where ω is the vorticity, ψ is the streamfunction, f is the forcing (the external action on the vorticity). The variables in equations (2.1) and (2.2) are related by

$$\mathbf{u} = \left(-\frac{\partial \psi}{\partial x_2}, \frac{\partial \psi}{\partial x_1} \right) \tag{2.3}$$

$$\omega = \frac{\partial u_2}{\partial x_1} - \frac{\partial u_1}{\partial x_2}. \tag{2.4}$$

For the approximation of equations (2.1), (2.2), a uniform spatial grid with steps (h_{x_1}, h_{x_2}) and time step Δt is chosen, and the following difference operators are introduced:

$$\delta_{x_i}\varphi = \frac{\varphi(x_i + h_{x_i}/2) - \varphi(x_i - h_{x_i}/2)}{h_{x_i}} \tag{2.5}$$

$$\overline{\varphi}^{x_i} = \frac{\varphi(x_i + h_{x_i}/2) + \varphi(x_i - h_{x_i}/2)}{2} \tag{2.6}$$

$$\nabla_h \cdot \mathbf{u} = \delta_{x_i} u_i \tag{2.7}$$

$$\Delta_h\varphi = \nabla_h^2\varphi = \delta_{x_i}(\delta_{x_i}\varphi), \tag{2.8}$$

here and below summation over the repeated index is assumed.

2.2 Numerical methods

2.2.1 Finite-difference schemes in the variables $(\mathbf{u}, p)$

The system of equations (2.1) is solved by the projection method [106]. The intermediate value of the velocity $\mathbf{u}'$ is found by the following scheme:

$$\frac{\mathbf{u}' - \mathbf{u}^n}{\Delta t} = -[(\mathbf{u}\cdot\nabla)\mathbf{u}]_h^{n+1/2} - \nabla_h p^n - \nu\Delta_h^2\mathbf{u}^{n+1/2} - \alpha\mathbf{u}^{n+1/2} + \mathbf{f}^n.$$

The spatial discretization of the advective term $(\mathbf{u}\cdot\nabla)\mathbf{u}$ is denoted by the subscript h and varies from one scheme to another. Values on the $n+1/2$ time layer $[(\mathbf{u}\cdot\nabla)\mathbf{u}]_h^{n+1/2}$, $\nu\Delta_h^2\mathbf{u}^{n+1/2}$, $\alpha\mathbf{u}^{n+1/2}$ are computed using the second-order Adams–Bashforth scheme

$$\varphi^{n+1/2} = \frac{3}{2}\varphi^n - \frac{1}{2}\varphi^{n-1}.$$

Next, the pressure correction φ^{n+1} is sought from the condition

$$\Delta_h\varphi^{n+1} = \frac{\nabla_h\cdot\mathbf{u}'}{\Delta t}$$

and the projection step is carried out:

$$\mathbf{u}^{n+1} = \mathbf{u}' - \Delta t\nabla_h\varphi^{n+1}$$
$$p^{n+1} = p^n + \varphi^{n+1}.$$

Scheme used in the ocean model **INMOM**

In the INMOM model [107] the advection $(\mathbf{u}\cdot\nabla)\mathbf{u}$ is approximated by second-order central differences on the staggered C-grid (in Arakawa's terminology). The scheme conserves energy and, provided the discrete analogue of the continuity equation $\nabla_h\cdot\mathbf{u} = 0$ is satisfied, can be written in the simple form [108]:

$$[(\mathbf{u}\cdot\nabla)u_i]_h = \delta_{x_j}(\overline{u_j}^{x_i}\overline{u_i}^{x_j}).$$

Scheme used in the atmospheric model **INMCM**

In the atmospheric model, which is part of the INMCM climate model [109], one of the Arakawa schemes [110] is used. On the sphere it conserves angular momentum. It can

be obtained by considering, in addition to the usual coordinate system (x_1,x_2), an additional one (x'_1,x'_2) which on a square grid is obtained by a 45-degree counterclockwise rotation. The scheme has the form of a linear combination of the terms $(\mathbf{u}\cdot\nabla)\mathbf{u}$ written in the two coordinate systems:

$$[(\mathbf{u}\cdot\nabla)u_i]_h = \frac{2}{3}\cdot\overline{\overline{u_j}^{x_i}\delta_{x_j}u_i}^{x_j} + \frac{1}{3}\cdot\overline{u'_j\delta_{x'_j}u_i}^{x'_j}, \tag{2.9}$$

where (u'_1,u'_2) is the velocity in the new coordinate system (x'_1,x'_2).

2.2.2 Finite-difference schemes in the variables (ψ,ω)

The system of equations (2.2) is solved in two stages. At the first stage we solve the evolution equation (2.2a) and obtain the vorticity at the new step ω^{n+1} using the second-order Adams–Bashforth scheme. At the second stage we recover the streamfunction ψ^{n+1} from the vorticity ω^{n+1} according to the Poisson equation (2.2б), using the discrete Laplace operator (2.8).

Arakawa schemes The approximations E, Z, ZE described in Section 1.1 are used.

2.2.3 Semi-Lagrangian methods in the variables (ψ,ω)

The system of equations (2.2) is solved in two stages similarly to what is described in the previous Section 2.2.2; however, recovery of the streamfunction ψ^{n+1} is followed by determination of the velocity $\mathbf{u}^{n+1}$. To update the vorticity at the new time layer ω^{n+1} a semi-Lagrangian method is used, having the form

$$\frac{\omega_{\mathrm{A}}^{n+1}-\omega_{\mathrm{D}}^{n}}{\Delta t} = F(\omega^n)_{\mathrm{A}},$$

here A are the arrival points of the trajectory located at the grid nodes, and D are the departure points. The advection is described by the left-hand side of the equation, and the right-hand side $F(\omega)$ is responsible for dissipation and the external forcing, which do not require high accuracy and therefore are approximated with first-order accuracy

in time. The value ω_{D}^n is found by interpolation, and the schemes differ from each other only by the form of the interpolant. The trajectories are computed using the SETTLS scheme [111], used in the SL-AV model [112]. For the characteristic equation

$$\frac{d\mathbf{x}}{dt} = \mathbf{u}$$

it has the form

$$\frac{\mathbf{x}_{\mathrm{A}}^{n+1} - \mathbf{x}_{\mathrm{D}}^{n}}{\Delta t} = \frac{1}{2}([2\mathbf{u}^n - \mathbf{u}^{n-1}]_{\mathrm{D}} + \mathbf{u}_{\mathrm{A}}^n). \tag{2.10}$$

The scheme is implicit with respect to the point D and is solved iteratively in 5 iterations using cubic interpolation of the velocity at the point D.

Types of interpolation

We shall distinguish semi-Lagrangian methods only by the type of one-dimensional interpolation. There are many ways to split a two-dimensional interpolation problem into a sequence of one-dimensional ones [113; 114]. Among the many methods we have chosen the cascade approach [114], since it is used in the new version of the SL-AV model [115]. In addition to the cascade approach, the tensor product method [113] was also tested, and in our experiments no differences were found.

The following types of one-dimensional interpolation have been investigated:

cubic – cubic interpolation [116]

hermite – Hermite interpolation. It satisfies the necessary and sufficient conditions of monotonicity [113] (by monotonicity we mean monotonicity of the interpolant on a grid step). The conditions of monotonicity NCM1 and SCM from [113] are taken. To construct the interpolant on an interval, one must know the values of the function and its derivative at the ends of the interval. The function values are known, and the values of the derivative are found with the help of a cubic interpolant (see [113], "cubic derivative estimate"). Then the values of the derivative are checked for monotonicity. If the monotonicity conditions are satisfied, the interpolation remains cubic; otherwise a correction is applied.

CCS – the cascade conservative semi-Lagrangian scheme [117]. In this scheme a sequence of one-dimensional redistributions of the mass contained in the computational cell is carried out. The mass redistribution for a one-dimensional conservation law of the form

$$\frac{\partial \rho}{\partial t} + \frac{\partial \rho u}{\partial x} = 0$$

is expressed as

$$\int_{A(t^{n+1})} \rho dx = \int_{A(t^n)} \rho dx, \tag{2.11}$$

here $A(t)$ is a volume moving with the fluid which at the moment of time $n+1$ coincides with the computational cell. The integral on the right-hand side of (2.11) is found approximately using a conservative piecewise-parabolic interpolation.

In the SL-AV model all the described interpolants are implemented; however, in the operational version of the model only two are used: cubic in the dynamical core and CCS for tracer advection [115].

2.2.4 Semi-Lagrangian methods in the variables $(\mathbf{u}, p)$

The system of equations (2.1) is solved by the projection method similarly to what is described in Section 2.2.1, using the semi-Lagrangian methods described in Section 2.2.3; however, the treatment of pressure is different and has the form of the Crank–Nicolson scheme [118]

$$\frac{\mathbf{u}_{\mathrm{A}}^{n+1} - \mathbf{u}_{\mathrm{D}}^{n}}{\Delta t} = -\frac{1}{2}(\nabla_h p_{\mathrm{A}}^{n+1} + \nabla_h p_{\mathrm{D}}^{n}) + F(\mathbf{u}^n)_{\mathrm{A}}.$$

2.3 Numerical experiments

The equations (2.1), (2.2) are solved until statistical equilibrium is reached ($t = 100$, approximately 4000 time steps for the semi-Lagrangian schemes). Then the computation is continued for another 500 time units to obtain averaged characteristics of the solution. In all the experiments the forcing provides an energy influx per unit surface per unit time $\varepsilon = 1.534 \cdot 10^{-4}$. The Rayleigh friction coefficient equals $\alpha = 0.012$. Our analysis excludes consideration of time-integration errors of advection, so we use small time steps for the finite-difference schemes: Courant number $\frac{u_{max}\Delta t}{h} < 0.15$. For the semi-Lagrangian schemes the Courant number is set equal to 1, since as a rule semi-Lagrangian methods are not used at low Courant numbers.

The results of computations at low spatial resolution (coarse models) are compared with the high-resolution DNS model, which is computed using the ZE scheme on the fine grid 2016×2016 (the viscosity coefficient was chosen so as to obtain the most extended enstrophy interval). The viscosity coefficient in the coarse models depends on the forcing scale and the resolution, and is given in each case separately. The level of energy in the ideal model (energy is not dissipated when biharmonic viscosity is used) can be obtained by equating the energy influx from the forcing ε and the dissipation by Rayleigh friction $2\alpha E$:

$$E = \frac{\varepsilon}{2\alpha}. \tag{2.12}$$

2.3.1 Large-scale forcing

The problem is solved at resolution 360×360 nodes. The external forcing is set on large scales, at the wavenumber $k_f = 4$. The biharmonic viscosity coefficient is $\nu = 1.06 \cdot 10^{-9}$.

Figure 2.1 shows the spectral distribution of energy for the schemes under study (semi-Lagrangian methods only in the variables (ψ,ω)). The large-scale part of the spectrum is the same for all numerical discretizations of advection and coincides with the DNS high-resolution computation. The energy level differs from one scheme to another by no more than 1% and is consistent with the theoretical estimate (2.12). The external forcing is well separated in scale from the grid scale, and the energy is practically

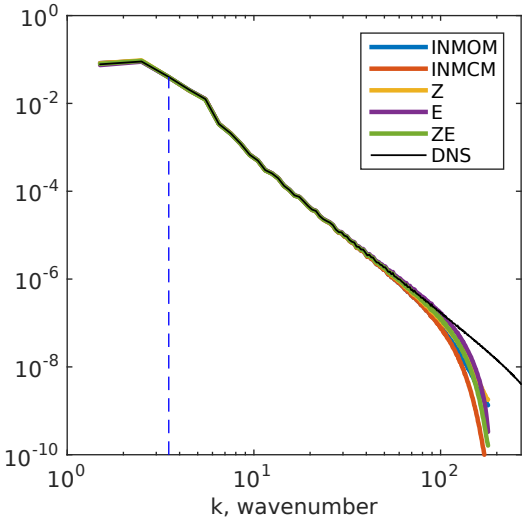

a) finite-difference schemes

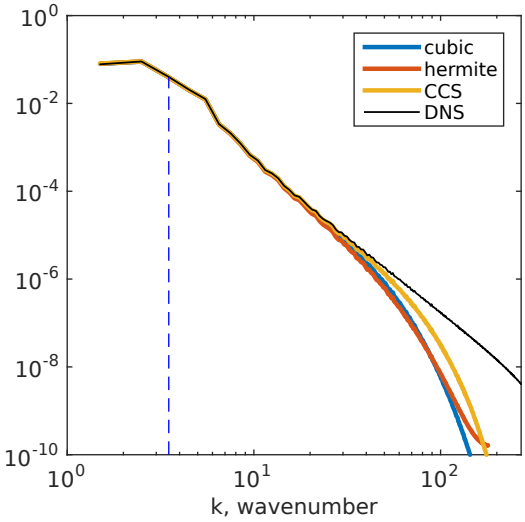

b) semi-Lagrangian schemes, (ψ, ω)

Figure 2.1 — Energy spectrum in the experiment with large-scale forcing; the forcing scale is shown by the dashed line; resolution 360^2.

not dissipated by viscosity. Scheme errors of energy non-conservation are also insignificant. Differences are observed on small scales (region of high wavenumbers), where scheme effects manifest themselves most strongly. The semi-Lagrangian schemes are inferior to the finite-difference ones in the magnitude of dissipation. For this reason, the energy spectrum of the semi-Lagrangian schemes is underestimated down to intermediate scales (12 grid steps), whereas for the finite-difference schemes it is underestimated down to 6 grid steps. One can conclude that if the forcing has a sufficiently large scale, then the nonlinear character of the approximation errors is not capable of altering the large-scale dynamics.

2.3.2 Small-scale forcing

The external perturbation is located at small scales, $k_f = 90$. The problem is solved at resolutions 540×540 (the forcing corresponds to waves of length 6 grid steps, $\nu = 4.21 \cdot 10^{-10}$) and 360×360 (the forcing corresponds to waves of length 4 grid steps, $\nu = 2.13 \cdot 10^{-9}$).

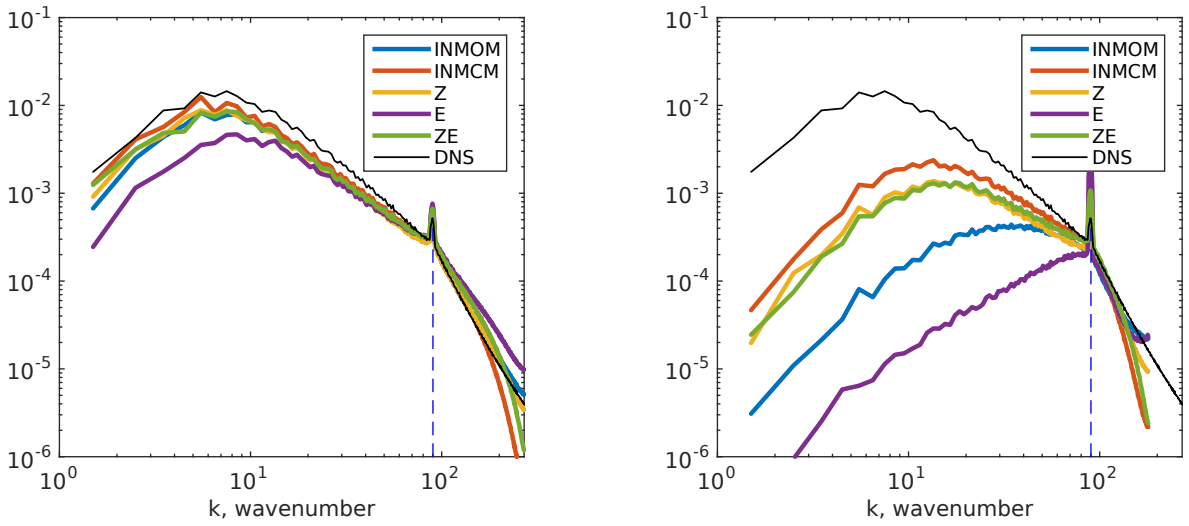

a) resolution 540^2 b) resolution 360^2

Figure 2.2 — Energy spectrum for the finite-difference schemes in the experiment with small-scale forcing; the forcing scale is shown by the dashed line.

Finite-difference schemes

The spectral distribution of energy for the finite-difference schemes is shown in Figure 2.2, which illustrates the process of disruption of the inverse energy cascade as the resolution is coarsened. As seen in Figure 2.2(b), practically all finite-difference schemes, regardless of whether they use the variables $(\mathbf{u},p)$ or (ψ,ω), have a similar form of the spectrum at large scales, with the exception of the two schemes E and INMOM, which conserve only energy. These schemes have a noticeably lower energy level at resolution 360×360, since they generate enstrophy at small scales (see Table 1), where it is dissipated by the numerical filter, which in turn leads to a decrease in the energy level. This effect was already discussed when considering the relation (1.27) in the previous chapter of the dissertation.

The INMCM scheme has the highest energy level, even higher than the scheme with the two quadratic invariants ZE, see Table 1. This happens for two reasons. First, it is practically energy-conserving. Second, the scheme dissipates enstrophy. The combination of these two properties means that the scheme reduces the mean squared wavenumber, i.e. it "models" the kinetic energy backscatter (KEB). A detailed analysis of KEB is given in the next chapter of the dissertation 3.

Table 1 — Energy (E) and enstrophy (Z) levels, and also their fluxes $\partial E/\partial t$, $\partial Z/\partial t$. E,Z are normalized by the DNS values. The fluxes are normalized by ε and $k_f^2\varepsilon$. Finite-difference schemes, 540×540, small-scale forcing.

scheme	E	$\partial E/\partial t$			Z	$\partial Z/\partial t$		
		scheme	**viscosity**	**friction**		**scheme**	**viscosity**	**friction**
INMOM	64%	0%	-38%	-62%	71%	23%	-110%	-13%
INMCM	75%	-0.33%	-27%	-72%	67%	-32%	-55%	-12%
Z	64%	-5%	-34%	-62%	66%	0%	-84%	-12%
E	49%	0%	-53%	-47%	86%	61%	-145%	-16%
ZE	66%	0%	-37%	-63%	75%	0%	-87%	-14%
DNS	100%	0%	-4%	-96%	100%	0%	-83%	-17%

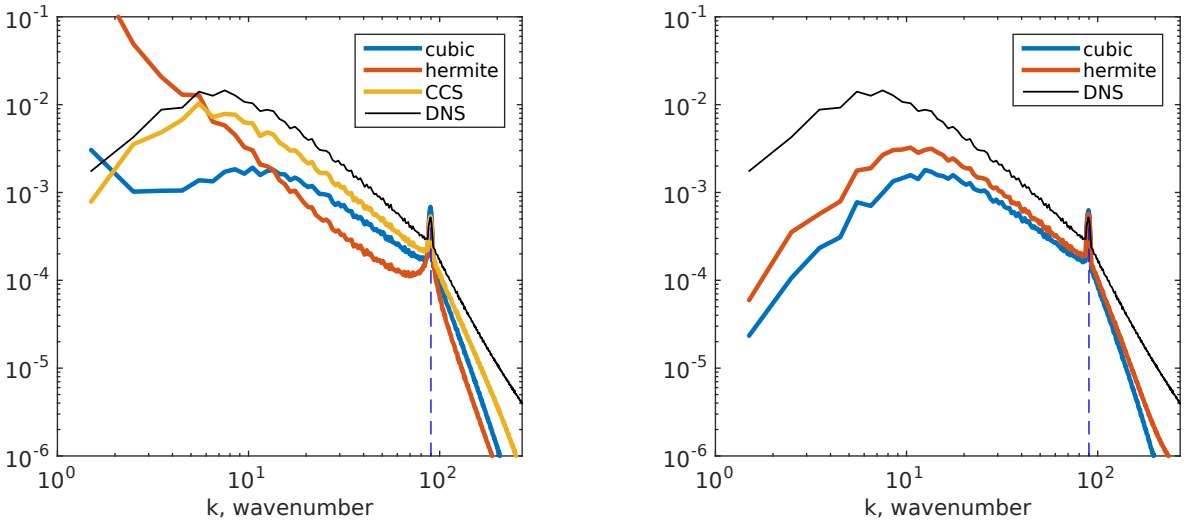

a) variables (ψ,ω) b) variables $(\mathbf{u},p)$

Figure 2.3 — Energy spectrum for the semi-Lagrangian schemes in the experiment with small-scale forcing; the forcing scale is shown by the dashed line; resolution 540^2.

Semi-Lagrangian methods

Figure 2.3 shows the energy spectra for the semi-Lagrangian methods. In the variables $(\mathbf{u}, p)$ these methods give results similar to those of the finite-difference schemes. The difference consists in the additional dissipation, which is minimal for the hermite scheme, see Figure 2.3(b).

The majority of semi-Lagrangian methods do not conserve the first moment. In the case of the variables $(\mathbf{u},p)$ this means violation of the conservation law for the integral momentum, while in the case of the variables (ψ, ω) it means violation of the

conservation law for the integral vorticity. Among all the schemes presented in this work, only the cubic and hermite schemes do not conserve the integral of the transported quantity. Among the semi-Lagrangian methods in the variables (ψ, ω), only the conservative CCS scheme gives the correct asymptotics of the spectrum at large scales, see Figure 2.3(a). The cubic and hermite schemes have a singularity at the wavenumber $k = 0$: energy accumulates at large scales. The transfer of energy to large scales turns out to be nonlocal in Fourier space and occurs immediately after the start of the numerical experiment, unlike the conservative schemes. The generation of energy at large scales can lead to serious violations of the energy balance in the system (see Table 2, hermite), which remain when the resolution is doubled (figure not shown). We attribute the generation of energy at large scales to the magnitude of non-conservation of the integral vorticity: in [119] it is shown that the hermite scheme has significant non-conservation of the integral of the transported quantity. To test our hypothesis, experiments were carried out with upwind 2nd- and 3rd-order schemes, which showed that the non-conservation of the integral vorticity leads to singularities at large scales (figure not shown).

Table 2 — Energy (E) and enstrophy (Z) levels, and also their fluxes $\partial E/\partial t$, $\partial Z/\partial t$. E,Z are normalized by the DNS values. The fluxes are normalized by ε and $k_f^2\varepsilon$. Semi-Lagrangian methods, 540×540, small-scale forcing.

scheme	E	$\partial E/\partial t$			Z	$\partial Z/\partial t$		
		scheme	**viscosity**	**friction**		**scheme**	**viscosity**	**friction**
vorticity–streamfunction variables								
cubic	26%	-64%	-11%	-25%	32%	-77%	-17%	-6%
hermite	211%	110%	-7%	-203%	21%	-85%	-11%	-4%
CCS	59%	-27%	-17%	-57%	46%	-59%	-33%	-8%
velocity–pressure variables								
cubic	23%	-68%	-10%	-22%	32%	-80%	-14%	-5%
hermite	35%	-53%	-13%	-34%	39%	-69%	-23%	-7%
DNS	100%	0%	-4%	-96%	100%	0%	-83%	-17%

2.4 Conclusions

In the problem of forced two-dimensional turbulence, the quality of the solution depends on the ratio between the scale of the external forcing and the step of the computational grid. In the experiments with large-scale forcing, the effect of scheme errors on the statistical characteristics of the large scales is insignificant. In the case of small-scale forcing, all schemes reproduce the inverse energy cascade incorrectly. For modelling the inverse cascade, two of the most well-known Casimirs turned out to be key: *the integral vorticity* and *the enstrophy*. Control over these invariants is important to limit the growth of large and small scales:

- Strong violations of the invariance of the integral vorticity lead to the generation of energy at large scales. The invariance is, in the main, violated through small-scale variability, and this leads to the appearance of strongly Fourier-nonlocal interactions between the small-scale and large-scale components of the flow, which are absent in the original equations.
- The generation of enstrophy (for schemes with a single invariant—energy) creates an additional load on the numerical filter (biharmonic viscosity), as a result of which excessive dissipation of energy takes place. To restrict the small scales, the INMCM scheme turns out to be useful, exhibiting selective properties with respect to the dissipation of invariants: it dissipates enstrophy but approximately conserves energy.

Chapter 3. Investigation of the influence of subgrid parameterizations on the reproduction of the inverse energy cascade

In the previous chapter of the dissertation it was shown that, in forced two-dimensional turbulence, the inverse energy cascade is weakened when the scale of the external forcing is chosen in the short-wave range. It is known that the inverse energy cascade is maintained by strongly nonlocal triadic interactions, in which flows comparable in scale with the forcing scale transfer energy directly to large scales corresponding to the inertial interval of the inverse energy cascade [28]. In the cited work the described physical process is called “backscatter”. We shall use the definition “kinetic energy backscatter” (KEB). For the explicit reproduction of KEB in numerical experiments it is necessary that the forcing scale be well resolved on the computational grid. Otherwise, the mentioned triadic interactions will either be absent (insufficient resolution) or weakened (low-order advection approximation).

In this chapter of the dissertation, an analysis is carried out of the interaction between flows resolved and unresolved on the computational grid of the coarse model, taking into account the numerical approximation of advection, and spectral characteristics are constructed describing how the unresolved flows redistribute the energy of the resolved flows. The analysis is carried out on the trajectory of a high-resolution model and is called *a priori analysis*. The forces with which the unresolved scales act on the resolved ones are called *subgrid forces*. To model the energetic effect of the subgrid forces, several KEB parameterizations are proposed.

The KEB defined above is a physical process that is observed in two-dimensional turbulence but is absent in three-dimensional. The existence of KEB follows from two fundamental properties of two-dimensional fluids: enstrophy must be redistributed to small scales, while energy must be redistributed to large scales. If we denote the spectral density of the energy influx from the subgrid forces at wavenumber k by $S(k)$, then the two properties mentioned (in the absence of energy sources at subgrid scales) can be written as follows:

$$\int_0^{k_{max}} S(k)k^2 < 0, \tag{3.1}$$

$$\int_0^{k_{max}} S(k)dk = 0, \tag{3.2}$$

where k_{max} is the maximum wavenumber resolved in the coarse model. From the inequality it follows that there exist wavenumbers for which $S(k) < 0$. From the equality it follows that there exist wavenumbers for which $S(k) > 0$. As shown below, two spectral intervals are usually observed: energy is dissipated by the subgrid forces near the grid scale and is generated on the inertial interval of the inverse energy cascade.

According to [92], on the basis of the characteristic $S(k)$ one can construct an eddy-viscosity parameterization in which the viscosity coefficient depends on the wavenumber:

$$S(k) = -2\nu(k)k^2E(k). \tag{3.3}$$

In [92] it is shown that in three-dimensional turbulence $\nu(k) > 0, \forall k$, while in two-dimensional turbulence the eddy viscosity must be negative on large scales, $\nu(k) < 0$. In [120] it was first proposed to approximate $\nu(k)$ in two-dimensional turbulence by means of a combination of two operators: the Laplace operator with negative viscosity and the biharmonic operator. The viscosity coefficients of these operators were chosen so that the total enstrophy influx from the complete subgrid model would be zero (the case when the grid scale belongs to the inverse-energy-cascade interval was considered). An analogous idea was proposed in [68]; however, the ratio between the viscosity coefficients was chosen so that the total energy influx from the complete subgrid model vanishes (the case when the grid scale belongs to the direct-enstrophy-cascade interval was considered). This way of tuning the KEB parameterization is called "energetically consistent backscatter". It is rather easy to estimate the energetic effect of such a parameterization as a function of resolution. Let the enstrophy flux through the cascade be η. Then, together with enstrophy, the viscosity will dissipate energy in proportion to $\sim \eta/k_{max}^2$. That is, the energetic effect of the KEB parameterization will decrease quadratically with resolution; analogous estimates are given in [68; 121].

Although KEB, as described above, exists only in two-dimensional turbulence, the first works on constructing KEB parameterizations were carried out in three-dimensional turbulence [40; 67; 70]. The energy exchange with the subgrid scales is divided into forward and backward by means of an EDQNM model, with the backward energy transfer corresponding to a stochastic parameterization, "stochastic backscatter". The stochastic return of energy occurs predominantly at small scales, with a spectral density k^4 in the case of three-dimensional turbulence and k^3 in two-dimensional [69]. The stochastic parameterization makes it possible to describe the growth of uncertainty associated with the absence of information about the unresolved scales. Such parameterizations can be used to construct ensemble weather-forecasting models, see

[77]. According to the classical works [40; 67; 70], when stochastic KEB is added it is necessary to increase the eddy viscosity. As a result, by construction, such a parameterization cannot redistribute energy across the wavenumber spectrum. In [43; 122] it is shown that when quasi-two-dimensional flows are sufficiently chaotic, i.e. the mean flows are weak, the addition of stochastic KEB indeed does not affect the distribution of energy over scales. Nevertheless, in the case of significant mean flows, the stochastic parameterization can contribute to the growth of unstable fluctuations [71] and accelerate the achievement of the statistically stationary regime of the solution [73].

Thus, for the reproduction of two-dimensional turbulence one can use two different KEB parameterizations. The first redistributes energy across scales and participates in maintaining the inverse energy cascade; we shall call it *long-wave* KEB. The second takes into account the uncertainty associated with the absence of information about the unresolved scales; we shall call it *short-wave* KEB. In this chapter we shall not consider short-wave KEB parameterizations that mainly act on scales in the enstrophy interval. Preliminary testing of such subgrid models has shown (see Appendix B) that they do not have a substantial effect on the inverse energy cascade. This chapter is devoted to constructing long-wave KEB parameterizations. It is shown that in homogeneous isotropic turbulence the redistribution of energy can be carried out both in a deterministic and in a stochastic way. The question of the choice of the preferable form of the KEB parameterization should be addressed either on the basis of analysis of the ensemble of solutions or on the basis of analysis of experiments in which strong mean flows are observed.

3.1 A priori analysis of subgrid forces

The dynamics of the two-dimensional fluid is described by the equations given in the previous chapter, (2.1), (2.2). The experiment with small-scale forcing described in Section 2.3.2 is considered. Below the definition of the subgrid forces is given and their spectral properties are studied.

Following the large-eddy method (LES, [123]), we write the relation between the fields of dynamical variables for the coarse model ω^h and the high-resolution model ω:

$$\omega^h \equiv \overline{\omega}, \tag{3.4}$$

where the overbar denotes the spectral filter, after the action of which only the Fourier modes of the coarse model in the region of wavenumbers $(-k_{max},k_{max}]^2$ remain nonzero. By means of the discrete Fourier transform the functions $\overline{\omega}$ can be uniquely mapped to the grid of the coarse model $N \times N$, $N = 2k_{max}$. Below we shall assume that one can act on the functions $\overline{\omega}$ both by the usual differential operators and by the discrete operators of the coarse model; for details see [30].

In the a priori tests, among all the right-hand sides of equations (2.1) and (2.2) we consider only advection. The high-resolution model is described by the equation

$$\frac{\partial \omega}{\partial t} = -J(\psi, \omega), \tag{3.5}$$

while the dynamics of the large scales (resolved on the coarse-model grid) obeys the equation

$$\frac{\partial \overline{\omega}}{\partial t} = -\overline{J(\psi, \omega)} = \underbrace{-J^h(\overline{\psi}, \overline{\omega})}_{\text{scheme}} + \sigma \tag{3.6}$$

$$\sigma = \underbrace{-\overline{J(\psi,\omega)} + J^h(\overline{\psi}, \overline{\omega})}_{\text{subgrid forces}}, \tag{3.7}$$

where J^h denotes the numerical discretization in the coarse model. In the variables $(\mathbf{u}, p)$ the subgrid forces can be found in an analogous way:

$$\frac{\partial \overline{\mathbf{u}}}{\partial t} = -\overline{(\mathbf{u} \cdot \nabla)\mathbf{u}} = -[(\overline{\mathbf{u}} \cdot \nabla)\overline{\mathbf{u}}]^h + \boldsymbol{\sigma} \tag{3.8}$$

$$\boldsymbol{\sigma} = -\overline{(\mathbf{u} \cdot \nabla)\mathbf{u}} + [(\overline{\mathbf{u}} \cdot \nabla)\overline{\mathbf{u}}]^h. \tag{3.9}$$

The subgrid forces take into account both the scales unresolved on the grid and the numerical-discretization errors:

$$\boldsymbol{\sigma} = \underbrace{-\overline{(\mathbf{u} \cdot \nabla)\mathbf{u}} + (\overline{\mathbf{u}} \cdot \nabla)\overline{\mathbf{u}}}_{\text{unresolved scales}} \underbrace{-(\overline{\mathbf{u}} \cdot \nabla)\overline{\mathbf{u}} + [(\overline{\mathbf{u}} \cdot \nabla)\overline{\mathbf{u}}]^h}_{\text{discretization errors}}. \tag{3.10}$$

The discretization errors are absent in the spectral scheme; however, for finite-difference methods they can determine the form of the subgrid forces; for more details see [30].

3.1.1 Spectral characteristics of the subgrid forces

For the three finite-difference schemes (INMCM, INMOM, Z) an a priori analysis on the trajectory of the DNS computation at the high resolution 2160×2160 was carried out (the viscosity coefficient was chosen so as to obtain the most extended enstrophy interval). The resolution of the coarse model was chosen equal to 360×360, the forcing scale $k_f = 90$. Figure 3.1(a) shows the spectral density of the resolved advection for the coarse models $\langle |(J^h(\overline{\psi},\overline{\omega}))_k|^2 \rangle$ and the DNS computation $\langle |(\overline{J(\psi,\omega)})_k|^2 \rangle$. The index k denotes the Fourier transform, the angular brackets denote time averaging. From the figure it is seen that on large scales the advection resolved by the coarse models is reproduced correctly, while on small scales strong differences from the DNS computation are observed. Using the formula for the subgrid forces, $\sigma_k = -(\overline{J(\psi,\omega)})_k + (J^h(\overline{\psi},\overline{\omega}))_k$, we obtain that on large scales the subgrid forces are small in amplitude, while on small scales they dominate over the resolved advection. Analogous results are given in [124]. Such a distribution of the subgrid forces across scales is explained by the fact that the maximum approximation errors of the advective terms fall on the small scales, where the phase errors of the numerical discretizations predominate.

Although the amplitude of advection on large scales is reproduced correctly by all the schemes, the equilibrium dynamics of models with low spatial resolution can differ strongly from the dynamics of the DNS model. This happens because of the poor description of the nonlocal triadic interactions.

Figure 3.1(b) shows the spectrum of energy generation by the subgrid forces $-2\pi k \mathrm{Re}\langle \overline{\psi^*}_k \sigma_k \rangle$. The generation and dissipation of energy by the subgrid forces (and, correspondingly, of enstrophy) are separated in spatial scales. On the scales of the direct enstrophy cascade ($k > 90$) the dissipation of a significant fraction of enstrophy (90% of its influx due to the external forcing η) is observed, while on the scales of the inverse energy cascade ($k < 90$) generation of energy is observed (50% of its influx due to the external forcing ε). The unresolved generation of energy in the long-wave range almost coincides for the three schemes under study and corresponds to long-wave kinetic energy backscatter. The largest energetic contribution to KEB falls on the compensation of the approximation errors of the scheme (35% of ε), and the remaining 15% on the compensation of the interaction with the unresolved scales. The underestimated generation of energy in the long-wave range decreases with increasing resolution (at the resolution 720×720 the generation amounts to 15% of the energy influx ε).

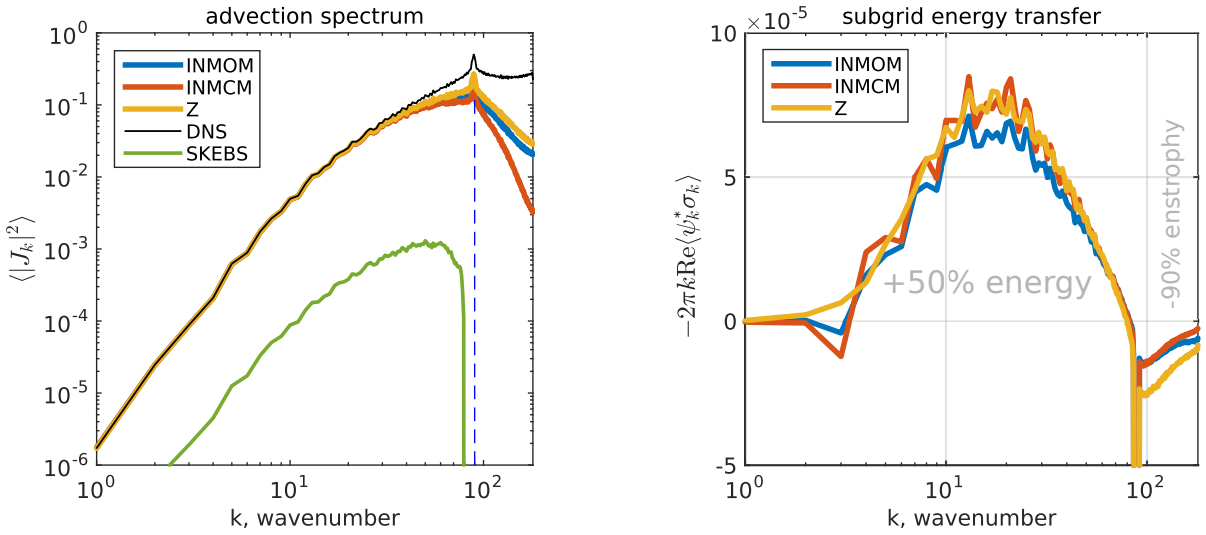

a) b)

Figure 3.1 — Spectral distribution of the resolved advection (a) and spectral distribution of the energy generation by the subgrid forces (b) for the three schemes (INMOM, INMCM, Z) in the a priori test. DNS resolution 2160^2, coarse-model resolution 360^2; the forcing scale is shown by the dashed line. SKEBS denotes the stochastic parameterization. The grey indicates the total generation of quadratic invariants on the direct and inverse inertial intervals, normalized by the influx from the external forcing.

As seen in the figure, the transfer of energy from the subgrid scales is strongly nonlocal in Fourier space: the maximum of the energy generation falls approximately on the middle of the inertial interval of the inverse energy cascade and makes a systematic positive contribution to the energy of the large-scale modes. The absence of this contribution in models with a coarse grid leads to the decay of large-scale variability, as shown in Section 2.3.2, see Figure 2.2(b).

3.1.2 Reproduction of KEB by the scale-similarity model

The spectrum of energy generation by the subgrid forces located on the inertial interval of the inverse energy cascade can be reproduced by means of the scale-similarity model [44], which has the following form:

$$\frac{\partial \overline{u}_i}{\partial t} = \cdots - C_{sim} \frac{\partial}{\partial x_j} (\widetilde{\overline{u}_j \overline{u}_i} - \widetilde{\overline{u}}_j \widetilde{\overline{u}}_i), \tag{3.11}$$

here C_{sim} is a dimensionless coefficient of order 1, $\overline{(\cdot)}$ is the "base" filter defined above, and $\widetilde{(\cdot)}$ is the "test" filter applied to the coarse-model fields $\overline{u}_i$. The test filter is based on a three-point stencil in each direction:

$$F_{x_i}(\varphi) = a\varphi(x_i - h_{x_i}) + (1-2a)\varphi(x_i) + a\varphi(x_i + h_{x_i}), \tag{3.12}$$

where the coefficient $a < 1/2$ determines the filter width $\Delta_F/h_{x_i} = \sqrt{24a}$ [125]. The test filter has the form

$$\widetilde{\varphi} = F_{x_2}(F_{x_1}(\varphi)) = F_{x_1}(F_{x_2}(\varphi)). \tag{3.13}$$

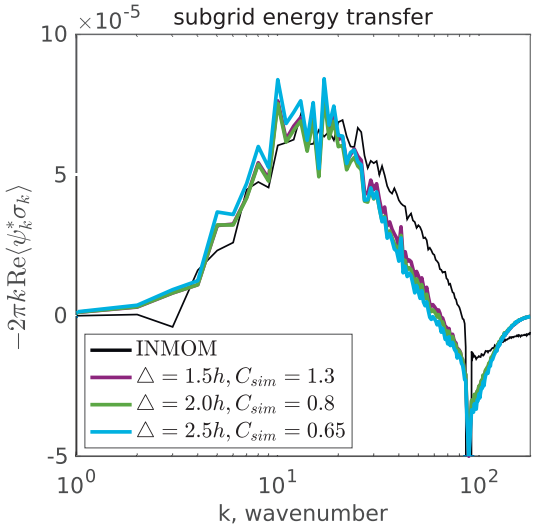

Figure 3.2 — Spectral distribution of the energy generation by the subgrid forces for the INMOM scheme (black line), and also for the scale-similarity models that differ in the width of the test filter Δ and the constant C_{sim}. DNS resolution 2160^2, coarse-model resolution 360^2.

As seen from Figure 3.2, the spectrum of energy generation by the subgrid forces on large scales for the INMOM scheme (black line) is well reproduced by the scale-similarity models (coloured lines) for various test-filter widths $\Delta_F = 1.5h, 2.0h, 2.5h$, with the proper choice of the constant $C_{sim} = 1.3, 0.8, 0.65$. If the small scales are filtered out in the model (3.11), then it can be used to describe KEB.

3.2 Subgrid parameterizations

In this section we describe the scheme-dependent subgrid parameterizations proposed by us, based on the a priori analysis of the scheme errors. As the basic turbulence

model we choose the biharmonic operator, as is done in the original formulation of the problem (2.1), (2.2). The KEB parameterizations are tuned so as to reproduce the spectrum of energy generation by the subgrid forces on the inertial interval of the inverse energy cascade, shown in Figure 3.1(b).

3.2.1 Stochastic parameterization

The stochastic KEB parameterization is based on an autoregressive model, as proposed in [77]. The parameters of the model are chosen so as to reproduce the spectrum of energy generation by the subgrid forces and to reproduce the characteristic times of the subgrid forces, which depend on the modulus of the wavenumber (k).

The dynamical equation in Fourier space, taking into account a certain time approximation, has the following form:

$$\frac{\omega_k^{n+1} - \omega_k^n}{\Delta t} = F_k^n + s_k^n, \tag{3.14}$$

where F_k^n denotes all the right-hand sides, including advection, viscosity and so on, and s_k^n is the stochastic parameterization. n is the time-step index. The stochastic tendency will be modelled by an AR1 process [126]:

$$s_k^{n+1} = \beta_k s_k^n + d_k \varepsilon_k^n,$$

where $\beta_k \in [0,1)$ is the decay coefficient, ε_k^n is white noise in time with unit variance, d_k is the noise amplitude. Since homogeneous turbulence is characterized by statistically independent Fourier coefficients, ε_k^n are also chosen independent for each wave vector. The covariance matrices have the form [126]:

$$\langle \varepsilon_k^m \varepsilon_k^{n*} \rangle = \delta_{m,n}, \quad \langle s_k^m s_k^{n*} \rangle = \beta_k{}^{|m-n|} \frac{d_k^2}{1-\beta_k^2}. \tag{3.15}$$

Here $*$ denotes complex conjugation, and the angular brackets denote averaging over realizations of the random process. From equation (3.15) one can obtain the correlation time τ_k and the variance of the process s_k^n:

$$\tau_k = \frac{\Delta t}{1-\beta_k}, \quad \langle s_k^n s_k^{n*} \rangle = \frac{d_k^2}{1-\beta_k^2}. \tag{3.16}$$

Let us estimate the energetic contribution from the stochastic forcing s_k^n. According to [127; 128], the energy influx ($E_k = \frac{1}{k^2}\omega_k\omega_k^*/2$) on a small time interval Δt has the following form:

$$k^2\frac{\Delta E_k}{\Delta t} = Re\left(\omega_k^n s_k^{n*}\right) + \frac{\Delta t}{2}s_k^n s_k^{n*}. \tag{3.17}$$

The right-hand side of this equation can be expressed through the properties of the stochastic process by substituting the expression for the solution, $\omega_k^n = \Delta t\sum_{m=0}^{n-1}\left(s_k^m + F_k^m\right)$. Assuming that $\langle F_k^m s_k^{n*}\rangle = 0$ (see also [77]), and performing the summation taking into account the form of the covariance matrix (3.15), we obtain:

$$k^2\left\langle\frac{\Delta E_k}{\Delta t}\right\rangle = \lim_{\mathrm{n}\to\infty}\Delta t\left[\frac{1}{2}\left\langle s_k^n s_k^{n*}\right\rangle + \sum_{m=0}^{n-1}\left\langle s_k^m s_k^{n*}\right\rangle\right] = \frac{\Delta t}{2}\frac{d_k^2}{\left(1-\beta_k\right)^2}. \tag{3.18}$$

The decay coefficient β_k is chosen such that the correlation time τ_k coincides with the time of exponential decay of the autocorrelation function of the subgrid forces. The parameter τ_k depends on the wavenumber and decreases in the short-wave range. The amplitude d_k is chosen so as to equate the energy influx from the stochastic parameterization (3.18) with the influx from the subgrid forces on the inertial interval of the inverse energy cascade:

$$\left\langle\frac{\Delta E_k}{\Delta t}\right\rangle = \max\left(-\mathrm{Re}\langle\overline{\psi^*}_k\sigma_k\rangle,0\right). \tag{3.19}$$

The amplitude of the stochastic parameterization is sufficiently small compared with the amplitude of the resolved advection at large scales, see Figure 3.1(a), the green line.

Let us denote by $s^\omega(\mathbf{x},t)$ the stochastic tendency in physical space. The tendency in the velocity–pressure variables can be found as follows:

$$\left(s_1^u, s_2^u\right) = \left(-\frac{\partial}{\partial x_2}, \frac{\partial}{\partial x_1}\right)\Delta^{-1}s^\omega\left(\mathbf{x},t\right). \tag{3.20}$$

3.2.2 Negative-viscosity parameterization

Following [129], we write the linear eddy-viscosity model in Fourier space:

$$\frac{\partial\omega_k}{\partial t} = \cdots - \nu\left(k\right)k^2\omega_k, \tag{3.21}$$

where $\nu(k)$ is the wavenumber-dependent eddy viscosity. The energy influx due to this parameterization has the form

$$\frac{\partial E_k}{\partial t} = \cdots - \nu(k)\,\omega_k^*\omega_k.$$

Negative values of the viscosity ($\nu(k) < 0$) describe energy generation. In order to compare this parameterization with the stochastic one, the viscosity coefficient is chosen as follows:

$$\nu(k) = -\left\langle \frac{\Delta E_k}{\Delta t} \right\rangle / \left\langle \omega_k^*\omega_k \right\rangle,$$

where the spectrum of energy generation ($\left\langle \frac{\Delta E_k}{\Delta t} \right\rangle$) and the solution spectrum ($\left\langle \omega_k^*\omega_k \right\rangle$) correspond to an a posteriori experiment with a coarse model driven by the stochastic parameterization.

3.2.3 Scale-similarity model

In order to remove the dissipation of energy at small scales, the tendency of the model (3.11) is additionally filtered by a spectral filter: Fourier coefficients with large modulus of the wavenumber ($k > 0.9k_f$) are zeroed out. This filter is denoted by $\widehat{(\cdot)}$. In the velocity–pressure variables the model has the form:

$$-C_{sim}\frac{\partial}{\partial x_j}(\widehat{l_{ij}^u}),\ l_{ij}^u = \widetilde{u_j u_i} - \widetilde{u}_j\widetilde{u}_i. \tag{3.22}$$

To construct the test filter, $a = 1/6$ is used in formula (3.12), which corresponds to the filter width $\Delta_F/h = 2$.

In the streamfunction–vorticity variables the model can be written in an analogous way:

$$-C_{sim}\frac{\partial}{\partial x_j}(\widehat{l_j^\omega}),\ l_j^\omega = \widetilde{u_j\omega} - \widetilde{u}_j\widetilde{\omega}. \tag{3.23}$$

The constant C_{sim} was chosen so as to equate the total energy influx from this parameterization with the energy influx from the stochastic parameterization. For the schemes INMOM, INMCM, Z, CCS the following values of C_{sim} were used, respectively: $4.1,\ 1.5,\ 2.3,\ 2.6$.

3.2.4 Combined parameterization: stochastic + scale-similarity model

The combined model is a linear combination of (3.22), (3.23) and the stochastic tendency (3.20):

$$C_{stoch} s_i^u - C_{sim} \delta_{x_j} \widehat{l_{ij}^u}, \tag{3.24}$$

$$C_{stoch} s^\omega - C_{sim} \delta_{x_j} \widehat{l_j^\omega}. \tag{3.25}$$

The optimal choice of the parameters C_{stoch} and C_{sim} is discussed below.

3.3 Numerical experiments

The numerical experiments with the coarse models are carried out analogously to what is described in Section 2.3.2: at the resolution 360×360, biharmonic viscosity $\nu = 2.13 \cdot 10^{-9}$. For each numerical scheme (INMOM, INMCM, Z, CCS) experiments without a KEB parameterization ("no backscatter") and with one of the following parameterizations were carried out: stochastic ("stochastic") 3.2.1, negative-viscosity ("negative visc.") 3.2.2, scale-similarity ("similarity") 3.2.3, combined model ("stochastic+similarity") 3.2.4. In all the experiments with the stochastic parameterization the same spectrum of energy generation was used, corresponding to the Z scheme, see Figure 3.1(b).

Figures 3.3 and 3.4 show the energy spectrum and the compensated energy spectrum (multiplied by $\varepsilon^{-2/3} k^{5/3}$) for the coarse models in comparison with the reference computation (black line). The stochastic parameterization (red line) makes it possible to recover the large scales ($1 < k < 5$); however, the intermediate scales ($5 < k < 90$) are characterized by an underestimated energy level. Increasing the strength of the stochastic parameterization leads to an even greater enhancement of the large scales, but the intermediate scales remain practically unchanged.

The use of the negative-viscosity parameterization (yellow line) leads to analogous results; however, one of the schemes (the Z scheme) turns out to be unstable: small eddies on the scale of the external forcing grow without bound.

The scale-similarity parameterization does not supply enough energy to the large scales, but effectively recovers the energy spectrum at intermediate scales (the cyan

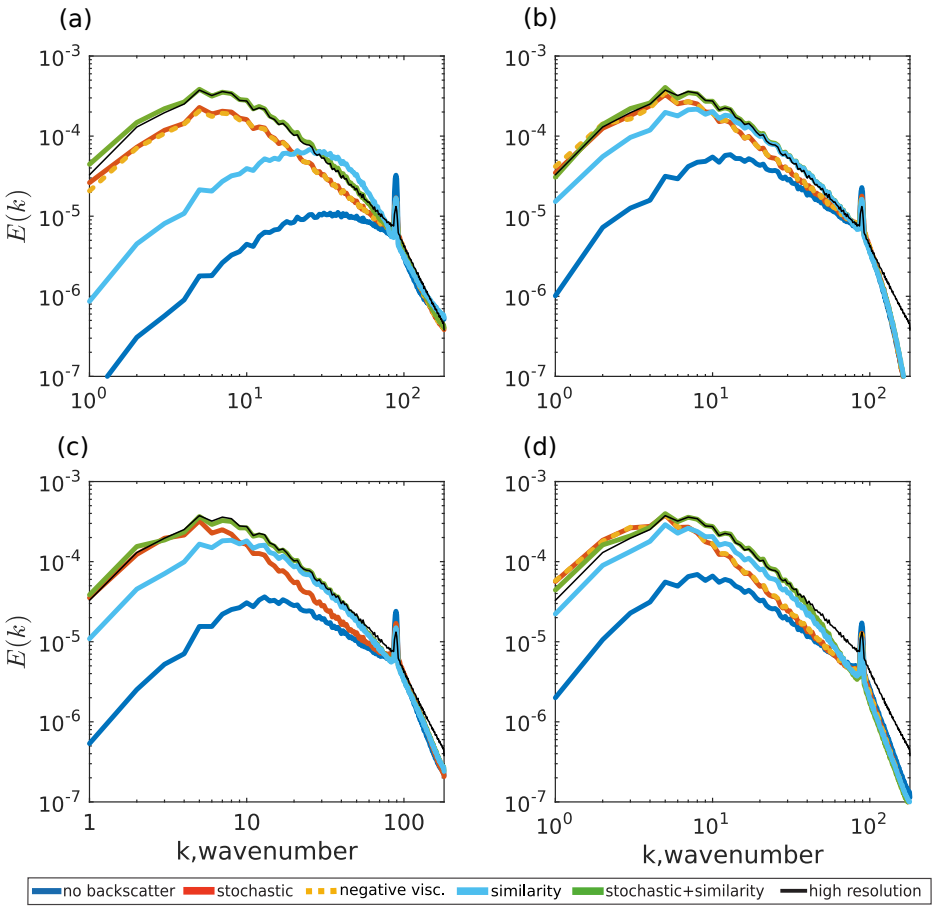

Figure 3.3 — Spectral density of energy of the coarse models for four advection schemes, (a) – INMOM, (b) – INMCM, (c) – Z, (d) – CCS. The black line corresponds to the reference model.

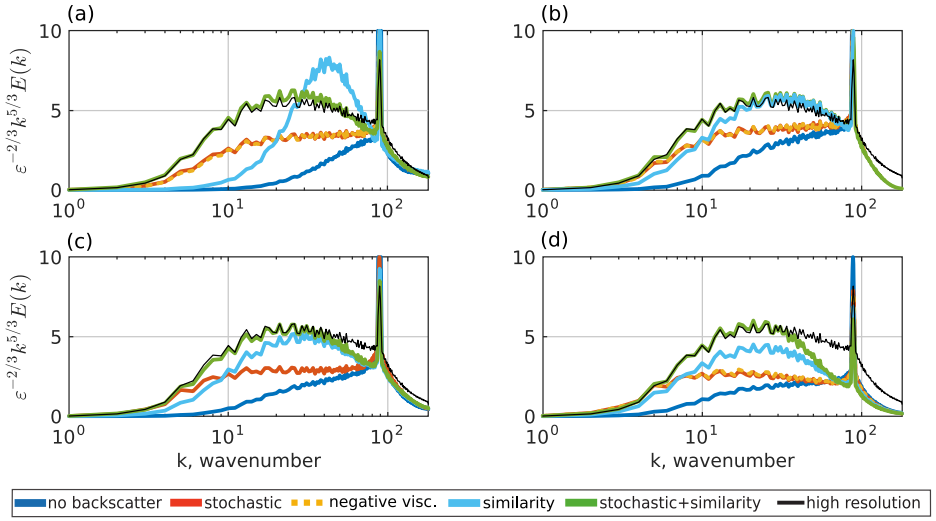

Figure 3.4 — The same as Figure 3.3, but the compensated energy spectrum (multiplied by $\varepsilon^{-2/3}k^{5/3}$) is shown.

line in Figures 3.3 and 3.4). One can expect that the combined model will be able to recover the spectral density of energy at large and small scales. The free parameters in formulas (3.24) and (3.25) were chosen experimentally so as to achieve the best agree-

ment between the energy spectrum of the coarse model and the reference model in the wavenumber range $(1 < k < 40)$. For the schemes INMOM, INMCM, Z, CCS the following values of C_{stoch} and C_{sim} were used: (1.25, 1.7), (0.79, 1.4), (0.76, 2.5) and (0.43, 4.0). With this choice of coefficients, the total energy influx from the combined model turns out to be practically equal to the total dissipation associated with the biharmonic viscosity (as in "energetically consistent KEB", [68]). The use of the combined model makes it possible to correctly reproduce the compensated energy spectrum (see the green line in Fig. 3.4), which on the inertial interval of the inverse energy cascade becomes comparable with the Kolmogorov constant $C_f \approx 6 \pm 0.5$ [130]. The analogous characteristic when using the stochastic parameterization and the negative-viscosity parameterization turns out to be significantly underestimated ($C_f \approx 3 - 4$, the red and yellow lines in Figure 3.4).

Figure 3.5(a) shows a typical realization of the streamfunction in the reference computation. The streamfunction in the coarse model (based on the INMOM scheme) has practically zero large-scale component 3.5(b). The use of the stochastic parameterization and of the negative-viscosity parameterization improves the structure of the flows, see Fig. 3.5(c),(d). The best agreement in the large-scale structure of the flows is observed for the combined model 3.5(e).

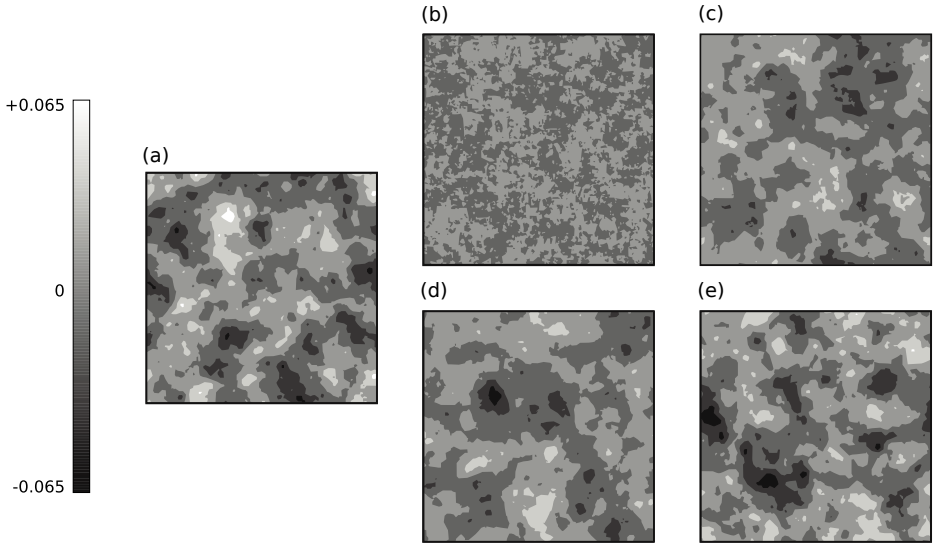

Figure 3.5 — Instantaneous streamfunction of the reference model (a), and of the coarse model with the INMOM scheme without KEB parameterization (b), stochastic parameterization (c), negative-viscosity parameterization (d), combined parameterization (e).

The autocorrelation functions of the solution ω_k and of the advection $(\mathbf{u}\nabla\omega)_k$ at the wavenumber $k = 30$, which corresponds to intermediate scales, are shown in Fig-

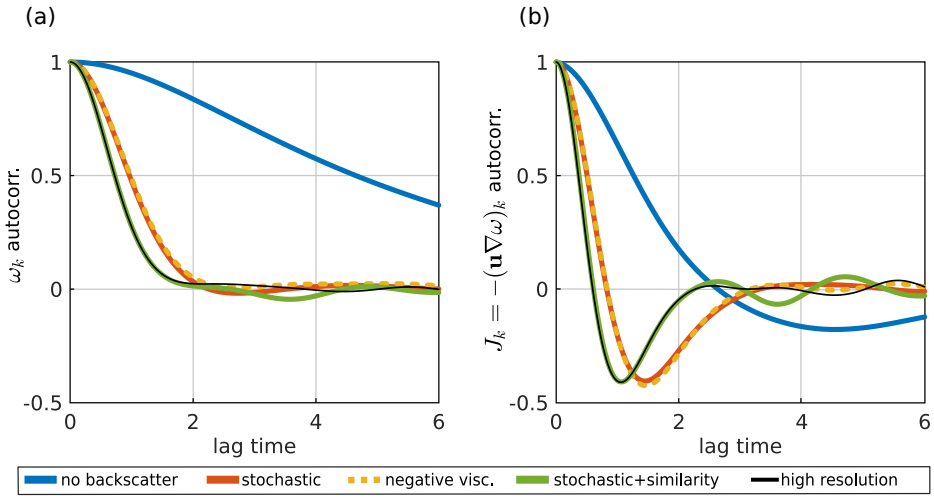

Figure 3.6 — Autocorrelation functions of the Fourier coefficients of the solution (a) and of the advection (b) at wavenumber 30, coarse model with the INMOM scheme.

Table 3 — Relative error in the mean streamfunction, given in two norms.

	$\|\|\langle\psi\rangle - \langle\psi_{DNS}\rangle\|\|_\infty / \|\|\langle\psi_{DNS}\rangle\|\|_\infty$				$\|\|\langle\psi\rangle - \langle\psi_{DNS}\rangle\|\|_2 / \|\|\langle\psi_{DNS}\rangle\|\|_2$			
	INMOM	INMCM	Z	CCS	INMOM	INMCM	Z	CCS
no backscatter	0.83	0.47	0.68	0.58	0.44	0.30	0.39	0.37
stochastic	0.13	0.08	0.09	0.10	0.13	0.11	0.10	0.11
negative viscosity	0.17	0.09	unst.	0.11	0.19	0.13	unst.	0.14
stochastic+similarity	0.07	0.08	0.05	0.05	0.11	0.10	0.07	0.08

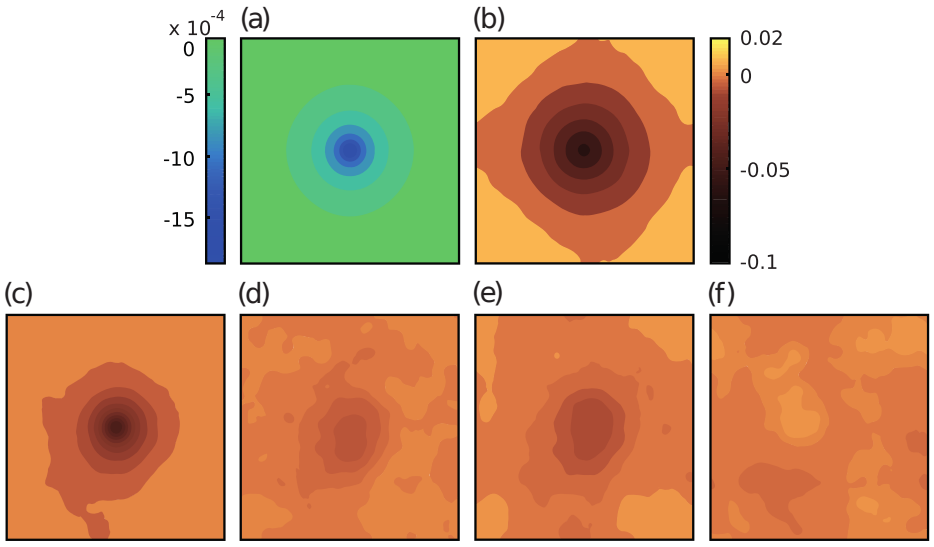

Figure 3.7 — Steady external forcing (a) represented by a streamfunction, mean streamfunction of the reference model (b). Error in the mean streamfunction of the coarse model (INMOM scheme): (c) – without KEB parameterization, (d) – stochastic parameterization, (e) – negative-viscosity parameterization, (f) – combined parameterization.

ure 3.6. The use of the parameterizations makes it possible to reduce the characteristic times of variability, and the best agreement with the reference computation is observed for the combined model.

For climate-modelling problems an important property is the correct description of the sensitivity to a steady external forcing in the coarse model. To compare the sensitivity characteristics, we add to the right-hand side of the dynamical equations a steady forcing that is sufficiently small from the point of view of the systematic energy influx:

$$\frac{\partial \omega}{\partial t} = \cdots + 0.09 \cdot \exp(-70 \cdot [(x_1 - \pi)^2 + (x_2 - \pi)^2]). \tag{3.26}$$

The response of the system to the forcing (3.26) consists in the formation of a mean flow. The mean flow was found by averaging over a period of 24000 time units. The streamfunction of the external forcing (a), the mean flow in the reference model (b) and the errors in the mean for the coarse models (c–f) are shown in Figure 3.7.

The coarse models without a parameterization (Figure 3.7(c)) give errors comparable with the response of the reference model (see the error norms in Table 3). The use of the stochastic parameterization decreases the error (Fig. 3.7(d)). The error when using the negative-viscosity parameterization turns out to be larger compared with the stochastic parameterization (Fig. 3.7(e)). The minimum errors correspond to the combined parameterization (Fig. 3.7(f)).

3.4 Conclusions

In this chapter of the dissertation an a priori analysis of the subgrid forces in the problem of forced turbulence is carried out, with the choice of the external forcing near the grid scale. The analysis is carried out taking into account the numerical advection schemes. It is shown that the subgrid forces exert a systematic energetic action on the scales of the inertial interval of the inverse energy cascade. The underestimated generation of energy in the long-wave range almost coincides for the three second-order finite-difference schemes under study, which makes it possible to use the same parameterizations for all the schemes considered. To model the energetic action, several long-wave KEB parameterizations were tuned. It is shown that such parameterizations are capable of improving the reproduction of the spectral density of energy at large and intermediate scales and of the autocorrelation functions of the solution. As expected, in the absence of mean flows the stochastic parameterization and the negative-viscosity parameterization give analogous results. Differences are observed in the reproduction of the mean flow (sensitivity to the external forcing). Also, the negative-viscosity model can be numerically unstable. It is shown that KEB can be reproduced by means of the scale-similarity model, which leads to a better reproduction of the intermediate scales.

A stochastic parameterization exciting flows on the interval of the enstrophy cascade (short-wave KEB) does not make it possible to improve the reproduction of the inverse energy cascade (see Appendix B).

We note some drawbacks of the scale-similarity model which prevent its application in more realistic problems (the model is not presented in Chapter 5, where the NEMO ocean model is investigated). For modelling KEB with this model, the construction of a selective short-wave filter is required. For real-ocean models with lateral boundaries it would be necessary to construct such a filter in physical space, which is computationally expensive. In addition, when filtering, the problem arises of setting the lateral boundary conditions. Another requirement for the successful application of the model is the presence of an extended inertial interval of the inverse energy cascade, which is not always realized in models of real geophysical flows.

Chapter 4. Investigation of the influence of subgrid parameterizations on the reproduction of barotropic instability

The previous chapter was devoted to the investigation of subgrid parameterizations in the problem of modelling homogeneous isotropic two-dimensional turbulence. Geophysical flows observed in the atmosphere and ocean consist of mean flows and turbulent fluctuations, and subgrid eddies act on both components of the resolved flows. According to [75], the parameterizations constructed in the previous chapter describe the interaction of subgrid turbulent fluctuations with the resolved ones, "eddy–eddy interactions". In the same work it was also proposed to model separately the action of subgrid fluctuations on the resolved mean flows ("eddy–meanfield interactions") by means of a deterministic eddy-viscosity operator. From the distribution of eddy viscosity over wavenumbers it follows that, as in "eddy–eddy" interactions, the eddy viscosity in "eddy–meanfields" interactions is positive at small scales and negative at large ones, with the values of the viscosity being 1.5–2 times smaller than for "eddy–eddy" interactions. In [71; 72] it is pointed out that stochastic subgrid parameterizations can initiate the growth of the instability of the mean flow, thereby contributing to the conversion of the kinetic energy of the mean flow into turbulent kinetic energy.

From the above it follows that subgrid parameterizations can be useful also in problems with a strong mean flow. In this chapter we consider the limiting case in which at the initial moment in time the solution is represented by an unstable stationary barotropic jet flow. Such a problem makes it possible to study the properties of subgrid parameterizations in the case when the turbulent fluctuations have a special form: they are described by equations linearized about the mean flow, and the modes of barotropic instability can be found by spectral analysis. The development of barotropic instability is considered in the statistical sense: an ensemble averaging is performed over realizations of the external stochastic forcing that models the action of mesoscale atmospheric flows on the jet flow in the ocean. The quality of the subgrid parameterizations is assessed by how well the coarse model reproduces the energy of the fluctuations associated with the barotropic-instability modes. The subgrid closures are applied to the whole flow without separating it into mean and fluctuation components, since in realistic problems such a separation is not always possible. The subgrid parameterizations in this chapter are applied to the full flow. In contrast to the previous chapter, all parameterizations are constructed without using the Fourier transform. The negative-viscosity

model and the stochastic model are tuned so as to compensate the dissipation associated with the biharmonic viscosity ("energetically consistent KEB"). In contrast to the previous chapter, the scale-similarity model is applied without an additional spectral filter. The investigation of Hadamard well-posedness for the negative-viscosity parameterization is given in Appendix C.

4.1 Equations and model parameters

Consider equations analogous to (2.1) on the square $\Omega = [0,2\pi)^2$ with periodic boundary conditions:

$$\frac{\partial \mathbf{u}}{\partial t} + (\mathbf{u}\cdot\nabla)\mathbf{u} = -\nabla p + \mathbf{D} + \mathbf{F}, \tag{4.1}$$

$$\nabla\cdot\mathbf{u} = 0, \tag{4.2}$$

where $\mathbf{D}$ is the small-scale dissipation provided by the eddy-viscosity model, and $\mathbf{F}$ is the external stochastic forcing. For numerical discretization the INMOM scheme described in Chapter 2.2.1 is used.

As the initial condition we take the unstable jet flow proposed in [131] with small modifications:

$$u_x|_{t=0} = \exp\left(\frac{\pi^2}{2\sigma^2}\right)\cdot\exp\left[\frac{\pi^4}{2\sigma^2}\cdot\frac{1}{y\cdot(y-2\pi)}\right], \tag{4.3}$$

$$u_y|_{t=0} = 0. \tag{4.4}$$

The spatial mean is subtracted (not shown in the formula). The velocity field (4.3) is infinitely differentiable in Ω and is defined to be zero on the boundaries $y = 0, y = 2\pi$. In the centre of the channel ($y = \pi$) the velocity takes its maximum value, equal to 1, and can be approximated by a Gaussian with variance σ^2: $\exp\left[\frac{\pi^4}{2\sigma^2}\cdot\frac{1}{y\cdot(y-2\pi)}\right] = \exp\left[-\frac{\pi^2}{2\sigma^2} - \frac{1}{2\sigma^2}(y-\pi)^2 + O((y-\pi)^4)\right]$.

4.1.1 Eddy-viscosity model and external forcing

We use the eddy-viscosity model (EVM) [132] based on the biharmonic operator,

$$D_i = -2 \cdot \frac{\partial}{\partial x_j}(\nu \Delta S_{ij}), \tag{4.5}$$

with the Smagorinsky viscosity coefficient $\nu = C_{smag} h^4 |S|$, $C_{smag} = 0.06$ [82]. Here $S_{ij} = \frac{1}{2}\left(\frac{\partial u_i}{\partial x_j} + \frac{\partial u_j}{\partial x_i}\right)$ is the strain-rate tensor, and $|S| = \sqrt{2 S_{ij} S_{ij}}$ is its modulus.

The external forcing **F** imitates the influence of the atmosphere on the ocean in the mesoscale atmospheric range, where the slope of the energy spectrum is $-5/3$, [133]. At each time step we generate the streamfunction of the "atmospheric flow" $\psi^F(x,y)$ in Fourier space with the following distribution of energy ($E = -\frac{1}{2}\int \langle \psi^F \Delta \psi^F \rangle d\Omega = \int E(k) dk$) over wavenumbers: $E(k) = k^{-5/3} \exp[-(k/k^F)^8]$, where k^F is the cut-off wavenumber introduced to ensure rapid convergence of the statistical characteristics with increasing resolution. The Fourier coefficients of the random field ψ^F are statistically independent white noises with discrete time. The force with which the "atmospheric" flow acts on the fluid is chosen by the "bulk" formula: $f_i = u_i^F |\mathbf{u}^F|$, where u_i^F is the velocity corresponding to the streamfunction ψ^F. After subtracting the spatial mean and the divergent component, we obtain the field $\widetilde{f}_i$. The numerical integration of the external forcing is performed by the Euler method. In this case we have a simple formula for the energy influx [127]:

$$F_i = A \widetilde{f}_i, \tag{4.6}$$

$$\langle \frac{\partial |\mathbf{u}|^2/2}{\partial t} \rangle = \cdots + \frac{\Delta t}{2} \langle F_1^2 + F_2^2 \rangle = \cdots + \frac{A^2 \Delta t}{2} \langle \widetilde{f}_1^2 + \widetilde{f}_2^2 \rangle, \tag{4.7}$$

where A is the amplitude of the external forcing, and the brackets $\langle \cdot \rangle$ denote averaging over the ensemble.

4.1.2 Experiment parameters

The equations (4.1), (4.2) are integrated up to $t = 25$ for an ensemble consisting of 100 realizations of the stochastic external forcing. The amplitude A is chosen such

that over the entire computation time the influx of energy from the external forcing is equal to 1% of the energy of the initial state. The reference model has resolution 512×512. A model with intermediate resolution (128×128) is used to demonstrate the convergence of the statistical characteristics. The subgrid parameterizations are analysed for coarse-resolution models (32×32, 64×64). The maximum wavenumber for the coarsest model is 16. The external forcing (**F**) and the initial conditions (4.3) are well resolved on the computational grid. The cut-off wavenumber of **F** is $k^F = 8$. The width of the initial jet is $2\sigma = 1/2$. Taking into account the Fourier transform of the Gaussian distribution, $|\mathbb{F}(u_x|_{t=0})|^2 \sim \exp[-k_y^2\sigma^2]$, the wavenumber of exponential decay of the Fourier coefficients of the jet is $k_y = 4$.

4.2 Statistical characteristics of barotropic instability

The stochastic forcing **F** makes it possible to introduce averaging over the ensemble of realizations, denoted by angular brackets. Then the Reynolds decomposition has the form:

$$\mathbf{u} = \langle \mathbf{u} \rangle + \mathbf{u}', \tag{4.8}$$

where $\langle \mathbf{u} \rangle$ is the mean flow and $\mathbf{u}'$ are the turbulent fluctuations. As a statistical characteristic of the arising turbulent fluctuations we choose the energy of the growing unstable modes of the barotropic instability.

To find the unstable modes, let us pass to the representation of equations (4.1), (4.2) in terms of the streamfunction:

$$\frac{\partial \psi}{\partial t} + \Delta^{-1} J(\psi, \Delta\psi) = f_\psi, \tag{4.9}$$

where $J(\psi, \Delta\psi) = -\dfrac{\partial \psi}{\partial y}\dfrac{\partial \Delta\psi}{\partial x} + \dfrac{\partial \psi}{\partial x}\dfrac{\partial \Delta\psi}{\partial y}$ is the Jacobian, and f_ψ is the stochastic forcing **F** in the streamfunction representation. Let us linearize about the initial flow (4.3), (4.4), which in terms of the streamfunction we denote by $\psi_0(y)$:

$$\frac{\partial \psi'}{\partial t} = A(y)\psi' + f_\psi, \tag{4.10}$$

where $A(y) = \left[\Delta^{-1}\left(\dfrac{d\psi_0(y)}{dy}\Delta - \dfrac{d^3\psi_0(y)}{dy^3}\right)\dfrac{\partial}{\partial x}\right]\psi'$. It is assumed that the Laplace operator acts on the subspace of functions with zero mean value, on which it is invertible.

4.2.1 Numerical solution of the eigenvalue problem

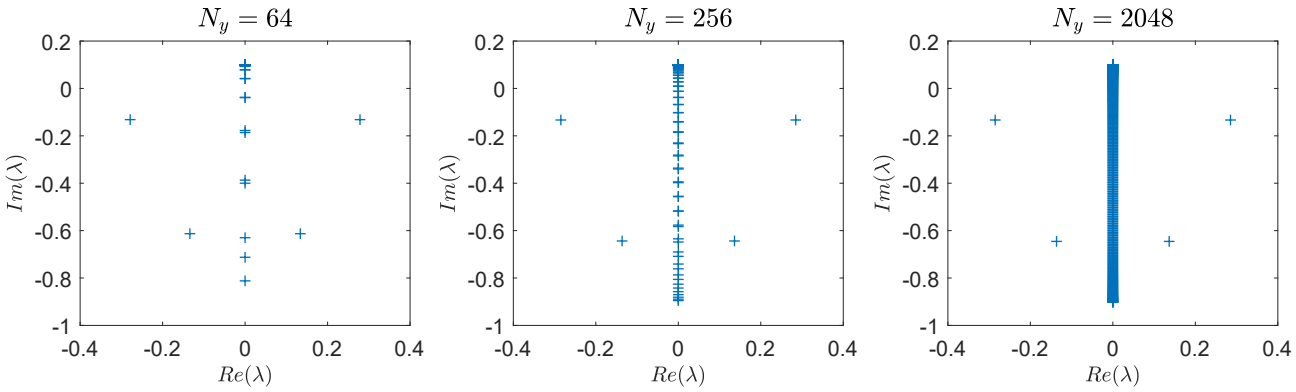

Figure 4.1 — Eigenvalues of the matrix H for $k_x = 1$ for various N_y.

Let us start with the eigenvalue problem $A(y)\Psi(x,y) = \lambda\Psi(x,y)$, which can be simplified taking into account that $A(y)$ does not depend on x. Separating variables, $\Psi(x,y) \equiv \Psi(y)e^{ik_x x}$, where i is the imaginary unit, $k_x \in \mathbb{Z} \setminus 0$ ($k_x = 0$ corresponds to trivial stationary modes), we arrive at the one-dimensional eigenvalue problem for $\Psi(y)$:

$$\left(\frac{d^2}{dy^2} - k_x^2\right)^{-1}\left(\frac{d\psi_0(y)}{dy}\left(\frac{d^2}{dy^2} - k_x^2\right) - \frac{d^3\psi_0(y)}{dy^3}\right)ik_x\Psi(y) = \lambda\Psi(y). \tag{4.11}$$

The eigenvalue problem (4.11) is solved numerically. We introduce a uniform grid along the y direction with N_y nodes and step $h_y = 2\pi/N_y$. The node coordinates:

$$y_j = jh_y,\ j = \overline{0, N_y - 1}. \tag{4.12}$$

The finite-difference approximation of the operator $\dfrac{d^2}{dy^2}$ is represented by the matrix L. E is the identity matrix. The matrices M_1 and M_2 are defined as follows: $M_1 = \mathrm{diag}\left(\dfrac{d\psi_0(y)}{dy}\Big|_{y_i}\right)$ and $M_2 = \mathrm{diag}\left(\dfrac{d^3\psi_0(y)}{dy^3}\Big|_{y_i}\right)$. Then the finite-difference analogue of (4.11) has the form:

$$H(k_x)\Psi = \lambda\Psi,\ \Psi \in \mathbb{C}^{N_y},\ H(k_x) \in \mathbb{C}^{N_y \times N_y}, \tag{4.13}$$

where the matrix H depends on k_x in the following way:

$$H(k_x) = (L - k_x^2 E)^{-1}(M_1(L - k_x^2 E) - M_2)ik_x. \tag{4.14}$$

For $k_x \in \mathbb{N}$ we solve the full eigenvalue problem (4.13). The convergence of the leading eigenvalues, that is, $\max(Re(\lambda))$, with respect to the number of grid nodes N_y is shown in Figure 4.1 for $k_x = 1$. For other k_x analogous figures are obtained. Eigenvalues with $Re(\lambda) > 0$ are separated from the rest of the spectrum and are therefore simple eigenvalues. Due to the special structure of the matrix H ($Re(H) = 0$), these eigenvalues come in pairs: $H\Psi = \lambda\Psi$ and $H\overline{\Psi} = -\overline{\lambda}\,\overline{\Psi}$ (the overbar denotes complex conjugation), and this is seen in Figure 4.1. The eigenvectors of the matrix $H(-k_x)$ coincide with the eigenvectors of the matrix $H(k_x)$, while the eigenvalues change sign. The real-valued unstable mode has the form:

$$\Psi(y)e^{ik_x x}e^{\lambda t} + \overline{\Psi(y)}e^{-ik_x x}e^{\bar{\lambda}t} \equiv 2\mathrm{Re}(\Psi(y)e^{ik_x x}e^{\lambda t}). \tag{4.15}$$

The unstable modes are computed on a grid with $N_y = 2048$ nodes. Among all $k_x \in \mathbb{N}$, the spectrum of $A(y)$ has 8 growing ($Re(\lambda) > 0$) modes. The growth rates of the energy ($2Re(\lambda)$) are given in Table 4. The modes most developed in the numerical experiments are shown in bold and depicted in Figure 4.2. Below we shall distinguish these modes either by wavenumbers ($k_x = 1,2,3$) or by ordinal numbers (the 1st, 2nd, 3rd mode).

Table 4 — Energy growth rates of the unstable modes for various k_x.

k_x	1	2	3	4	5
$2Re(\lambda)$	**0.5704**	**0.9861**	**1.0539**	0.7949	0.2682
	0.2732	0.3414	0.0864		

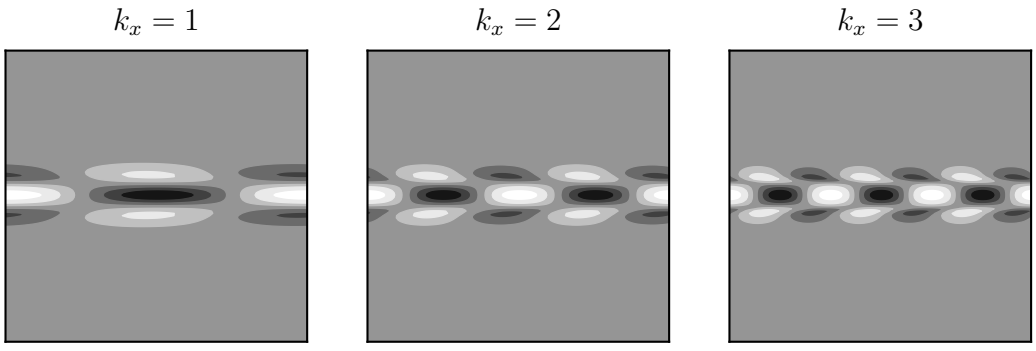

Figure 4.2 — The unstable modes of the operator $A(y)$ most developed in the numerical experiments, in the vorticity representation (real part). Negative values are shown in black, positive in white.

4.2.2 Definition of the energy of the unstable mode

The numerical solutions of the nonlinear equations (4.1), (4.2) are decomposed into the mean flow and the fluctuations about it according to the decomposition (4.8). The fluctuations ψ' are expanded in the basis of eigenfunctions of the operator $A(y)$:

$$\psi' = \sum_i \alpha_i \Psi_i(x,y). \tag{4.16}$$

Since the basis is non-orthogonal, to perform the projection onto the unstable mode $\Psi_i(x,y)$ we use the scalar product with the left eigenvector of the matrix $H(k_x)$. The expression for the energy of the unstable mode has the form:

$$E_i = \frac{|\alpha_i^2|}{2} \int |2Re(\nabla\Psi)|^2 d\Omega. \tag{4.17}$$

4.2.3 Growth of the unstable mode in the presence of external stochastic forcing

Projecting the solution of equation (4.10) onto the subspace spanned by the unstable mode, we arrive at the following equation for the amplitude of the unstable mode α:

$$d\alpha = \lambda\alpha dt + \sigma dW, \ \alpha(0) = 0, \tag{4.18}$$

where σdW is the projection of the stochastic forcing f_ψ onto the subspace, $\sigma > 0$, W is a complex Wiener process, i.e. $\langle \overline{dW} dW \rangle = dt$. Solving (4.18) for the growing modes ($Re(\lambda) > 0$), we obtain the following expression for α [134]:

$$\langle |\alpha(t)|^2 \rangle = \frac{\sigma^2}{2Re(\lambda)} (e^{2Re(\lambda)t} - 1). \tag{4.19}$$

Let us define the ensemble-averaged energy of the unstable mode $\Psi(x,y)$,

$$\langle E \rangle = \frac{\langle |\alpha|^2 \rangle}{2} \int |2Re(\nabla\Psi)|^2 d\Omega \tag{4.20}$$

and the generation of energy of the unstable mode due to the stochastic forcing, $\varepsilon = \frac{\sigma^2}{2} \int |2Re(\nabla\Psi)|^2 d\Omega$. Then for the ensemble-averaged energy of the unstable mode we have the following expression:

$$\langle E(t) \rangle = \frac{\varepsilon}{2Re(\lambda)} (e^{2Re(\lambda)t} - 1). \tag{4.21}$$

From the formula it follows that under the action of the external forcing **F** the energy of the unstable mode grows with the increment $2Re(\lambda)$, with the pre-exponential factor proportional to the power of the forcing, ε.

4.2.4 Overview of the computational results at various resolutions

This section shows how the coarse-resolution models reproduce the barotropic instability.

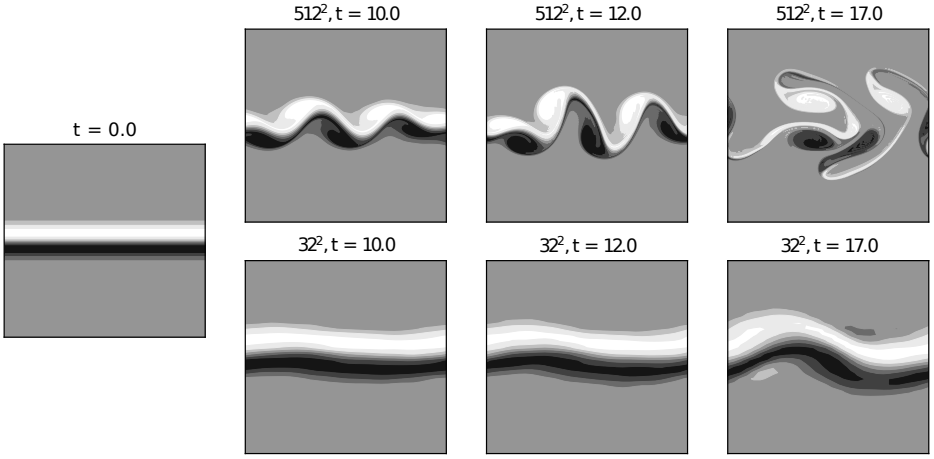

Figure 4.3 — Vorticity at different moments in time. Reference model (512^2) on top, coarse model (32^2) below. Negative values in black, positive in white.

The equations (4.1), (4.2) are solved numerically, the parameters are given in Section 4.1.2. The solutions for the reference (512^2) and coarse (32^2) models for two different realizations of the external forcing **F** are shown in Fig. 4.3. The stochastic forcing excites the unstable modes, which grow exponentially up to $t \approx 10.0$ (in the reference model), after which a transition to the turbulent regime occurs. In the coarse model (32^2) the growth of the instability is slowed down, since a larger-scale mode with a smaller growth increment turns out to be the most developed. We note that the eddy-viscosity model (EVM) strongly smooths the jet flow.

Figure 4.4 shows the energy of the fluctuations (a) and the energy of the unstable modes (b–d) in % of the initial energy of the jet. As the resolution is increased, these statistical characteristics converge.

Let us first describe the results for the reference model (512^2). The observed growth increment of the energy agrees with the theoretical one. The vertical shift of the section of linear growth (on a logarithmic scale) is determined by the incoming power

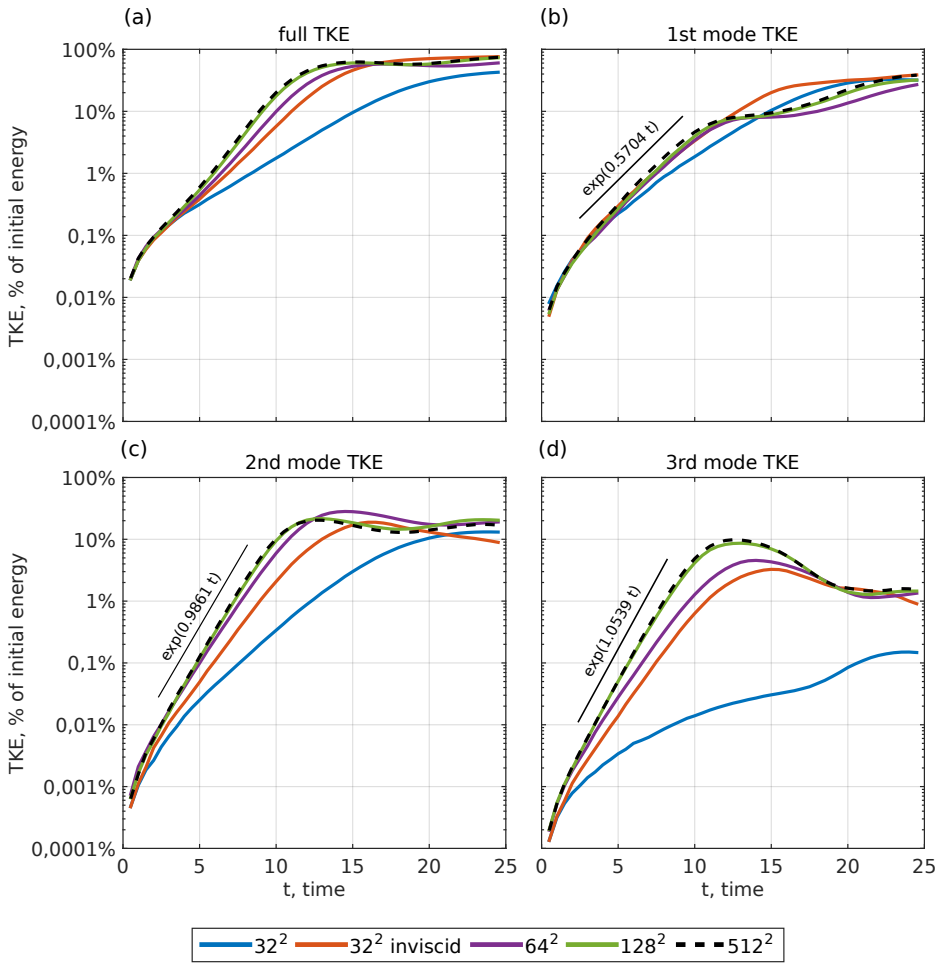

Figure 4.4 — Kinetic energy of the fluctuations (a) and energy of the unstable modes $k_x = 1,2,3$ respectively (b), (c), (d), in % of the initial energy of the jet. The red line corresponds to the computation at resolution 32^2 with the eddy viscosity switched off.

of the external forcing (see formula (4.21)). At the moment of transition to the turbulent regime, the second and third modes, which have the maximum increment, turn out to be the most developed.

The coarse-resolution models $(32^2, 64^2)$ demonstrate an underestimated level of fluctuation energy, see Fig. 4.4 (a). This is explained by the slowing down of the growth of the second and third modes, see Fig. 4.4 (c,d). Let us consider two reasons for this slowing: the action of the eddy-viscosity model (EVM) and the numerical approximation errors. In order to exclude the influence of the EVM, a computation with an inviscid fluid was carried out, the red line in the figures. From the figures it follows that the decisive role in the slowing of the growth is played by the eddy-viscosity model, which can act on the system in two ways: smooth the mean flow and modify the linearized system. Additional experiments with the linearized model showed that the smoothing of the mean flow is of decisive importance.

4.3 Models of subgrid two-dimensional turbulence

4.3.1 Negative-viscosity model

According to [68], let us consider a term added to the right-hand side of equation (4.1):

$$\mu(t)\Delta\mathbf{u}, \tag{4.22}$$

where $\mu(t) < 0$ is chosen at each time step so as to compensate the energy dissipation by the EVM:

$$\int \mathbf{D}\cdot\mathbf{u}\, d\Omega + \mu(t)\int \Delta\mathbf{u}\cdot\mathbf{u}\, d\Omega = 0, \tag{4.23}$$

D was defined in (4.5).

4.3.2 Stochastic model

At each time step, two random fields with uniform distribution on $(0,1)$ are generated, $\mathbf{s} = (s_1, s_2)$. From each field the spatial mean is subtracted, after which the divergent part is subtracted. Then a spatial filter is applied 6 times, defined in formula (3.13) with parameter $a = 1/6$. The spatial filtering of the stochastic tendency was proposed in [72; 84]. This number of filter applications makes it possible to choose the scale of the maximum spectral density to be approximately 5 grid steps. We denote by $(\widetilde{s}_1, \widetilde{s}_2)$ the stochastic tendency after all the indicated operations.

The amplitude of the stochastic forcing A is chosen so as to compensate the dissipation of the EVM:

$$\int \mathbf{D}\cdot\mathbf{u}\, d\Omega + |\Omega|\frac{A^2\Delta t}{2}\langle\widetilde{s}_1^2 + \widetilde{s}_2^2\rangle = 0, \tag{4.24}$$

where $|\Omega| = 4\pi^2$ is the area of the domain.

4.3.3 Scale-similarity model

The scale-similarity model (SS) has the form [44]:

$$-C_{sim}\frac{\partial}{\partial x_j}\left(\widehat{u_i u_j}-\widehat{u}_i\widehat{u}_j\right), \tag{4.25}$$

where $\widehat{(\cdot)}$ denotes one application of the filter (3.13) with parameter $a = 1/6$, $C_{sim} = 3$.

4.3.4 Comparative analysis of the parameterizations

In contrast to the previous chapter, where each subgrid model modelled KEB, in the present problem the parameterizations act on the mean flow and on the fluctuations in different ways.

The stochastic model does not modify the mean flow or the linearized system, but excites the unstable modes, i.e. it increases the pre-exponential factor in formula (4.21). Nevertheless, a multitude of modes that are not developed in the original formulation of the problem is excited.

The negative-viscosity model, like the eddy-viscosity model, acts predominantly on the mean flow. Energy is returned to the mean flow, as a result of which its smoothing is prevented.

The scale-similarity model does not influence the mean flow, since (4.25) is equal to zero for $u_i = U(y)\delta_{i,1}$, where $\delta_{i,j}$ is the Kronecker symbol. However, the model modifies the linearized system and, as will be shown in the numerical experiments, increases the growth increments of the energy of the unstable modes.

4.4 Numerical experiments

In the figures the following notation is used: “bare” denotes the model without an additional subgrid parameterization, “neg.visc” denotes the negative-viscosity model, “SS” denotes the scale-similarity model, “negvisc+SS” denotes the combination of the

negative-viscosity model and the scale-similarity model, “stoch” denotes the stochastic parameterization.

The results for the 32^2 model with the parameterizations are shown in Fig. 4.5. The negative-viscosity and scale-similarity parameterizations make it possible to increase the growth increments of the energy of the 2nd and 3rd unstable modes in an analogous way. The growth of the 1st mode is better reproduced by the model with the scale-similarity parameterization. Since these parameterizations act on the mean flow and on the fluctuations differently, they can be applied together. The combined model (neg.visc + SS) substantially improves the fluctuation energy and the energy of the 1st and 2nd modes; nevertheless, the 3rd mode still remains insufficiently developed. As follows from Figure 4.6, the combined model significantly improves the spatial structure of the solution.

The results for the model with resolution 64^2 are shown in Fig. 4.7. The deterministic models (neg.visc, SS, neg.visc. + SS) practically do not change the energy of the 1st and 2nd modes. The reproduction of the 3rd mode is significantly improved by the models based on the scale-similarity model. As seen in Fig. 4.7 (b–d), the stochastic parameterization modifies the pre-exponential factors (vertical shift). This effect indeed makes it possible to accelerate the onset of the turbulent regime; however, a multitude of modes that do not arise in the reference solution is excited, see the fluctuation energy in Figure 4.7 (a). At resolution 32^2 this effect is manifested even more strongly. As a result, one can conclude that the strength of the stochastic parameterization turns out to be too large for this experiment.

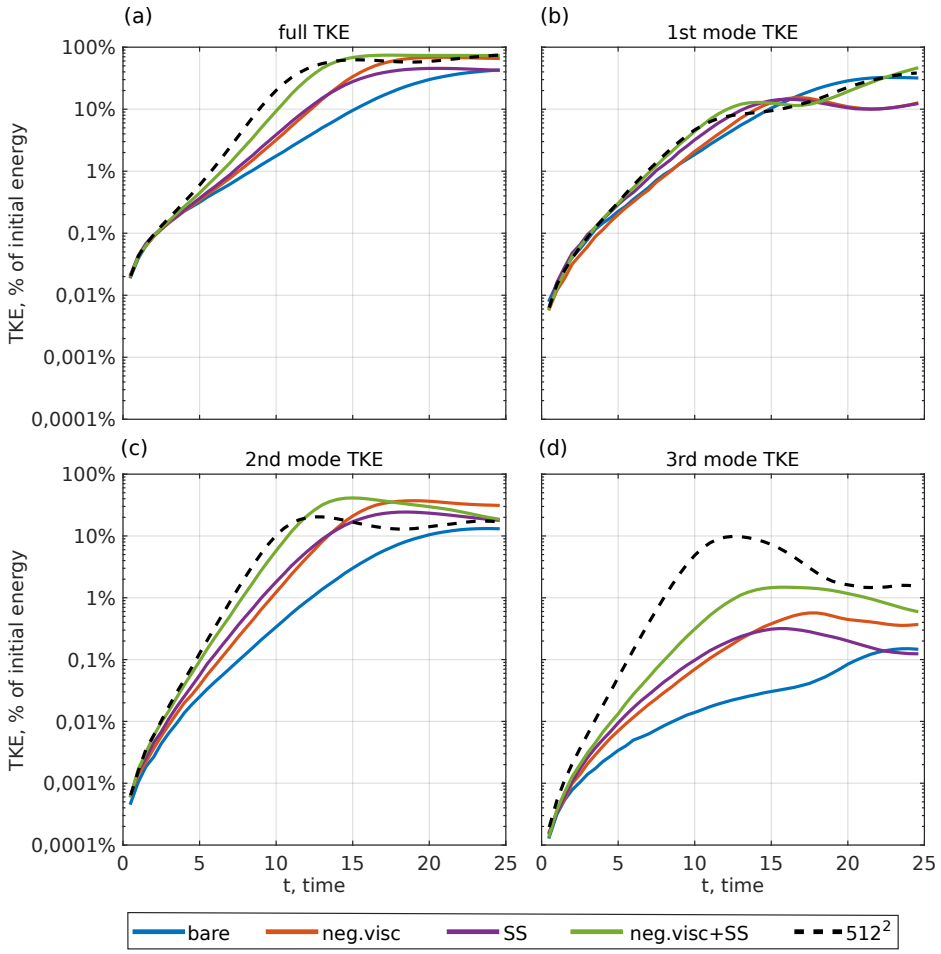

Figure 4.5 — Kinetic energy of the fluctuations (a) and energy of the unstable modes $k_x = 1,2,3$ respectively (b), (c), (d), in % of the initial energy of the jet. The results are shown for the models at resolution 32^2. The black line is the reference computation for the model at resolution 512^2.

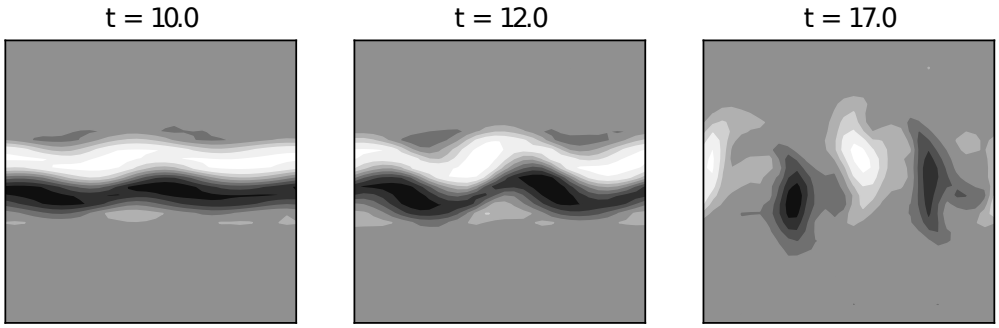

Figure 4.6 — Vorticity at different moments in time. Model at resolution 32^2 with the combined (neg.visc. + SS) parameterization. Negative values are shown in black, positive in white.

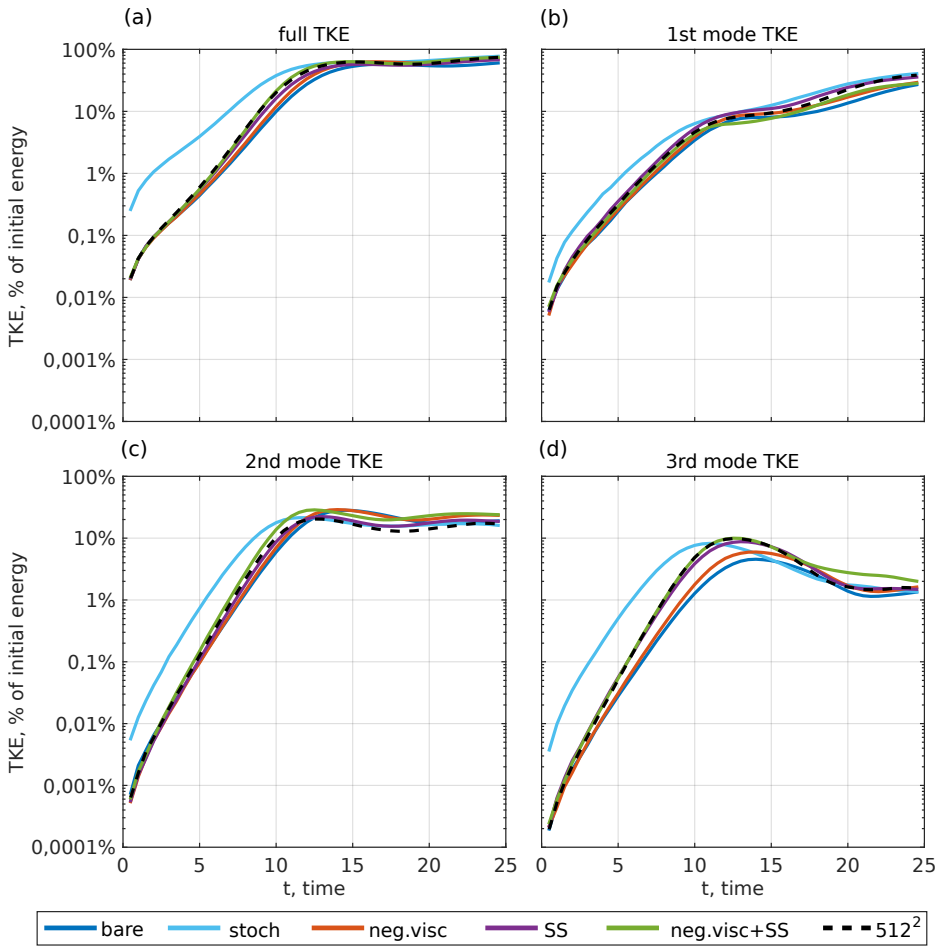

Figure 4.7 — Analogous to Figure 4.5, but for resolution 64^2. The additional cyan line corresponds to the stochastic parameterization.

4.5 Conclusions

Barotropic instability is reproduced incorrectly by the coarse models: larger-scale unstable modes are excited than in the reference computation. The main reason for the suppression of the small-scale modes is the smoothing of the mean flow by the eddy-viscosity model. It is shown that the subgrid parameterizations that were tuned in the previous chapter to model KEB can be applied in a problem with a strong mean flow. The three parameterizations (stochastic tendency, negative-viscosity model, scale-similarity model) act differently on the mean flow and on the fluctuations in the problem of modelling barotropic instability.

The stochastic model excites the unstable modes but does not change the mean flow or the linearized system. It is capable of advancing the moment of onset of turbulence; however, the strength of such a parameterization turns out to be too large.

The negative-viscosity model contributes to the preservation of the energy of the mean flow, which prevents its smoothing by the eddy-viscosity model. This effect leads to the increase of the growth increments of the unstable modes, as a result of which the moment of onset of turbulence is advanced.

The scale-similarity model modifies the linearized system, which leads to an increase of the growth increments of the unstable modes, as a result of which the moment of onset of turbulence is advanced.

The negative-viscosity and scale-similarity models can be applied together, since they act independently on the mean flow and on the fluctuations, respectively.

Chapter 5. Subgrid parameterizations in the Double Gyre model configuration of the NEMO ocean model

The greater part of the kinetic energy of oceanic flows is represented by the eddy kinetic energy [10]. "Eddy-permitting" ocean models only partially resolve the scale of baroclinic instability (the internal Rossby radius of deformation), as a result of which the density of kinetic energy turns out to be underestimated on all scales compared to eddy-resolving models [13]. In the cited work two main reasons for the insufficient development of mesoscale eddies are identified: the conversion of available potential energy into kinetic energy is weakened and the inverse cascade of kinetic energy is weakened. As shown in Chapter 3, KEB parameterizations are capable of restoring the redistribution of kinetic energy into large scales.

In this chapter, KEB parameterizations in the primitive equations of the ocean are considered on the basis of the NEMO model [85]. As the model configuration, the Double Gyre configuration is chosen. To improve the dynamics of the eddy-permitting model ($1/4^o$), two parameterizations are constructed: negative viscosity and stochastic tendency. Both parameterizations modify the evolution equation of the horizontal velocity. The parameterizations belong to the "energetically consistent KEB" class, i.e. they compensate the dissipation caused by the biharmonic viscosity. The local balance between generation and dissipation for the negative-viscosity parameterization is achieved by introducing an additional equation for the subgrid kinetic energy [82], and for the stochastic parameterization by multiplying the stochastic tendency by the square root of the local energy dissipation [77]. The investigation of Hadamard well-posedness for the negative-viscosity parameterization is given in Appendix C. In this chapter it is shown that such parameterizations are capable of restoring the eddy activity, in particular, the amount of eddy kinetic energy and the eddy heat flux. Improvements are also found in the mean fields: sea-surface temperature and the streamfunction of the meridional overturning circulation.

In this chapter the free parameters of the parameterizations are chosen so as to achieve the best agreement between the eddy-permitting and eddy-resolving models. The spectral analysis of the constructed parameterizations and the comparison with the spectral characteristics of the subgrid forces are given in the next chapter of the dissertation.

5.1 The Double Gyre configuration

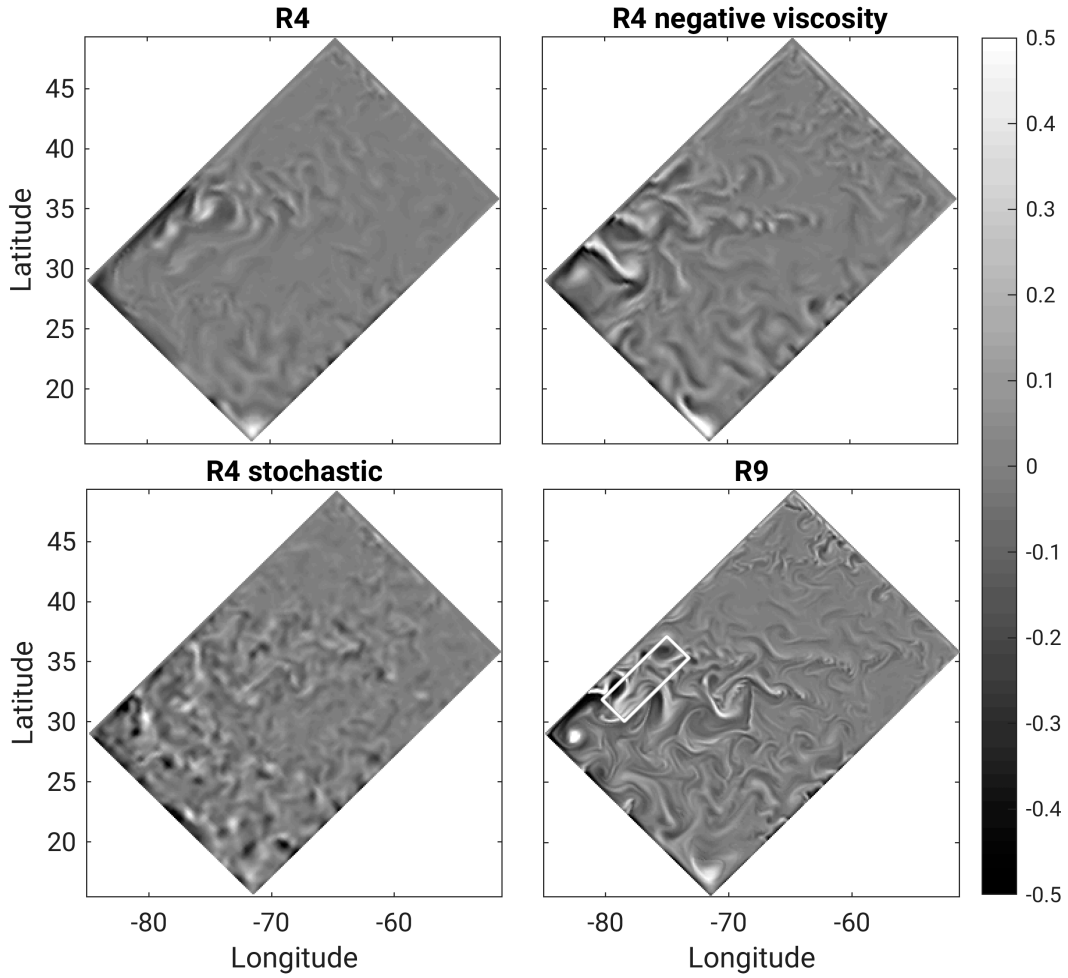

Figure 5.1 — Instantaneous field of relative vorticity in units of the Coriolis parameter (f). March 30 after the model spin-up. R4 is the eddy-permitting model, R9 is the eddy-resolving model, R4 negative viscosity and R4 stochastic are eddy-permitting models with KEB parameterizations. The colour scale saturates at the values ± 0.5. The white square is explained in Figure 5.10.

We use the NEMO ocean model (version 3.6) [85] in the Double-Gyre configuration, which is described in [135]. The model is based on the primitive equations of

the ocean (vectors are denoted in bold):

$$\frac{dT}{dt} = F_T, \ \frac{dS}{dt} = F_S, \tag{5.1}$$

$$\frac{\partial \mathbf{U}_h}{\partial t} + \mathrm{adv}_h + \mathrm{cor}_h = -\frac{1}{\rho_0}\nabla_h p + \mathbf{F}_{\mathbf{U}_h}, \tag{5.2}$$

$$\frac{\partial \eta}{\partial t} = -H\nabla_h \overline{\mathbf{U}}_h, \tag{5.3}$$

$$\frac{\partial p}{\partial z} = -\rho g, \ \nabla \cdot \mathbf{U} = 0, \tag{5.4}$$

$$\rho = \rho_0(1 - a(T - T_0) + b(S - S_0)), \tag{5.5}$$

where T,S,$\mathbf{U}$,η,ρ,p are temperature, salinity, velocity, free-surface elevation, density and pressure; $\mathbf{U}_h$ is the horizontal part of the velocity, and $\overline{\mathbf{U}}_h$ is its vertical average. F_T,F_S,$\mathbf{F}_{\mathbf{U}_h}$ are external forcings and physical parameterizations. The Lagrangian derivative is denoted by $\frac{d}{dt} = \frac{\partial}{\partial t} + (\mathbf{U} \cdot \nabla)$, $\nabla = (\partial_x,\partial_y,\partial_z)$, and its horizontal part by $\nabla_h = (\partial_x,\partial_y)$. The exact expressions for the advection and Coriolis force (adv_h and cor_h) are given in [85]. For scalar and momentum advection, respectively, a TVD scheme and an energy-conserving scheme in vector-invariant form are used, see [85]. In our configuration the free-surface equation (5.3) and the equation of state (5.5) are linear. The parameters of the equation of state are as follows: $\rho_0 = 1026\ \mathrm{kg} \cdot \mathrm{m}^{-3}$, $a = 2 \cdot 10^{-4}\ \mathrm{K}^{-1}$, $b = 7.7 \cdot 10^{-4}\mathrm{psu}^{-1}$, $T_0 = 10C^o$, $S_0 = 35\mathrm{psu}$. The computational domain is rectangular with a flat bottom, $L_x \times L_y \times L_z = 3180\ \mathrm{km} \times 2120\ \mathrm{km} \times 4\ \mathrm{km}$. For the Coriolis force the beta-plane approximation is used, $\beta = 1.8 \cdot 10^{-11}\ \mathrm{m}^{-1} \cdot \mathrm{s}^{-1}$. The horizontal boundary conditions are as follows: free slip (the relative vorticity is zero on the boundary), zero heat and salt fluxes through the horizontal boundary. The bottom friction is described by a quadratic law. The centre of the computational domain corresponds to $\sim 30^oN$, with the computational domain rotated by 45^o with respect to the zonal direction. We note that the metric terms corresponding to the spherical geometry are absent. In latitude–longitude coordinates the computational domain is shown in Figure 5.1.

The following boundary conditions are set on the free surface. The zonal wind, which has the maximum eastward speed at latitude 36^oN and the maximum westward speed at 22^oN. The heat flux from the atmosphere into the ocean is expressed by the formula $Q = \gamma\,(T_{atm} - T_{SST})$, where T_{SST} and T_{atm} are the near-surface temperature of the ocean and of the atmosphere respectively, $\gamma = 40\ \mathrm{W} \cdot \mathrm{m}^{-2} \cdot \mathrm{K}^{-1}$. The solar-radiation flux and the fresh-water flux are also specified. The external forcings depend

Table 5 — Parameters of the R1 (non-eddy-resolving), R4 (eddy-permitting), R9 (eddy-resolving) models. The turbulent diffusion in the R1 model acts along the isoneutral direction. All other diffusion and viscosity operators are horizontal.

	R1	R4	R9
$n_x \times n_y \times n_z$	$30 \times 20 \times 30$	$120 \times 80 \times 30$	$270 \times 180 \times 30$
grid step	1^o, 106 km	$1/4^o$, 26.5 km	$1/9^o$, 11.7 km
time step	120 min	30 min	800 s
diffusion	∇_h^2, 10^3 m^2/s	∇_h^4, -10^{10} m^4/s	∇_h^4, -10^9 m^4/s
viscosity	∇_h^2, 10^5 m^2/s	∇_h^4, $-5 \cdot 10^{11}$ m^4/s	∇_h^4, $-5 \cdot 10^{10}$m^4/s

on the latitude and on the season and are given in [135]. The internal Rossby radius of deformation is equal to 50 km in the south and 15 km in the north.

We consider models at three uniform spatial resolutions. The experiment parameters are given in Table 5. The initial velocity field in the R1 model is zero, and the temperature and salinity have a vertical profile applied throughout the entire computational domain [135]. First the R1 model is run for 1000 years, then the computation continues in the R4 and R9 models for 120 years. The last 20 years are used for the analysis of the statistical characteristics of the solution. The diffusion and viscosity coefficients in the R1 and R9 models are taken from [135]. The choice of these coefficients in the R4 model is discussed below.

5.2 Subgrid parameterizations

5.2.1 Negative-viscosity model

This parameterization supplements the biharmonic viscosity in equation (5.2) with an additional term in the form of viscosity with a negative coefficient, which returns energy, as proposed in [68]:

$$\frac{\partial \mathbf{U}_h}{\partial t} = \ldots \nu_4 \nabla_h^4 \mathbf{U}_h + \nabla_h \left(\nu_2 \nabla_h \mathbf{U}_h \right). \tag{5.6}$$

Here it is assumed that the operator ∇_h acts on vectors componentwise. When $\nu_4 < 0$, numerical noise is effectively dissipated. The coefficient $\nu_2 \leqslant 0$ must be negative in

order for energy to be returned. To take into account the spatial inhomogeneity of the modelled turbulence and the weak dynamics near the bottom, we follow [78; 79; 82] and introduce a dependence of the negative-viscosity coefficient on the coordinates, $\nu_2(x,y,z,t) \leqslant 0$. The coefficient ν_2 is chosen so as to balance the dissipation associated with the biharmonic viscosity. The energy fluxes into the subgrid scales associated with the biharmonic viscosity and with the negative-viscosity model, respectively:

$$\dot{E}_{diss} = \nu_4 \nabla_h \mathbf{U}_h \cdot \nabla_h \left(\nabla_h^2 \mathbf{U}_h \right), \tag{5.7}$$

$$\dot{E}_{back} = \nu_2 \nabla_h \mathbf{U}_h \cdot \nabla_h \mathbf{U}_h. \tag{5.8}$$

The fluxes are chosen in Galilean-invariant form. Integrally over the domain, these fluxes have the following signs: $\int \dot{E}_{diss} dxdydz > 0$, $\int \dot{E}_{back} dxdydz \leqslant 0$. The local equating of these fluxes, $\dot{E}_{diss}(x,y,z,t) + \dot{E}_{back}(x,y,z,t) = 0$, leads to an ill-posed problem for finding ν_2 if $|\nabla_h \mathbf{U}_h| = 0$. To overcome this problem, in [78; 82] it is proposed to introduce an equation for the subgrid kinetic energy ($e \equiv e(x,y,z,t)$), which is generated by the dissipation ($\dot{E}_{diss}$) and consumed by KEB ($\dot{E}_{back}$):

$$\frac{de}{dt} = c_{diss} \dot{E}_{diss} + \dot{E}_{back} + \nu_e \nabla_h^2 e. \tag{5.9}$$

Here d/dt is the Lagrangian derivative (taking into account the advection of the subgrid energy by the resolved flow), which is implemented in the code by means of the simplest upwind scheme [85]; the diffusion of the subgrid energy $\nu_e = 1000\ \mathrm{m}^2 \cdot \mathrm{s}^{-1}$ is equal to the eddy diffusion in the R1 model. Unlike [78], we apply the Lagrangian derivative instead of the partial one. The use of the Lagrangian derivative for modelling the propagation of the subgrid energy was first proposed in [136] and, in our view, describes this process in more detail. Nevertheless, experiments with the advection of e switched off give similar results. As in [79], a tunable parameter $c_{diss} \in (0,1)$ is introduced, which makes it possible to decrease the amount of returned energy. Its optimal value in the R4 model is the following: $c_{diss} = 0.8$. A further increase leads to an overestimated meridional eddy heat flux at the surface at the detachment point of the wall-bounded current. The subgrid energy e defines the negative-viscosity coefficient according to the following formula:

$$\nu_2 = -c_{back} \Delta x \sqrt{\max(e,0)}, \tag{5.10}$$

where Δx is the grid step and $c_{back} = 0.4\sqrt{2}$, as proposed in [82]. Despite the fact that $\int \dot{E}_{diss} dxdydz > 0$, the local values of $\dot{E}_{diss}$ can be negative, which locally can lead to negative values of the subgrid energy. The introduction of the function $\max(\cdot,\cdot)$

switches off the KEB parameterization at such points of the computational domain. For the operators $\nabla_h(\nu_2\nabla_h\mathbf{U}_h)$ in (5.6) and $\nu_e\nabla_h^2 e$ in (5.9), the Neumann boundary conditions are applied: $(\nabla_h\mathbf{U}_h)\cdot\mathbf{n}=0$ and $(\nabla_h e)\cdot\mathbf{n}=0$, $\mathbf{n}$ being the vector orthogonal to the horizontal boundary.

As in [82], we notice that the results depend weakly on the choice of the free parameters in the equation for the subgrid energy (except for the parameter c_{diss}). As will be shown in the next subsection, the tuning of the stochastic parameterization can be performed without an additional equation for the subgrid energy.

5.2.2 Stochastic parameterization

First we construct the quasi-barotropic (i.e. quasi-two-dimensional) streamfunction, as proposed in [77]:

$$\psi\left(x,y,z,t^n\right)=\varphi\left(x,y,t^n\right)\cdot A\left(x,y,z,t^n\right), \tag{5.11}$$

where $\varphi(x,y,t^n)$ is discrete spatio-temporal white noise with distribution $N(0,1)$, i.e. at each point of the spatial grid and at each time slice, t^n, the realizations of the random variable are independent. A is the amplitude that determines the spatial distribution of the energy influx. The streamfunction ψ modifies equation (5.2) as follows:

$$\frac{\partial\mathbf{U}_h}{\partial t}=\cdots+\alpha\nabla_h^{\perp}S^{n_s}\left(\psi\right), \tag{5.12}$$

where $\nabla_h^{\perp}=(-\partial_y,\partial_x)$. α will be defined later. The operator $S^{n_s}(\cdot)$ denotes n_s applications of the spatial discrete filter:

$$S\left(\psi\right)=\psi+\frac{\left(\Delta x\right)^2}{8}\nabla_h^2\psi. \tag{5.13}$$

This filter is based on the Laplace operator, which is already present in the model and zeroes out the checkerboard mode ($(-1)^{i+j}$; i and j are grid indices along x and y), if the standard second-order approximation is used. The Laplace operator is applied with zero boundary conditions. Unlike [84], we generate a random streamfunction rather than a random Reynolds tensor. The use of a streamfunction gives an analogous spectrum over wavenumbers, but at the same time does not require the removal of the divergence of the resulting forces [137]. The filter $S^n(\cdot)$ defines the correlation radius

of the stochastic tendency. As in the previous chapter, the value $n_s = 6$ is used, which provides a correlation radius equal to several grid steps.

According to [127], the generation of energy by white-in-time noise is proportional to the square of the amplitude, ($\dot{E}_{back} \sim -A^2$), and therefore A is chosen as follows:

$$A\left(x,y,z,t^n\right) = \sqrt{\max\left(\dot{E}_{diss},0\right)}\,. \tag{5.14}$$

Finally, we find the parameter α at each time step from the equality of the total energy fluxes:

$$\frac{\alpha^2\Delta t}{2}\int\left\langle\left|\nabla_h^{\perp}S^{n_s}\left(\psi\right)\right|^2\right\rangle dxdydz = c_{diss}\int\dot{E}_{diss}dxdydz. \tag{5.15}$$

Here Δt is the time step, and the angular brackets $\langle\cdot\rangle$ denote averaging over the ensemble of realizations of the random field φ. The left-hand side of equation (5.15) can be estimated analytically by integrating over the spectrum of wavenumbers [77], but an exact expression for an arbitrary field A depending on the spatial coordinates cannot be obtained. We propose to drop the ensemble averaging:

$$\int\left\langle\left|\nabla_h^{\perp}S^{n_s}\left(\psi\right)\right|^2\right\rangle dxdydz \approx \int\left|\nabla_h^{\perp}S^{n_s}\left(\psi\right)\right|^2 dxdydz, \tag{5.16}$$

where the right-hand side is computed using the current realization of the random field φ. Such a replacement can be made since the standard deviation of the integral is 7% of its ensemble-mean value. The optimal value of c_{diss} equals 1, in contrast to 0.8 for the negative-viscosity parameterization. The increase in the amount of returned energy can be explained by the fact that part of the energy is transferred into inertial waves (as will be shown below), which are dissipated by the numerical filter applied to the free-surface equation [85].

5.3 Results

The model in the Double Gyre configuration reproduces the western boundary current (WBC). At a certain latitude the WBC detaches from the boundary and spreads in the zonal direction, separating the northern and southern gyres. The latitude at which the detachment of the current occurs depends strongly on the spatial resolution and shifts to the south as the mesoscale and submesoscale eddies appear on the computational grid

[135]. The position of the detachment point of the WBC is related to such characteristics as the sea-surface temperature (SST) and the sea-surface height (SSH), since the isolines of these characteristics pass along the jet flow.

Below, we consider 4 models: the eddy-permitting R4, the eddy-resolving R9, and the eddy-permitting model with two KEB parameterizations: R4 negative viscosity and R4 stochastic. All models are spun up as described in Section 5.1.

5.3.1 Eddy kinetic energy

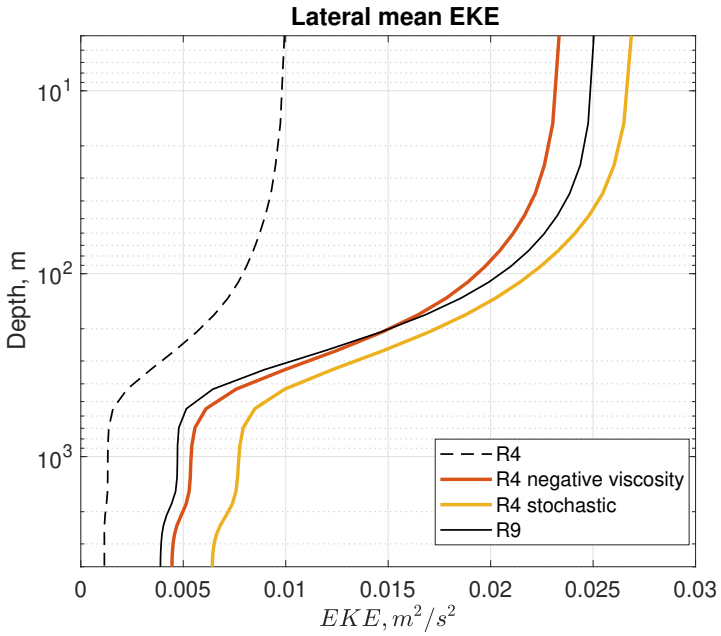

Figure 5.2 — 20-year mean eddy kinetic energy (EKE), averaged horizontally, as a function of depth, $m^2 \cdot s^{-2}$. Comparison of the eddy-permitting (R4, R4+KEBs) and eddy-resolving (R9) models.

Let us evaluate the eddy activity by the level of eddy kinetic energy (Eddy Kinetic Energy, EKE, $\langle \mathbf{u}'^2 \rangle / 2$, where $\mathbf{u}'$ is the deviation from the 20-year mean flow, $\langle \mathbf{u} \rangle$). The application of KEB parameterizations makes it possible to increase the horizontally averaged EKE in the eddy-permitting model approximately to the level of EKE in the eddy-resolving model (R9), see Figure 5.2. Unlike the results obtained in [79], where it was possible to restore the vertical profile over the entire depth, we find an overestimation of the EKE level at depths greater than 200 metres. The spatial distribution of the surface EKE is shown in Figure 5.3 in colour. Both KEB parameterizations lead to

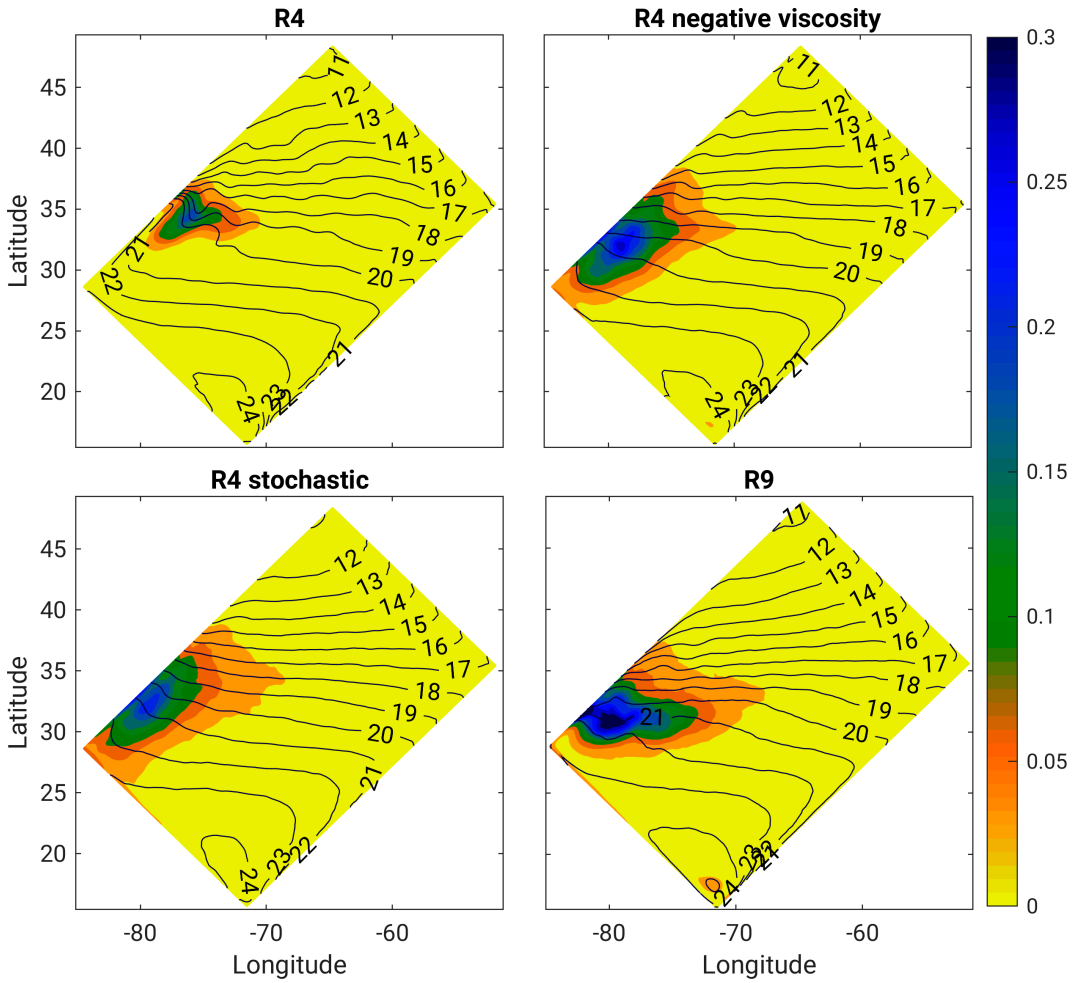

Figure 5.3 — Colour: 20-year mean near-surface kinetic energy, $\mathrm{m}^2 \cdot \mathrm{s}^{-2}$. The colour scale saturates at 0.3. Contours: 20-year mean sea-surface temperature (SST), C^o.

a shift of the region with maximum value of the surface EKE to the south, in agreement with the high-resolution model. However, we note that the surface EKE in the coarse models with KEB parameterizations is elongated along the boundary, in contrast to the elongation in the zonal direction in the R9 model. This means that the propagation of the jet flow in the zonal direction cannot be reproduced by the coarse model even after the application of the KEB parameterizations.

5.3.2 Eddy heat flux

Remark: often by "counter-gradient" heat flux is understood a heat flux *along* the temperature gradient, i.e. from cold to warm [138]. In this section we adopt analogous

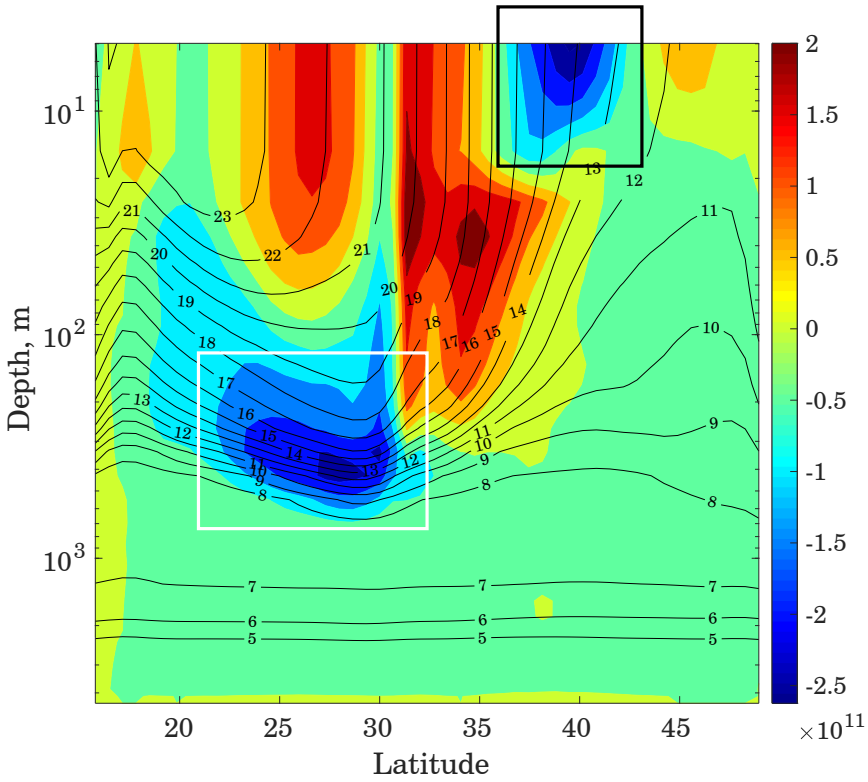

Figure 5.4 — Colour: 20-year mean meridional heat flux, zonally integrated, $\mathrm{W} \cdot \mathrm{m}^{-1}$. Contours: 20-year mean zonally averaged temperature, C^o. The R9 model. The black rectangle highlights a strong counter-gradient heat flux. The white rectangle highlights a strong gradient heat flux directed to the south.

terminology. "Counter-gradient flux" goes from cold to warm, "gradient flux" from warm to cold.

One of the most important characteristics of eddy activity is the explicitly reproduced eddy heat transport. In the case when the eddy heat transport is gradient, the slope of the isotherms decreases, hence the available potential energy of the mean flow decreases, which is the source of the kinetic energy of the mesoscale eddies. As noted in [68], the use of a KEB parameterization can increase the conversion of available potential energy into kinetic.

Let us define the northward meridional heat flux: $Q = \rho_0 C_p T V$, where $C_p \approx 3992\ \mathrm{J} \cdot \mathrm{K}^{-1} \cdot \mathrm{kg}^{-1}$ is the heat capacity and V is the meridional velocity; the dimension of the flux is $[Q] = \mathrm{W} \cdot \mathrm{m}^{-2}$. We note that we neglect the diffusive heat flux, since its magnitude is small when using the biharmonic diffusion operator. The meridional heat flux consists of two parts: the transport by the mean flows (Mean Flow Meridional Heat Transport, MMHT),

$$\rho_0 C_p \langle T \rangle \langle V \rangle, \tag{5.17}$$

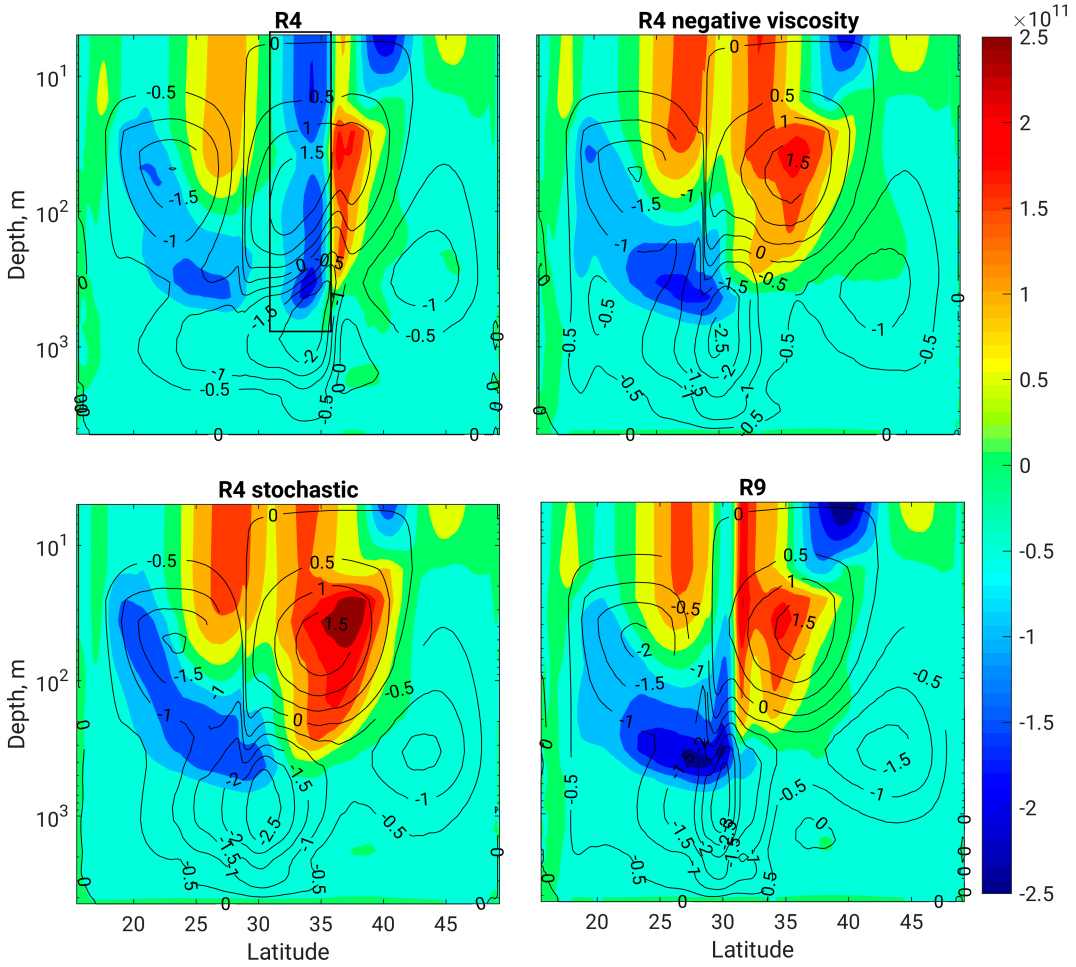

Figure 5.5 — Colour: 20-year mean meridional heat flux, zonally integrated, $\mathrm{W} \cdot \mathrm{m}^{-1}$. Contours: 20-year mean streamfunction of the meridional overturning circulation, Ψ_{MOC}, in Sverdrups. The black rectangle highlights an erroneously predicted southward heat flux in the coarse model.

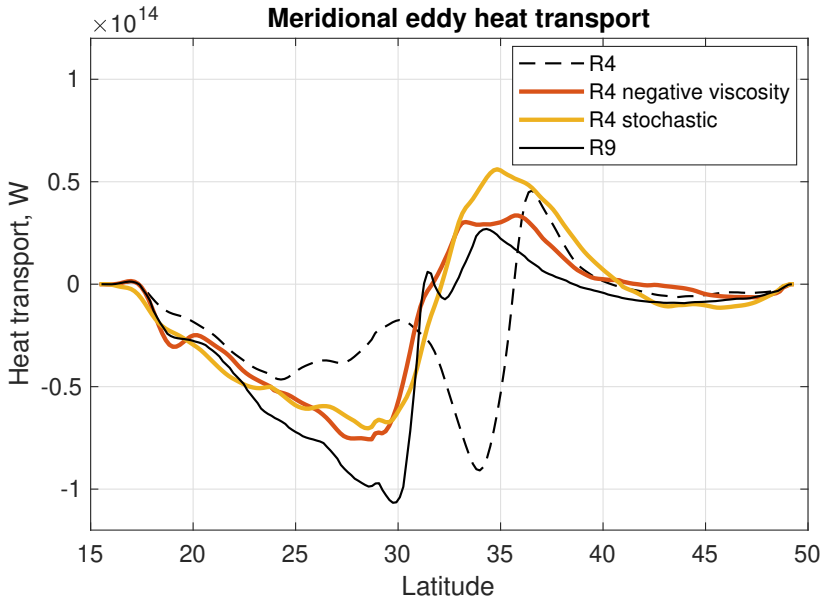

Figure 5.6 — 20-year mean eddy heat flux, zonally and vertically integrated, W.

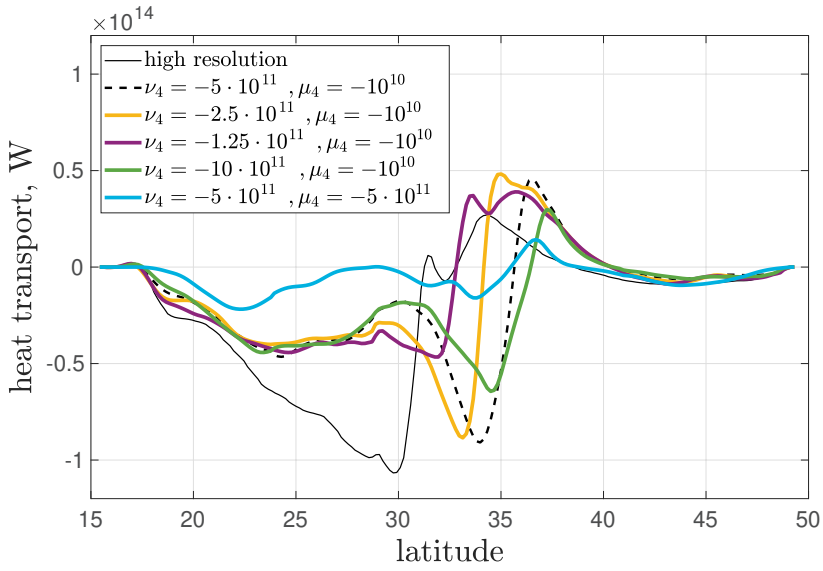

Figure 5.7 — 20-year mean eddy heat flux, zonally and vertically integrated, W. The solid black line is the R9 model, the dashed line is R4. The coloured lines correspond to the R4 model with modified eddy viscosity (ν_4) and diffusion (μ_4) coefficients.

where the angular brackets denote averaging in time over the last 20 years, and the remainder, the eddy heat flux (Eddy Meridional Heat Transport, EMHT),

$$\rho_0 C_p(\langle TV\rangle - \langle T\rangle\langle V\rangle). \tag{5.18}$$

We present only the eddy heat flux, which does not depend on the units of temperature, C^o or K. The EMHT depends significantly on the spatial resolution: it is practically zero in the R1 model, and at high resolutions is comparable with the MMHT, see [135].

Since the northern gyre is colder than the southern one, we expect the eddy heat flux to be directed to the north. As follows from Figure 5.4, which shows the distribution of EMHT over depth for the R9 model, the eddy flux is directed northward (shown in red) predominantly in the near-surface layer of depth 200 metres. An exception is the near-surface region $37^oN - 42^oN$, where a strong counter-gradient flux directed to the south arises, see the black rectangle in Figure 5.4. The most significant EMHT (note the logarithmic depth scale) corresponds to the region $200\text{m} - 500\text{m}$ in depth and $23^oN - 30^oN$ in latitude, which is marked by the white rectangle in Figure 5.4. Heat in this region propagates to the south, in agreement with the northward direction of the temperature gradient at this depth, i.e. the flux is a gradient one. This region defines the sign of the depth-integrated EMHT in the southern gyre, see Figure 5.6. As a result of the application of KEB parameterizations, the southward heat flux in this region increases in the coarse R4 model, see Figure 5.5, and the sign of the erroneously predicted flux in the region $32^oN - 35^oN$ changes, as it should be in the high-resolution

model, see the black rectangle. Both KEB parameterizations make it possible to shift to the south the position of the minimum of the vertically integrated eddy heat flux, although its absolute value turns out to be underestimated, see Figure 5.6. Also, the models with KEB parameterizations overestimate the flux north of the 30th latitude, see Figure 5.6. The described effect of shifting the extremal value of the flux to the south cannot be achieved by changing the viscosity (ν_4) or diffusion (μ_4) coefficients, see Figure 5.7.

5.3.3 Mean fields

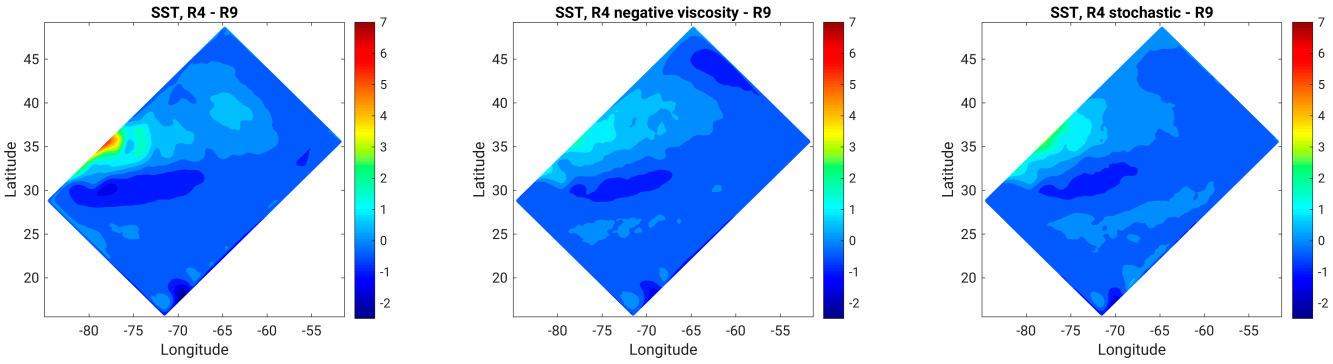

Figure 5.8 — 20-year mean difference in sea-surface temperature between eddy-permitting (R4, R4+KEBs) and eddy-resolving R9 models, C^o.

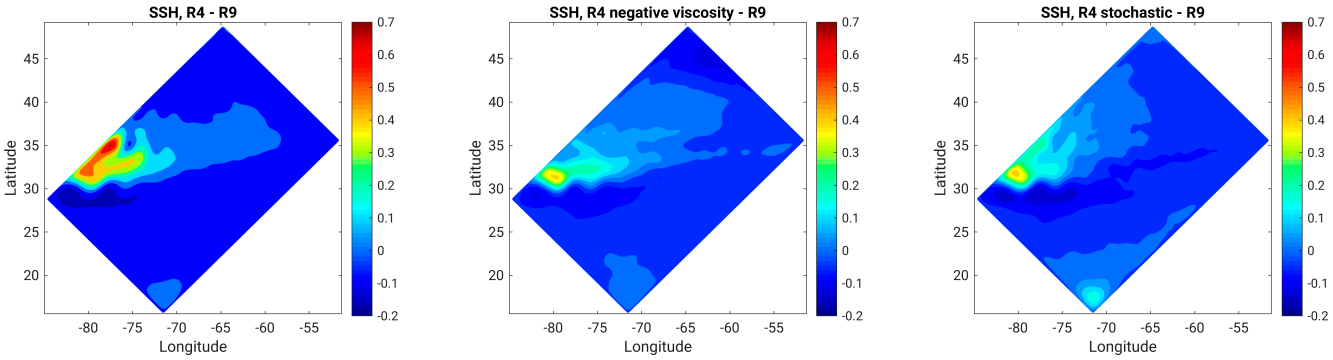

Figure 5.9 — 20-year mean difference in sea-surface height between eddy-permitting (R4, R4+KEBs) and eddy-resolving R9 models, m.

The meridional overturning circulation (MOC) is shown by contours in Figure 5.5. The MOC is defined by the following streamfunction: $\Psi_{MOC}(y',\ z) = \int_{-H}^{-z} \langle V(x',y',z',t)\rangle dx'dz'$, where x' and y' are the coordinates along longitude and latitude respectively, $z \in (-H,0)$ is the depth, V is the meridional velocity, and the angular

Table 6 — Norms of errors in the 20-year mean sea-surface temperature, sea-surface height and surface salinity (SST, SSH, SSS) between the coarse models (R4, R4 + KEBs) and the high-resolution model (R9). The following two norms for an arbitrary field $\varphi(x,y)$ are separated by a semicolon: $\max(|\varphi_{R4} - \varphi_{R9}|)$; $\text{mean}(|\varphi_{R4} - \varphi_{R9}|)$.

	R4	R4 negative viscosity	R4 stochastic
SST, C^o	7.0; 0.4	3.1; 0.3	4.3; 0.27
SSH, m	0.68; 0.062	0.38; 0.039	0.40; 0.040
SSS, psu	0.54; 0.108	0.33; 0.098	0.52; 0.070

brackets denote averaging over the last 20 years. The circulation in all the models consists of 4 cells, with the largest cell located near the bottom (taking into account the logarithmic depth scale). The near-bottom cell is shifted to the north in the R4 model compared with the R9 model. Both KEB parameterizations restore the correct position of this cell: near the 30th latitude. The northern near-surface cell acquires the correct shape as a result of the application of the KEB parameterizations. The northern near-bottom cell is better reproduced in the model with the stochastic KEB parameterization, compared with the model with the negative-viscosity parameterization: note the isoline -1.5 in Figure 5.5.

The restoration of the eddy activity and of the mean circulation has a positive effect on the mean near-surface fields. In Figure 5.3 the sea-surface temperature for the four models is shown by contours. The main difference between the R4 and R9 models is observed in the wall-bounded region, approximately at latitude $35^o N$. In this region the isolines of temperature in the R4 model (see the isotherms 21 and 22 in Figure 5.3) pass along the boundary of the domain, creating a large temperature gradient in the direction perpendicular to the boundary. The KEB parameterizations smooth out this gradient, which leads to a significant reduction of the errors in SST, see Table 6. The spatial distribution of errors in SST and SSH is shown in Figures 5.8 and 5.9 respectively. A significant decrease of the errors for both parameterizations is observed near the detachment point of the jet flow. We note that the negative-viscosity parameterization introduces additional errors in the northern part of the domain.

5.3.4 Temporal variability

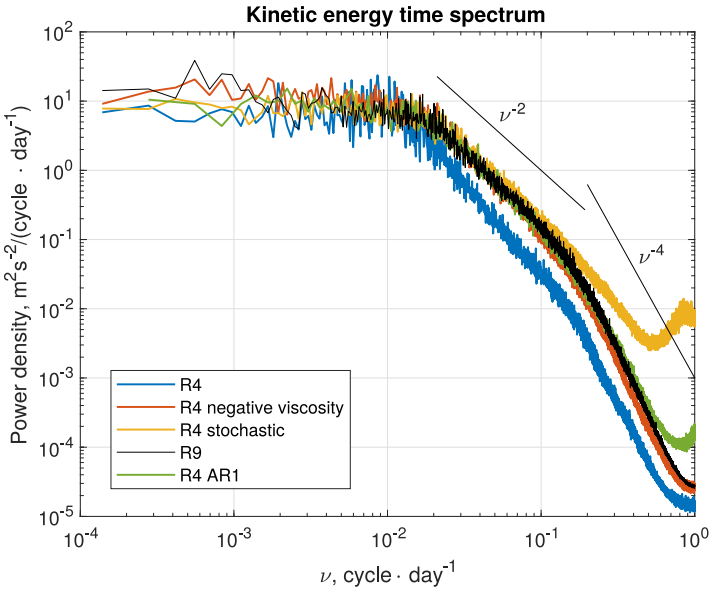

Figure 5.10 — Distribution of the surface EKE over the spectrum of time scales. The spectrum is averaged over the region bounded by the white rectangle shown in Figure 5.1. The additional line "R4 AR1" corresponds to a temporally correlated stochastic parameterization.

We study the temporal variability by considering the distribution of the surface EKE over the spectrum of time scales, see Figure 5.10. The spectral density is averaged over the region bounded by the white rectangle in Figure 5.1, in order to exclude the strong dependence on the detachment latitude of the jet flow. The high-frequency variability (up to 100 days) is characterized by two spectral-density intervals obeying power-law dependences (ν^{-4}, ν^{-2}). We do not provide a physical explanation of the observed intervals, but assume that the change of the slope at the 5-day scale is explained by the fact that the mesoscale dynamics is absent on shorter time scales. The energy density in both power-law intervals is underestimated in the R4 model. The KEB parameterizations make it possible to increase the spectral density on the interval ν^{-2} up to the level corresponding to the R9 model. The negative-viscosity parameterization also restores the spectral density on the interval ν^{-4}. For the stochastic parameterization a spurious maximum is observed in the energy spectrum at the scale of 1 day, presumably associated with the excitation of inertial oscillations, which have a close period. It has not been reported previously that a stochastic KEB parameterization with white-in-time noise can excite inertial oscillations, possibly because in most works quasi-geostrophic

equations are considered (as, for example, in [68] and [84]), which exclude the presence of inertial oscillations. The use of a temporally correlated stochastic parameterization makes it possible to avoid the excitation of inertial waves, see Figure 5.10, the line "R4 AR1". The parameterization is described in Appendix D; the parameters are: $c_{diss} = 0.8$, $n_s = 6$.

Finally, let us consider the instantaneous fields of relative vorticity, see Figure 5.1. The solutions of the R4 and R9 models differ significantly in the number of eddies. Both KEB parameterizations strengthen the eddy activity, but in different ways. The stochastic parameterization generates "synthetic" turbulence, which in its form is similar to the stochastic tendency itself, while the negative-viscosity parameterization strengthens the already existing eddy field.

5.4 Conclusions

In this chapter it is shown that KEB parameterizations compensating the dissipation associated with the biharmonic viscosity can restore the level of eddy activity in an eddy-permitting ocean model based on the primitive equations. In particular, the eddy kinetic energy is increased and the eddy heat flux is restored. Improvements are also observed in the mean fields: the meridional overturning circulation, the sea-surface elevation and the sea-surface temperature. The propagation of the wall-bounded jet flow in the zonal direction cannot be reproduced by means of KEB parameterizations. The stochastic KEB parameterization with white-in-time noise can excite inertial oscillations. To prevent this effect, a temporally correlated stochastic tendency, constructed by means of an autoregressive model, can be used.

Although the studied parameterizations differ in the form of the tendency (stochastic or deterministic) and in the presence of an equation for the subgrid kinetic energy, their effect on the mean characteristics of quasi-two-dimensional turbulence can be considered to be close. An analogous result was given in Chapter 3. In this connection, we come to the conclusion that the key characteristic of a KEB parameterization is how it redistributes the kinetic energy into large scales. For this process one can distinguish two key parameters: the scale of the energy return and the amount of returned energy, the study of which is the subject of the next chapter of the dissertation.

Chapter 6. Spectral characteristics of the subgrid forces and of the subgrid parameterizations in the NEMO model

In the previous chapter the parameters of the KEB parameterizations were chosen so as to achieve the best agreement between the eddy-permitting and eddy-resolving ocean models. In order to use such parameterizations in more realistic configurations and at various resolutions, it is necessary to tune the free parameters of the parameterizations, among which the most significant are the following: the *scale of the energy return* and the *amount of returned energy*. The scale of the energy return can be defined as follows:

$$\overline{k^2} = \frac{\int k^2 B(k) dk}{\int B(k) dk}, \tag{6.1}$$

where

$$B(k) = \frac{d}{dk} \int_{|\mathbf{k}|^2 \leqslant k^2} Re\langle \mathbf{u}_\mathbf{k}^* \mathbf{f}_\mathbf{k} \rangle d\mathbf{k}, \tag{6.2}$$

is the density of the energy influx from the KEB tendency at the scale with modulus of the wavenumber k, and $\mathbf{u}_\mathbf{k}$, $\mathbf{f}_\mathbf{k}$ are the Fourier transforms of the velocity and of the KEB tendency, respectively, $*$ is the complex conjugate, $\langle \cdot \rangle$ is averaging over the ensemble or in time. For the stochastic parameterization with white-in-time noise, formula (6.2) should be replaced by the following one: $B(k) = \frac{\Delta t}{2} \frac{d}{dk} \int_{|\mathbf{k}|^2 \leqslant k^2} \langle |\mathbf{f}_\mathbf{k}|^2 \rangle d\mathbf{k}$.

Many ways of tuning the scale of the stochastic parameterization are known:

1. Parameterizations based on the prediction of the EDQNM theory, [70]. In such parameterizations either a random vector potential is constructed [72], or a random Reynolds tensor [67], with white grid noise in space. In that case the stochastic tendency has the Fourier transform $\mathbf{f}_\mathbf{k} \sim k$, and $B(k) \sim k^4$ in three-dimensional turbulence [67], $B(k) \sim k^3$ in two-dimensional [84].
2. In [137] it was proposed, for simplicity of implementation, to use white grid noise in velocity as the stochastic tendency, $\mathbf{f}_\mathbf{k} \sim 1$, which gives in three-dimensional turbulence $B(k) \sim k^2$, and in two-dimensional $B(k) \sim k$.
3. In [68] white grid noise in vorticity was used, which gives $\mathbf{f}_\mathbf{k} \sim k^{-1}$ and $B(k) \sim k^{-1}$ in two-dimensional turbulence.
4. In the ECMWF ensemble weather-prediction model a random streamfunction with Fourier coefficients $\sim k^{-1.27}$ is used, which gives $B(k) \sim k^{0.46}$ [77]. As will be shown below, the spectral slope $k^{0.46}$ corresponds to the spectral density of the subgrid forces.

5. In the coarse-resolution atmospheric model PUMA [139] a random vorticity with Fourier coefficients $\sim k^{-1.27}$ is used, which gives $B(k) \sim k^{-3.54}$.
6. Also widespread is spatial filtering of white noise in space, which corresponds to considering a non-spectral filter for separation of scales in the EDQNM theory [70]; however, unlike in the present work, the spatial filter is usually applied once or twice [72], [84].
7. In Section 3.2 of Chapter 3 of the dissertation it was proposed to tune $B(k)$ so as to reproduce the spectrum of energy generation by the subgrid forces, which is located on the inertial interval of the inverse energy cascade.

Most of the above ways of constructing the stochastic tendency lead either to the generation of energy near the grid scale (items 1, 2, 4, 6), or at the largest scales (items 3, 5). The scale of the parameterization tuned according to item 7 does not depend on the resolution of the coarse model and always corresponds to the inertial interval of the inverse energy cascade.

For the deterministic KEB parameterization the tuning of the scale of the energy return is also possible:

– In [42; 140] various tendencies in vorticity were investigated: $\Delta^n\xi$, $n = -1,0,1,2$; $\widehat{\xi}$, $\xi - \widehat{\xi}$, where $\widehat{(\cdot)}$ is a spatial filter. For non-spectral schemes, the best results in forecast errors and in the decay of energy and enstrophy were found for the parameterization $\xi - \widehat{\xi}$, which in scale coincides with the Laplace operator.
– In [79] spatial smoothing of the tendency of the negative-viscosity parameterization is applied.

Note that, unlike most of the stochastic KEB models mentioned above, the negative-viscosity parameterization predominantly returns energy not at the edges of the range of reproducible scales, but in its middle – on the interval of kinetic-energy generation (the internal Rossby radius of deformation). If one assumes the existence of a bidirectional energy–enstrophy cascade,

$$E(k) = \begin{cases} C_1\varepsilon^{2/3}k^{-5/3}, k < k_f, & \text{(6.3а)} \\ C_2\eta^{2/3}k^{-3}, \quad k > k_f, & \text{(6.3б)} \end{cases}$$

then the spectrum of energy generation by the negative-viscosity operator will have the form:

$$B(k) \sim k^2E(k) = \begin{cases} C_1\varepsilon^{2/3}k^{1/3}, k < k_f, & \text{(6.4а)} \\ C_2\eta^{2/3}k^{-1}, \quad k > k_f, & \text{(6.4б)} \end{cases}$$

which has a maximum on the scale of energy generation k_f.

The amount of returned energy in two-dimensional turbulence is usually chosen proportional to the viscous dissipation, i.e.

$$\dot{E}_{back} = c_{diss}\dot{E}_{diss}, \tag{6.5}$$

where the proportionality coefficient $0 \leqslant c_{diss} \leqslant 1$ can be chosen either globally for the whole domain (as done in the previous chapter and in [68]), or depend on the local Rossby number ($Ro = \dfrac{|\xi|}{f}$, ξ is the relative vorticity, f is the local Coriolis parameter) [79; 81; 141]:

$$c_{diss} = \left(1 + \frac{Ro}{Ro_{diss}}\right)^{-1}, \tag{6.6}$$

or be greater than unity if the dissipation of available potential energy is included in the subgrid kinetic-energy budget [142]. The exact value of c_{diss} cannot be found from a priori analysis of the subgrid forces, because, firstly, the stability of the computation depends on its choice, and secondly, the energy flux can be separated into forward and backward in three different ways: in Fourier space, in physical space, and according to the energetic contributions of the eddy-viscosity and KEB parameterizations. In each case the coefficient c_{diss} will be different. Nevertheless, if c_{diss} is defined in some way, one can measure how it depends on resolution and on local characteristics of the turbulence (the Rossby number).

As follows from the above overview, there are many ways of tuning the scale and the amount of returned energy. In this chapter, by means of the analysis of the solutions of the NEMO model in the Double Gyre configuration at high resolution $1/24^o$, an analysis of the interaction between resolved and unresolved scales in coarse models is carried out (a priori analysis of the subgrid forces). An attempt is made to relate the characteristics of the KEB parameterizations with the characteristics of the inverse kinetic-energy cascade partially resolved on the grid. In particular, the question of the possibility of applying the parameterizations in eddy-resolving models, in which the forward kinetic-energy cascade is partially resolved at submesoscales ($1 - 100$ km), is considered. On the basis of the analysis, recommendations are given for tuning the KEB parameterizations and preliminary computations at eddy-resolving resolution are carried out.

6.1 Spectral characteristics of the R24 model

Table 7 — Parameters of the eddy-resolving models. The parameterizations of turbulent diffusion and viscosity act in the horizontal direction.

	R9	R12	R24
$n_x \times n_y \times n_z$	$270 \times 180 \times 30$	$360 \times 240 \times 30$	$720 \times 480 \times 30$
grid step	$1/9^o$, 11.7 km	$1/12^o$, 8.8 km	$1/24^o$, 4.4 km
time step	800 sec	600 sec	300 sec
diffusion	∇_h^4, -10^9 m^4/s	∇_h^4, -10^9 m^4/s	∇_h^4, -10^9 m^4/s
viscosity	∇_h^4, $-5 \cdot 10^{10}$ m^4/s	∇_h^4, $-1.25 \cdot 10^{10}$ m^4/s	∇_h^4, $-5 \cdot 10^9$ m^4/s

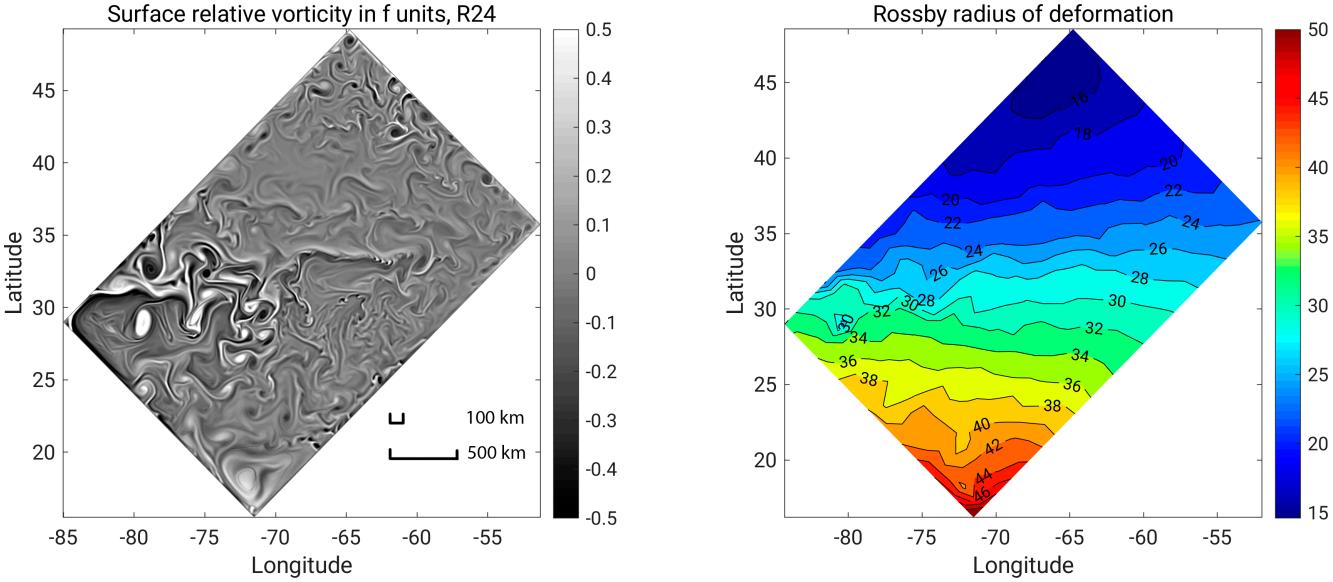

Figure 6.1 — Left: relative vorticity at the surface in units of the Coriolis parameter for the R24 model, March 30. The colour scale is limited by the values ± 0.5. In reality the range of values is $(-0.9; 3.7)$. Right: the internal Rossby radius of deformation in kilometres, from data of January 1.

The NEMO model configuration described in Section 5.1 was used. The parameters of the eddy-resolving models are given in Table 7. The computations with the eddy-resolving models were carried out for 20 years starting from the statistically equilibrium state of the R9 model. For the analysis of the nonlinear interactions, one last year of the computation with the R24 model was used.

Let us roughly estimate the spectral interval on which the inverse energy cascade should occur. We assume that the baroclinic instability is the source of kinetic energy.

Let us compute the internal Rossby radius of deformation, $L_R = \frac{c_{int}}{f}$ [143], where $c_{int} = \pi^{-1}\int_{-H}^{0} N(z)dz$ is the phase velocity of internal gravity waves, $N(z)$ is the Brunt–Väisälä frequency, f is the Coriolis parameter. c_{int} varies in the range 2 m/s in the south and 1.6 m/s in the north, and the Coriolis parameter f: $3.9{\cdot}10^{-5}$ s^{-1} in the south and $1.1\cdot10^{-4}$ s^{-1} in the north. As a result, the deformation radius L_R varies in the range from 50 km in the south to 15 km in the north, see Fig. 6.1(b). The deformation radius determines the minimum wavelength of baroclinic instability, $L_{bc} = 2\pi L_R$, [144]. We obtain that baroclinic instability in the south should occur at wavelengths $L_{bc} \approx 300$ km, and in the north $L_{bc} \approx 100$ km. These wavelengths are well resolved by all the models given in Table 7.

Since we observe strongly anisotropic flows, we assume that the blockage of the cascade occurs at the Rhines scale. The root-mean-square horizontal velocity averaged over the domain and over the year in the R24 model is $U_{rms} = 0.13$ m/s, and the differential rotation $\beta = 1.8\cdot10^{-11}$ 1/(m s). Then the cascade-blockage wavenumber [10], $k_{rh} = \sqrt{\frac{\beta}{U_{rms}}} \approx 0.012$ km^{-1}, which corresponds to the scale $L_{rh} = \frac{2\pi}{k_{rh}} \approx 500$ km. Thus, we expect that the conversion of available potential energy into kinetic will occur in the wavelength range $100-300$ km, after which the energy will be redistributed to large scales, of the order of 500 km, until the blockage of the cascade by Rossby waves occurs. These scales are shown on Figure 6.1(a) for comparison with the eddy sizes.

For the computation of the spatial spectra, discrete sine–cosine Fourier transforms are used. The type of transform is chosen depending on the boundary conditions for the horizontal velocity. Let $\mathbf{U}$ be the full three-dimensional velocity, $\mathbf{U}_h$ the horizontal component of the velocity, and $\widehat{(\cdot)}$ the Fourier transform. Then the depth-averaged *spectral density of kinetic energy* associated with the horizontal velocity is:

$$E_U(k) = H^{-1}\int_{-H}^{0}\frac{d}{dk}\int_{|\mathbf{k}|^2\leqslant k^2}\frac{|\widehat{\mathbf{U}_h}|^2}{2}d\mathbf{k}dz, \tag{6.7}$$

$\mathbf{k} = (k_x,k_y)$. The Fourier-transform normalization is as follows:

$$\int E_U(k)dk = (L_xL_yH)^{-1}\int\frac{|\mathbf{U}_h|^2}{2}dxdydz. \tag{6.8}$$

The *spectral influx of kinetic energy* from the advection forces is computed as follows:

$$T_N(k) = -H^{-1}\int_{-H}^{0}\frac{d}{dk}\int_{|\mathbf{k}|^2\leqslant k^2} Re\left(\widehat{\mathbf{U}_h}^{*}\widehat{(\mathbf{U}\cdot\nabla)\mathbf{U}_h}\right)d\mathbf{k}dz. \tag{6.9}$$

Since the advection operator conserves energy, the spectral energy influx satisfies the equality $\int T_N(k)dk = 0$, and the *spectral flux of kinetic energy* from scales $k' \leqslant k$ to scales $k' > k$ is defined by the formula:

$$\Pi_N(k) = \int_{k'>k} T_N(k')dk'. \tag{6.10}$$

Positive values of the flux correspond to a forward energy cascade through the wavenumber k to small scales (high wavenumbers), and negative values to an inverse cascade. Let us also introduce the *spectral flux of relative enstrophy*:

$$\int_{k'>k} T_N(k')k'^2dk'. \tag{6.11}$$

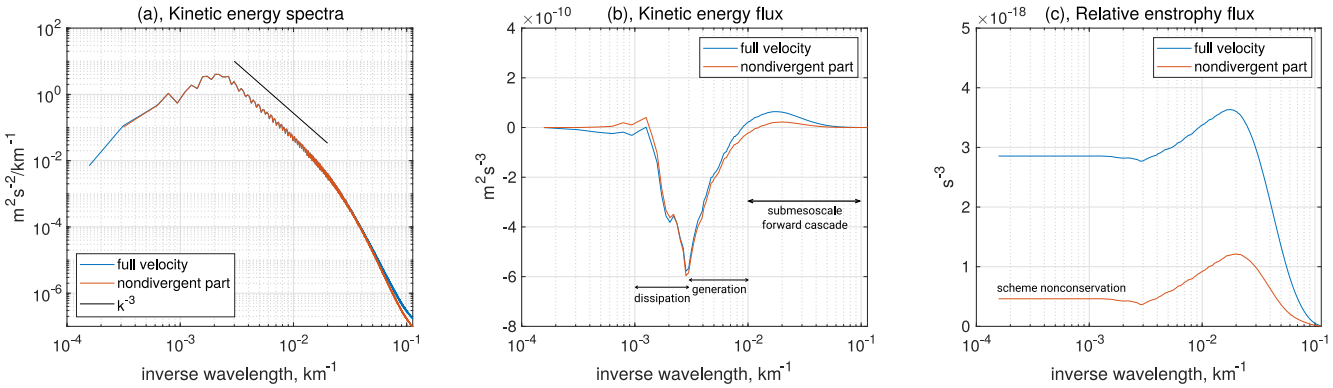

Figure 6.2 — (a), spectral density of kinetic energy (6.7). (b), spectral flux of kinetic energy (6.10). (c), spectral flux of enstrophy (6.11). The blue curve corresponds to the full velocity, and the red one to the non-divergent part. The R24 model, averaging over depth and over the year, the Fourier transform corresponds to the whole domain.

Figure 6.2 shows the spectral characteristics of the R24 model. According to the character of the nonlinear interactions, three spectral intervals can be distinguished. On the wavelengths $100 - 300$ km the generation of kinetic energy occurs. Most of this energy is redistributed to large scales, forming the inverse energy cascade, which is blocked at the scales $300 - 1000$ km, see Fig. 6.2(b). As in [145], [146], the maximum of the spectral density of kinetic energy approximately corresponds to the scale at which the maximum energy flux is observed. In the generation interval a spectral density of kinetic energy with the slope k^{-3} is observed, see Fig. 6.2(a). Although the theory of geostrophic turbulence predicts the slope $k^{-5/3}$ on the interval of the inverse energy cascade [10], in practice the slope k^{-3} is usually observed [68], [144], [146], [147], [148]. Apparently this is associated with the fact that the intervals of generation and dissipation of energy are not separated in Fourier space, as a result of which essentially

no inertial interval of the inverse energy cascade exists; however, the redistribution of energy to large scales is preserved. On the other hand, the slope k^{-3} can be explained by the fact that in the range of scales $100-300$ km, along with the inverse energy cascade, a forward enstrophy cascade is observed, see Fig. 6.2(c), the red line.

In the submesoscale range $10-100$ km the generation of kinetic energy is practically absent and a forward energy cascade into small scales is observed, see Fig. 6.2(b). The forward energy cascade must necessarily exist, since it is related to the forward enstrophy cascade. Nevertheless, many works are devoted to the properties of this cascade [149], [15]. In particular, it is assumed that in the submesoscale range the flows become geostrophically unbalanced, and as a result of the interaction of the geostrophic and ageostrophic components of the flow, a forward energy cascade represented by inertia–gravity waves is formed. The existence of such a cascade has been shown both in the Boussinesq equations and in the primitive equations [149]. The simplest way to estimate the contribution of ageostrophic flows to the formation of the forward energy cascade is to consider the contribution from non-divergent flows. From Figure 6.2(a) it is seen that the divergent component of velocity modifies the spectral energy density at the smallest scales (a few tens of kilometres); nevertheless, taking into account the divergent component of velocity (and the vertical velocity) leads to an increase of the forward-cascade energy flux by a factor of 2.9 ("full velocity" compared with "nondivergent part" in Figure 6.2(b)). A characteristic feature of the forward energy cascade is also the generation of enstrophy by ageostrophic flows, see Figure 6.2(c), the blue line. A more accurate analysis of ageostrophic flows can be performed taking into account the dispersion relation of inertia–gravity waves [149].

6.2 Characteristics of the subgrid forces

Below we shall need the definition of subgrid forces. Let us introduce the projection operator, $\mathcal{P}$, from the grid of the R24 model onto a coarser grid, which is applied in two stages. First, in the neighbourhood of a point of the coarse grid the horizontal averaging over the nearest points of the R24 model with equal weights is performed. After that smoothing with the filter $[1\ 2\ 1]/4$ in each horizontal direction is performed. Then the velocity resolved on the coarse grid is:

$$\mathcal{P}(\mathbf{U}), \tag{6.12}$$

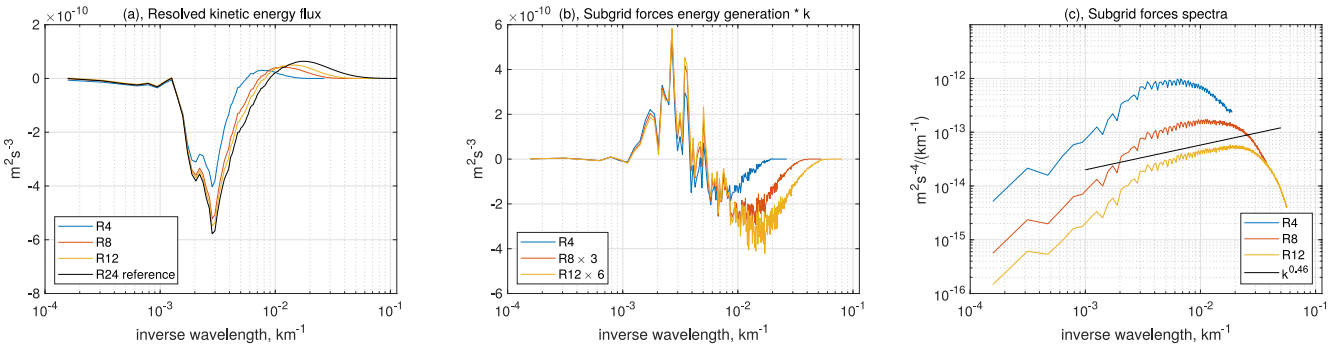

Figure 6.3 — (a), spectral flux of energy resolved on the coarse grid. (b), spectral density of the energy influx for the subgrid forces. The influxes at resolutions R8 and R12 are multiplied by 3 and 6 respectively, in order to match the graphs at large scales. The influx is multiplied by the wavenumber, which makes it possible to estimate the area under the curve in logarithmic coordinates. (c), spectral density of the subgrid forces.

the tendency of the resolved advection on the coarse grid is:

$$N = -(\mathcal{P}(\mathbf{U}) \cdot \nabla)\mathcal{P}(\mathbf{U}_h), \tag{6.13}$$

and the tendency of the unresolved advection on the coarse grid, i.e. the *subgrid forces*:

$$S = -\mathcal{P}((\mathbf{U} \cdot \nabla)\mathbf{U}_h) + (\mathcal{P}(\mathbf{U}) \cdot \nabla)\mathcal{P}(\mathbf{U}_h). \tag{6.14}$$

For the computation of the advection operator on the coarse grid, a scheme in flux form is used, which is one of the schemes implemented in the NEMO model. We consider coarsening of the resolution to 1^o (R1), $1/4^o$ (R4), $1/8^o$ (R8), $1/12^o$ (R12).

The spectral characteristics (6.9), (6.10) can be computed for the resolved advection N and for the subgrid forces S. Figure 6.3 shows: (a), the resolved flux of kinetic energy, $\Pi_N(k)$; (b), the influx of kinetic energy from the subgrid forces, $T_S(k)$. When the resolution is coarsened, the resolved flux of kinetic energy through the inverse cascade decreases, Fig. 6.3(a). For the resolution R4 by approximately 30%, and for the resolution R1 it is practically absent (not shown in the figure). For the eddy-resolving R8 and R12 models the energy flux decreases insignificantly; nevertheless, this is the result of a priori analysis, and in real computations the inverse-cascade energy flux can depend strongly on resolution [144]. The insufficient spectral energy flux at coarse resolution is compensated by the subgrid forces, which redistribute the kinetic energy from scales smaller than 250 km to scales larger than 250 km, see Fig. 6.3(b). An analogous result was already given for homogeneous two-dimensional turbulence (see Chapter 3, Figure 3.1). The spectrum of energy generation by the subgrid forces should be used

for tuning the long-wave KEB parameterization. Let us highlight the main properties of the generation spectrum:

- The generation scale (larger than 250 km) does not depend on the resolution of the coarse model and approximately corresponds to the scales of blockage of the inverse energy cascade.
- The strength of the long-wave pumping decreases as the resolution of the coarse model is increased: by a factor of 3 and 6 as the resolution is increased by a factor of 2 and 3 respectively. Note that in Figure 6.3 the influxes for the R8 and R12 models are multiplied by 3 and 6 respectively.
- The ratio of returned energy ($T_S(k) > 0$) to dissipated ($T_S(k) < 0$) decreases as the resolution is increased. If we estimate the proportionality coefficient in formula (6.5) as

$$c_{diss} = \frac{\int \max(T_S(k),0)dk}{\int \max(-T_S(k),0)dk}, \tag{6.15}$$

  we obtain the following values of c_{diss}: 6.2, 1.44, 0.84, 0.6 for resolutions R1, R4, R8 and R12 respectively. The values $c_{diss} > 1$ for the R1 and R4 models mean that at the "subgrid" scale eddies are generated, which then grow up to resolved scales. Such situations were proposed to be taken into account in [142] by including the contribution of the Gent–McWilliams parameterization into the subgrid energy budget. The values $c_{diss} < 1$ for resolutions R8 and R12 mean that in these models the forward energy cascade in submesoscales starts to be resolved, and the assumption of geostrophic turbulence about the redistribution of energy to large scales is violated.

The spectral density of the subgrid forces S, computed analogously to (6.7), is shown in Figure 6.3(c). The slope of the spectral density corresponds to the one used in [77], and is equal to $k^{0.46}$. The maximum of the spectral density depends on resolution and is reached at wavelengths of approximately 5 grid steps. This scale can be used for tuning the short-wave KEB parameterization (the definition of the short-wave and long-wave KEB parameterizations is given in the introduction to Chapter 3).

Figure 6.4 shows the dependence of c_{diss} on the local Rossby number in comparison with formula 6.6. The distribution is constructed from the values of the local energy influx from the subgrid forces in Galilean-invariant form:

$$\frac{dE}{dt} = \frac{\partial \mathcal{P}(u_i)}{\partial x_j}(\mathcal{P}(u_i u_j) - \mathcal{P}(u_i)\mathcal{P}(u_j)), \tag{6.16}$$

then

$$c_{diss}(Ro) = \frac{\langle \max(\frac{dE}{dt},0)\rangle}{\langle \max(-\frac{dE}{dt},0)\rangle}\Big|_{Ro}. \tag{6.17}$$

The averaging $\langle\cdot\rangle$ is taken in time and over all computational points. In accordance with formula (6.6), the amount of returned energy decreases with the increase of the local Rossby number, with a characteristic scale of $Ro_{diss} \approx 1$. Exactly this value was used in [79]. Since high-resolution models are characterized by larger values of vorticity, the formula can be used for the automatic reduction of the strength of the KEB parameterization and thus takes into account the partially resolved forward energy cascade in submesoscales, whose magnitude should be determined by the imbalance of the flow (i.e. by the local Rossby number). Nevertheless, this formula has been tested predominantly in eddy-permitting models, and at such resolution the greatest sensitivity to the choice of the coefficient Ro_{diss} is observed in the presence of strong wall-bounded flows [79; 81]. The strength of the parameterization near the boundaries can also be reduced by simpler means: by using zero Dirichlet boundary conditions for the subgrid energy, or by zeroing c_{diss} near the boundaries. For the eddy-permitting R4 model this makes it possible to increase the stability of the computation and to use $c_{diss} = 1$ far from the boundaries (the results are not given).

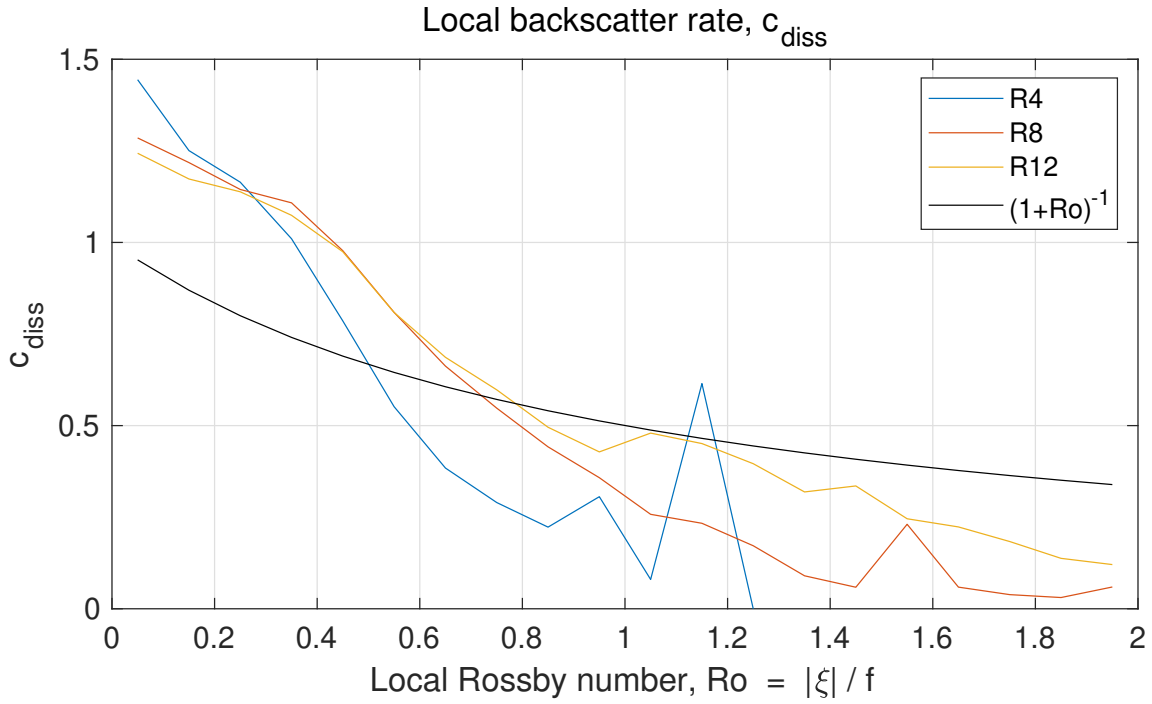

Figure 6.4 — Verification of the formula $c_{diss} = (1 + Ro/Ro_{diss})^{-1}$ for the estimation of the local amount of returned energy.

6.3 Spectral analysis of the subgrid parameterizations

In the previous chapter, the KEB parameterizations were described: the stochastic one (Section 5.2.2, "stoch" in the graphs) and the negative-viscosity one (Section 5.2.1, "negvisc" in the graphs). Also considered are the subgrid forces ("subgrid" in the graphs), the biharmonic viscosity ("blp" in the graphs) and the scale-similarity model ("SS" in the graphs, described in Section 4.3.3). The parameters of the KEB parameterizations at resolution R4 in the previous chapter were chosen so as to achieve the best agreement with the R9 model, mainly in the reproduction of the meridional eddy heat flux. We propose to find out how the spectral characteristics of the subgrid forces and of the subgrid parameterizations relate to each other, and to associate the scales of energy return with the scales of the inverse energy cascade.

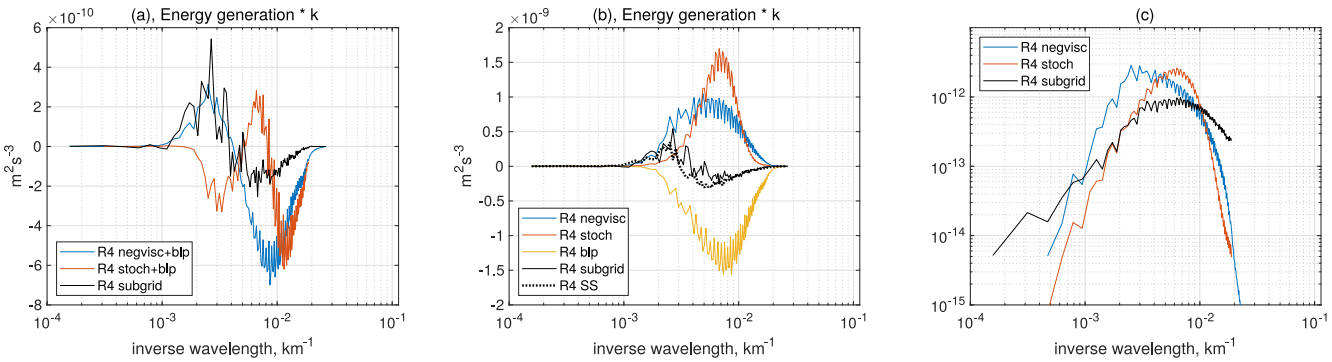

Figure 6.5 — Comparison of the energy influx from the subgrid forces ("R4 subgrid") and from the models of subgrid turbulence at resolution R4: (a), KEB parameterization + biharmonic viscosity; (b), the subgrid parameterizations separately. (c), comparison of the energy influxes from the KEB parameterizations and the spectral density of the subgrid forces.

Figure 6.5(b) shows the spectral influxes of kinetic energy for the KEB parameterizations (blue and red lines). For both KEB parameterizations, the larger part of the energy influx is observed on the scales of baroclinic instability, i.e. $100 - 300$ km. If we add to the negative-viscosity parameterization the dissipation associated with the biharmonic operator, the characteristic scales of energy generation shift to the long-wave region and approximately coincide with the spectrum of generation by the subgrid forces, see Figure 6.5(a), the blue line. The analogous characteristic for the stochastic model, the red line, can be corrected if a larger number of filterings is applied to the stochastic tendency. However, the direct excitation of the scales $300 - 1000$ km by the stochastic

parameterization may be undesirable, since in this region the nonlinear interactions are weakened and the flows are anisotropic. As a result, there is a possibility of destruction of large-scale coherent structures, such as jet flows, by the stochastic parameterization.

For the scale-similarity model two spectral intervals of energy generation and dissipation are observed, analogous to the subgrid forces, see Fig. 6.5(b), shown by dots. However, in order to construct a KEB parameterization on the basis of this model analogously to what is done in Section 3.2.3 of Chapter 3, it is necessary to filter the tendency down to scales of 300 km, which would require too large a number of applications of the spatial filters. For this reason we do not give the results for the SS parameterization in the NEMO ocean model.

From Figure 6.5(c) it is seen that the spectrum of energy generation by the stochastic parameterization (red line) and the spectral density of the subgrid forces (black line) have approximately the same horizontal scale (the graphs are aligned along the y-axis). This may mean that at coarse resolution it is impossible to distinguish between the long-wave and short-wave KEB parameterizations. Exactly this situation was investigated in [84], where by means of a short-wave KEB parameterization the inverse energy cascade was restored. A distinction will already be observed at eddy-resolving resolution, as shown below.

The scale of the energy return, defined as the mean squared wavenumber (6.1), coincides up to 10% for both parameterizations tuned in the previous chapter. Bearing in mind that the scale of the energy return by the negative-viscosity model is determined by the scale of the baroclinic instability and practically does not depend on resolution, one can tune the scale of the energy return for the stochastic parameterization so that the mean squared wavenumber coincides with the one of the Laplace operator:

$$\overline{k^2} = \frac{\int |\Delta \mathbf{U}_h|^2 dxdy}{\int |\mathbf{U}_h \Delta \mathbf{U}_h| dxdy}. \tag{6.18}$$

Such tuning can be performed at each vertical level separately.

6.4 Relaxation method for determining the characteristics of subgrid parameterizations

Let us give one more argument in favour of the assertion that the energy return in long-wave KEB should occur on the scales of baroclinic instability, while the generation

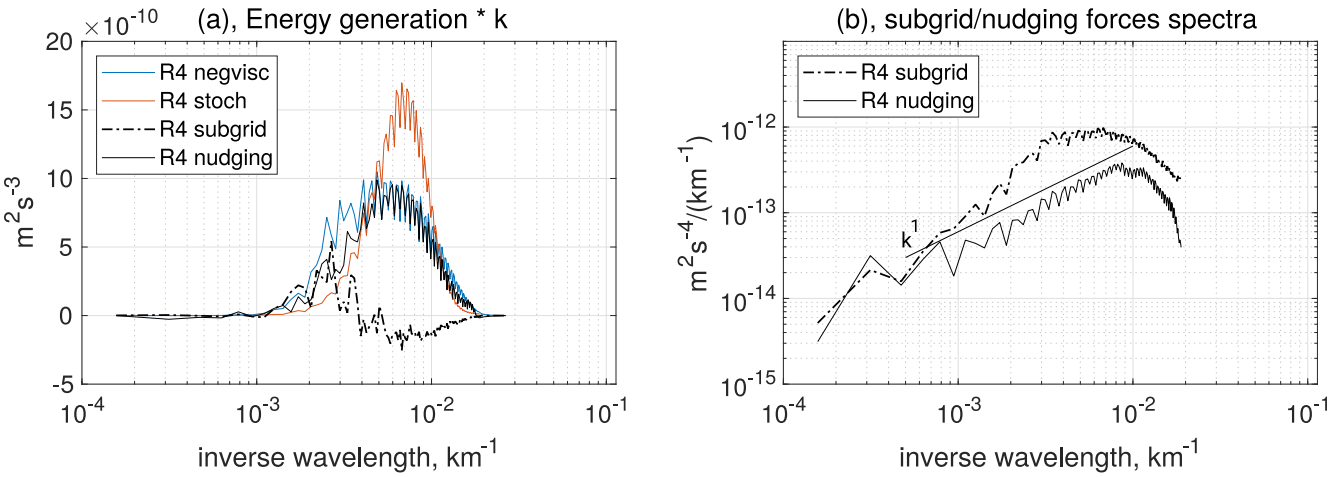

Figure 6.6 — (a), energy influx from the subgrid forces ("R4 subgrid"), from the relaxation ("R4 nudging") and from the KEB parameterizations. (b), spectral density of the subgrid forces and of the relaxation.

spectrum is reproduced by the negative-viscosity operator. In order to tune the long-wave KEB by the spectrum of energy influx from the subgrid forces, it is necessary to have a procedure for separating the energy influx into energy generation and dissipation. As a model of dissipation, a high-order viscosity is usually chosen. However, as follows from Figure 6.5(a), the dissipation at small scales is overestimated by a factor of 3 by the joint model ("negvisc+blp"). This happens because the viscosity coefficient is usually chosen larger than what is predicted by the a priori analysis of the subgrid forces. The most likely reason for the overestimation of the viscosity is the desire to suppress the dispersive errors of the numerical advection schemes in the short-wave range. In turn, the subgrid forces constructed in the standard way (6.14) compensate the dispersive errors of the numerical advection scheme, but this is not taken into account in the construction of simple subgrid-turbulence parameterizations. As a result, the dynamics of the small resolved scales in the a priori analysis of the coarse model and in real computations differ greatly. At the very least, the time scales should differ greatly.

In this connection, one can try to change the methodology of carrying out the a priori analysis. It should have the following two properties:

– The small resolved scales of the coarse model may have significant dispersive errors, but the large scales are reproduced correctly.
– The characteristics of the long-wave KEB parameterization can be constructed for *any* given value of the biharmonic viscosity.

Both properties can be satisfied if we consider the adaptation of the coarse-resolution model to the high-resolution model at a fixed biharmonic-viscosity coefficient:

$$\frac{\partial \mathbf{U}_h^c}{\partial t} = ... + \frac{1}{\tau}\left(\mathcal{P}(\mathbf{U}_h) - \mathbf{U}_h^c\right), \tag{6.19}$$

where the superscript c denotes the fields of the coarse-resolution model. $\tau = 1$ day is the characteristic relaxation time, chosen so that mesoscale eddies are reproduced well. If we compare this time with the characteristic time of another linear operator, the biharmonic viscosity, $\tau_{blp} = 1/(\nu_4 k^4)$, then at wavelengths larger than 90 km the relaxation will predominate, and in the short-wave range, the viscosity. A particular advantage of this procedure is that it takes into account all the inaccuracies inherent to the coarse-resolution model, including the numerical schemes and the peculiarities of operation of various parameterizations at coarse resolution.

The use of the relaxation procedure, i.e. the right-hand side of equation (6.19), for finding the tendency of physical processes unresolved on the grid, is proposed for the first time. In recent works this procedure was proposed for the estimation of free parameters of parameterizations [150], [151]. In those works the optimal values of the free parameters corresponded to the minimum relaxation tendency. Although the attempt to model this tendency may be insufficiently grounded, it nevertheless restores the energy balance in the system and can be used for finding the spectrum of energy generation.

The relaxation was performed for the R4 model, the trajectory of which was pulled towards the R9 model during one year, where the coarsened fields $\mathcal{P}(\mathbf{U}_h)$ of the R9 model were fed into the R4 model with a temporal discreteness of 6 hours. Figure 6.6(a) shows the spectrum of generation of kinetic energy by the relaxation tendency, by the subgrid forces and by the KEB parameterizations. The spectrum of energy generation for the relaxation tendency agrees well with the spectrum of generation for the negative-viscosity model. According to Figure 6.6(b), the spectral density of the relaxation is smaller than that of the subgrid forces. This may indicate that the relaxation, unlike the subgrid forces, does not compensate the dispersive errors of the schemes in the short-wave range (with the used value of τ).

6.5 The negative-viscosity parameterization at eddy-resolving resolution

On the basis of the results of the a priori analysis of the subgrid forces, we came to the conclusion that the negative-viscosity parameterization at any resolution returns energy on the scales of baroclinic instability and does not require additional tuning of the scale. The results of the computations with the negative-viscosity parameterization at $c_{diss} = 0.8$ are given in Figures 6.7, 6.8. A positive effect on the integral eddy heat flux is observed at all resolutions in the range $1/4^o - 1/12^o$ in comparison with the reference computation $1/24^o$, Fig. 6.7. In accordance with the results of the a priori analysis, the amount of returned energy c_{diss} should be decreased as the resolution is increased, since the near-surface eddy heat flux turns out to be overestimated, see "R12 negvisc" in Figure 6.8. By exactly this characteristic we chose c_{diss} at resolution R4 in the previous chapter. At resolution R9 the coefficient $c_{diss} = 0.8$ can be considered acceptable. The norms of errors in the mean fields are given in Table 8. At resolutions R4 and R9 the application of the negative-viscosity parameterization leads to a decrease or a non-increase of all error norms. At resolution R12 almost all error norms increase: an error appears in the northern region in the fields of temperature and salinity.

Table 8 — Norms of errors in the 20-year mean sea-surface temperature, sea-surface height and surface salinity (SST, SSH, SSS) between the coarse models (R_c) and the high-resolution model ($R24$). Results for the negative-viscosity parameterization. The following two norms for an arbitrary field $\varphi(x,y)$ are separated by a semicolon: $\max(|\varphi_{R_c} - \varphi_{R24}|)$; $\text{mean}(|\varphi_{R_c} - \varphi_{R24}|)$.

	SST, C^o	SSH, m	SSS, psu
R4	8.8; 0.54	0.75; 0.1	0.65; 0.16
R4 negvisc	5.3; 0.45	0.63; 0.08	0.45; 0.15
R9	3.8; 0.22	0.6; 0.04	0.37; 0.06
R9 negvisc	2.15; 0.2	0.18; 0.03	0.26; 0.06
R12	2.0; 0.13	0.21; 0.024	0.22; 0.04
R12 negvisc	1.1; 0.17	0.24; 0.03	0.21; 0.06

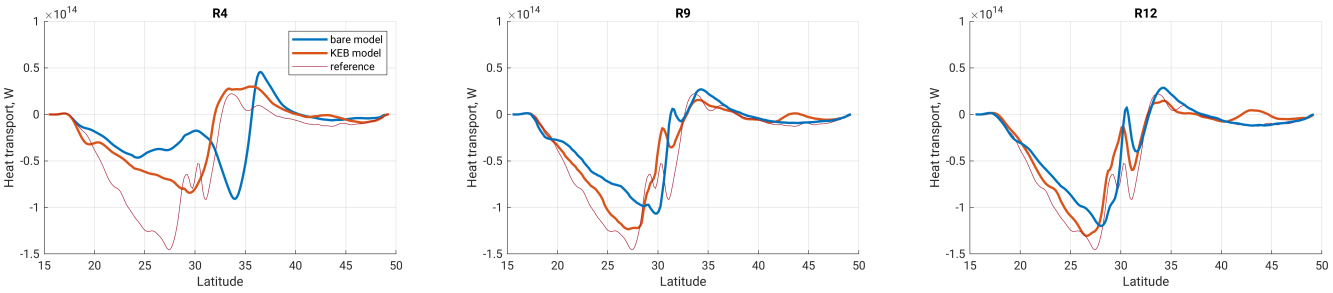

Figure 6.7 — Mean meridional eddy heat flux, integrated over depth, W. Models without parameterization ("bare model") and with the negative-viscosity parameterization ("KEB model") in comparison with the R24 model ("reference").

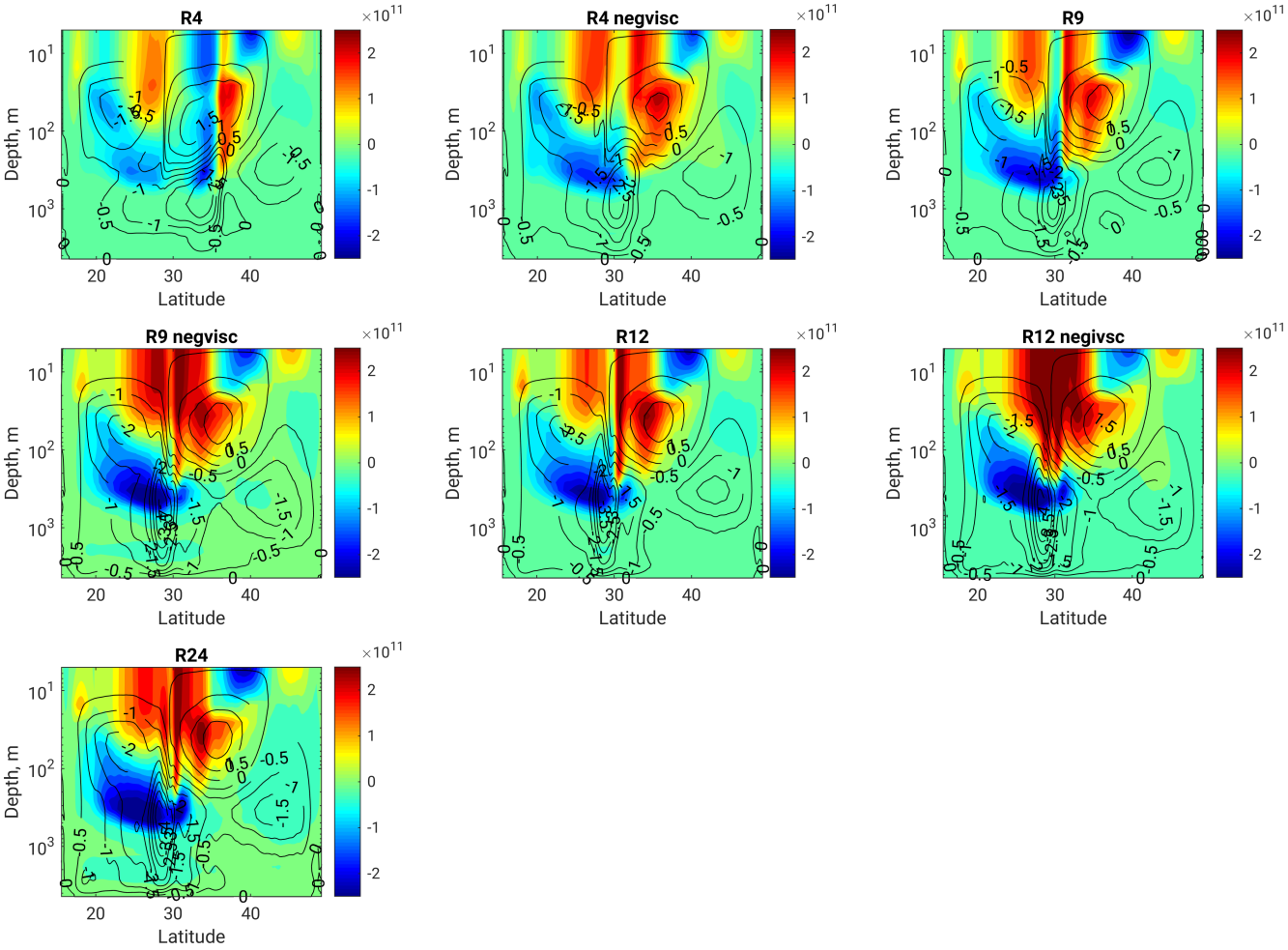

Figure 6.8 — Colour: distribution over depth of the meridional eddy heat flux, $\mathrm{W} \cdot \mathrm{m}^{-1}$. Lines: meridional streamfunction, in Sverdrups. Results for the negative-viscosity parameterization.

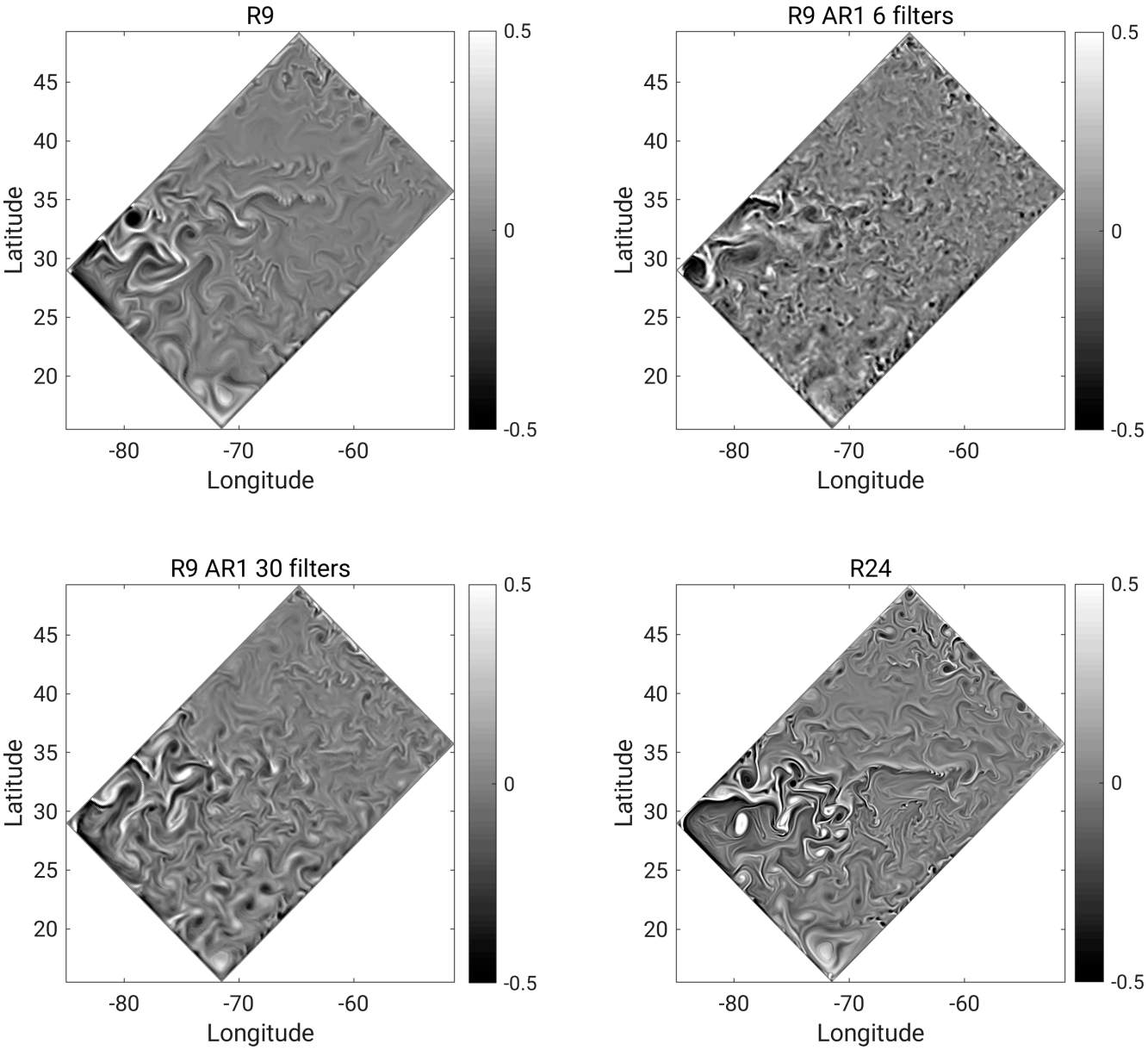

Figure 6.9 — Relative vorticity at the surface in units of the Coriolis parameter for the R9, R24 models, and also for the R9 models with the AR1 stochastic parameterization, see Appendix D, for various numbers of applied filterings. March 30 after the spin-up of the models.

6.6 Choice of the scale of the stochastic parameterization at eddy-resolving resolution

In this section we propose to find out whether the scale of energy return for the stochastic parameterization should depend on the grid step. The AR1 stochastic parameterization described in Appendix D is studied for the R9 model. The amount of returned energy $c_{diss} = 0.8$. To construct the short-wave KEB parameterization, the

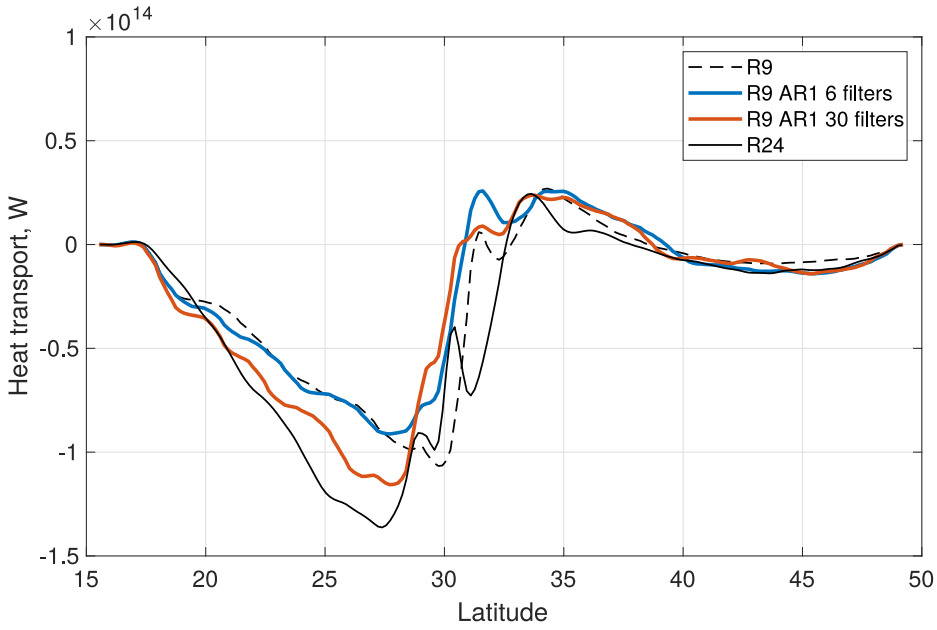

Figure 6.10 — Mean meridional eddy heat flux, integrated over depth, W. Results for the AR1 stochastic parameterization.

Table 9 — Norms of errors in the 20-year mean sea-surface temperature, sea-surface height and surface salinity (SST, SSH, SSS) between the coarse models (R_c) and the high-resolution model ($R24$). Results for the stochastic parameterization. The following two norms for an arbitrary field $\varphi(x,y)$ are separated by a semicolon: $\max(|\varphi_{R_c} - \varphi_{R24}|)$; $\text{mean}(|\varphi_{R_c} - \varphi_{R24}|)$.

	SST, C^o	SSH, m	SSS, psu
R9	3.8; 0.22	0.6; 0.04	0.37; 0.06
R9 AR1 6 filters	3.8; 0.25	0.52; 0.05	0.44; 0.06
R9 AR1 30 filters	3.8; 0.25	0.32; 0.04	0.43; 0.07

number of filterings equal to 6 is used, as at resolution R4. The scale of the long-wave KEB parameterization should not depend on the grid step, accordingly, we choose 30 filterings so that the scale of energy return is the same in the R4 and R9 models. Here it is assumed that the width of the resulting filter is proportional to the square root of the number of applications, i.e. $26.5\text{km}\sqrt{6} \approx 11.7\text{km}\sqrt{30}$.

The maximum energy influx for the parameterization AR1 6 filters at resolution R9 falls on the wavelength of 63 km, which corresponds to the submesoscale range. As follows from Figure 6.9, this parameterization too strongly excites small eddies, compared with the high-resolution model R24. The meridional eddy heat flux is reproduced better by the parameterization AR1 30 filters, Fig. 6.10; this is associated with the good reproduction of the eddy flux at depths greater than 100 metres, Fig. 6.11. One can

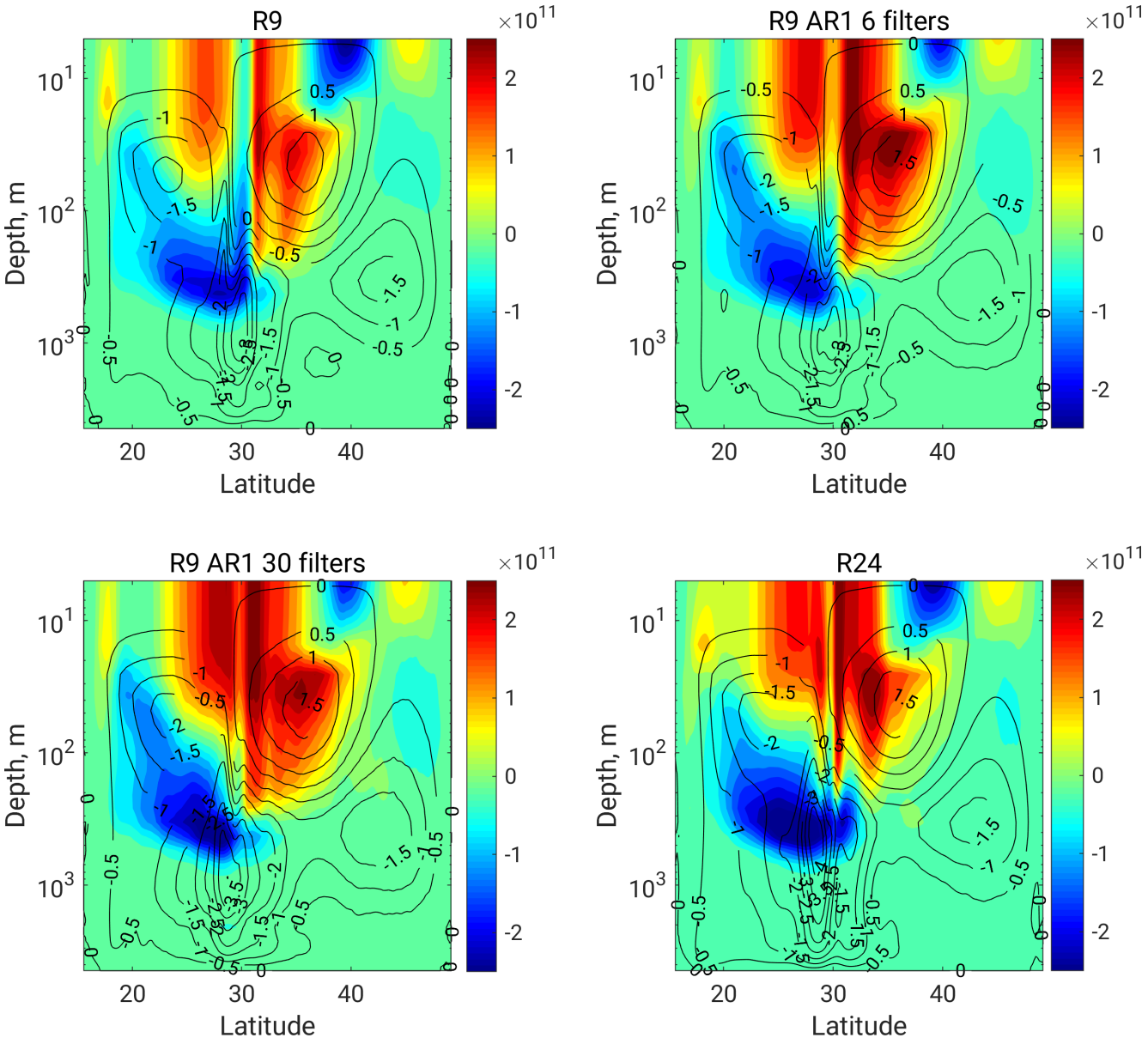

Figure 6.11 — Colour: distribution over depth of the meridional eddy heat flux, $\mathrm{W} \cdot \mathrm{m}^{-1}$. Lines: meridional streamfunction, in Sverdrups.

also note the stronger meridional overturning circulation near the bottom in the AR1 30 filters model, in agreement with the high-resolution model, Fig. 6.11. Although the solutions visually differ significantly for the two parameterizations, the errors in the mean near-surface fields of temperature and salinity are approximately the same, and worse than in the R9 model without parameterization, see Table 9. The R9 AR1 30 filters model better reproduces the mean sea-surface height.

6.7 Conclusions

The results of this chapter are presented in the following list:

– In the primitive equations of the ocean, the poorly resolved inverse energy cascade on the grid can be enhanced both in eddy-permitting and in eddy-resolving models by means of KEB parameterizations.

– If the dissipation is described by the biharmonic-viscosity operator, then the spectrum of energy return is well described by the negative-viscosity operator.

– The scale of energy return *in this case* should correspond to the scales of baroclinic instability.

– If the scale is chosen to be smaller, i.e. falls into the submesoscale range, then too-small eddies are excited. If, on the contrary, the scale is chosen to be larger, then destruction of large-scale anisotropic coherent structures, such as jet flows, is possible.

– At eddy-resolving resolution the negative-viscosity model reproduces the mean near-surface fields significantly better than the stochastic parameterization.

– The scale-similarity model reproduces the energy generation at large scales (larger than 300 km); however, in order to filter out the small dissipative scales, the application of too large a number of filters would be required.

– The amount of returned energy depends on which physical processes are resolved on the grid. Thus, with the partial resolution of the forward energy cascade in the submesoscale range, it is necessary to reduce the strength of the parameterization, and with insufficient resolution of the mesoscale range it is necessary to take into account the baroclinic instability unresolved on the grid (values $c_{diss} > 1$ in formula (6.15)). In particular, the formula for the local value $c_{diss} = \left(1 + \dfrac{Ro}{Ro_{diss}}\right)^{-1}$, proposed in [141], which parameterizes the local weakening of the inverse energy cascade due to the local imbalance of the flow, has been confirmed experimentally.

Conclusion

In this dissertation an analysis and testing of parameterizations of subgrid quasi-two-dimensional turbulence intended for use in ocean models at eddy-permitting resolution has been carried out. In the first two chapters of the dissertation, the role of numerical approximations of advection in the formation of coherent structures in an ideal fluid and of the inverse energy cascade in forced turbulence is investigated in detail. It is shown that the most successful are the numerical approximations that preserve the first two Casimirs – vorticity and enstrophy.

In the third chapter, an a priori analysis of the subgrid forces in the problem of forced homogeneous turbulence is carried out, taking into account the numerical approximations of advection. It is shown that the under-resolved energy generation in the long-wave range practically does not depend on the choice of the numerical advection approximation (for second-order schemes) and corresponds to the scales of the inertial interval of the inverse energy cascade. Three KEB parameterizations returning energy to the large scales are proposed: the negative-viscosity model, a stochastic parameterization, and the scale-similarity model (after the application of a short-wave filter that removes the small dissipative scales). The parameterizations make it possible to restore the density of kinetic energy at large scales, the autocorrelation functions of the solution and the sensitivity to a constant external forcing. In the fourth chapter of the dissertation, the influence of the subgrid parameterizations on the development of barotropic instability is investigated. It is shown that the parameterizations bring forward the moment of onset of the turbulent flow regime, and do so in different ways: the stochastic parameterization excites unstable modes; the scale-similarity model modifies the linearized system, thereby increasing the growth rates of the unstable modes; and the negative-viscosity model prevents the smoothing of the mean flow caused by the action of the eddy-viscosity model.

In the fifth chapter of the dissertation, the KEB parameterizations, the negative-viscosity and the stochastic one, are investigated in the NEMO ocean model in the Double Gyre configuration at eddy-permitting resolution ($1/4^o$). It is shown that the parameterizations are able to restore the eddy heat flux and the meridional overturning circulation. In the sixth chapter of the dissertation, an analysis of the subgrid forces in the same configuration of the NEMO model is carried out. It is shown that the scale of the under-resolved long-wave energy generation corresponds to the scale of block-

age of the inverse energy cascade and does not depend on the resolution of the coarse model. The KEB parameterizations tuned in the previous chapter of the dissertation return energy at a smaller scale – the scale of baroclinic instability. An assumption is made that, if the dissipation is described by the biharmonic-viscosity operator, then the scale of energy return should not depend on the resolution of the coarse model and is determined by the scale of baroclinic instability. It is shown that, as the resolution is increased, the amount of returned energy with respect to the dissipated one should be reduced, which is associated with the gradual resolution on the grid of submesoscale eddies. Preliminary experiments with KEB parameterizations at eddy-resolving resolution have shown that the negative-viscosity model can be used up to resolution $1/12^o$. It is, however, recommended to reduce the amount of returned energy. The stochastic parameterization is able to restore the eddy heat flux if the scale of energy return corresponds to the scales of baroclinic instability. However, no improvements in the mean near-surface fields are observed for it.

On the basis of the results of the dissertation, the following recommendations on the inclusion of KEB parameterizations in more realistic configurations of ocean models can be proposed:

1. Computations with the stochastic KEB parameterization possess larger errors in the mean fields; the parameterization requires tuning of the scale of energy return, and in addition, in order to generate a random field with a large correlation radius, large computational costs for the construction of the smoothing filter will be required. When using a time autoregressive model, additional procedures are needed for an accurate computation of the energy coming from the parameterization (Appendix D). For these reasons, the negative-viscosity parameterization is preferable.
2. It is necessary to switch off the KEB near the lateral boundaries by one of the ways given in Chapter 6. It is necessary to take into account the dissipation associated with the numerical advection schemes. It may be necessary to take into account the dissipation of available potential energy associated with the isopycnal-diffusion operator.

In conclusion, the author expresses gratitude to the scientific advisor A. V. Glazunov and to the coauthors of the works V. P. Dymnikov, A. S. Gritsun, E. V. Mortikov, E. M. Volodin, and also to V. N. Lykosov, N. G. Yakovlev, Yu. M. Nechepurenko, K. V. Demyanko and V. V. Shashkin for constructive remarks.

Appendix A

External stochastic forcing

Depending on the chosen variables $(\mathbf{u},p)$ or (ψ,ω), the forcing has the form

$$\mathbf{f} = \begin{bmatrix} a \\ b \end{bmatrix} \cdot \sin(\mathbf{k}\cdot\mathbf{x}+\varphi) \quad \text{or} \quad f = c\cdot\sin(\mathbf{k}\cdot\mathbf{x}+\varphi),$$

where $\varphi \in [0, 2\pi)$ is the phase. The wavevector $\mathbf{k} = (k_1, k_2)$ lies in a thin circular shell about the wavenumber k_f:

$$\|\mathbf{k}\|_2 \in \left(k_f - \frac{k_\delta}{2}, k_f + \frac{k_\delta}{2}\right).$$

The wavenumbers k_1, k_2 are chosen to be integer, and the width of the shell is $k_\delta = 4$.

The integration in time is performed by means of an explicit Euler scheme, and at each time step the quantities φ, k_1, k_2 are chosen randomly. In this case the energy influx per unit surface area ε depends on the second norm of the forcing and on the time step (see [127]):

$$\varepsilon = \frac{1}{2}\Delta t \|\mathbf{f}\|_2^2 \;/\; S = \frac{\Delta t}{4}(a^2+b^2), \tag{A.1}$$

where S is the area of the domain. An additional condition on the coefficients a,b is obtained from the non-divergence condition:

$$\nabla_h \cdot \mathbf{f} = 0 \rightarrow \begin{bmatrix} k_1' & k_2' \end{bmatrix} \cdot \begin{bmatrix} a \\ b \end{bmatrix} = 0, \tag{A.2}$$

where ∇_h is the finite-difference gradient operator (2.7), and k_1',k_2' are its modified wavenumbers. Finally, having chosen the time step Δt and the energy influx ε, one can find the coefficients a,b from equations (A.1), (A.2). The coefficient c is determined from the discrete relation between vorticity and velocity.

Appendix B

Preliminary testing of the short-wave stochastic parameterization

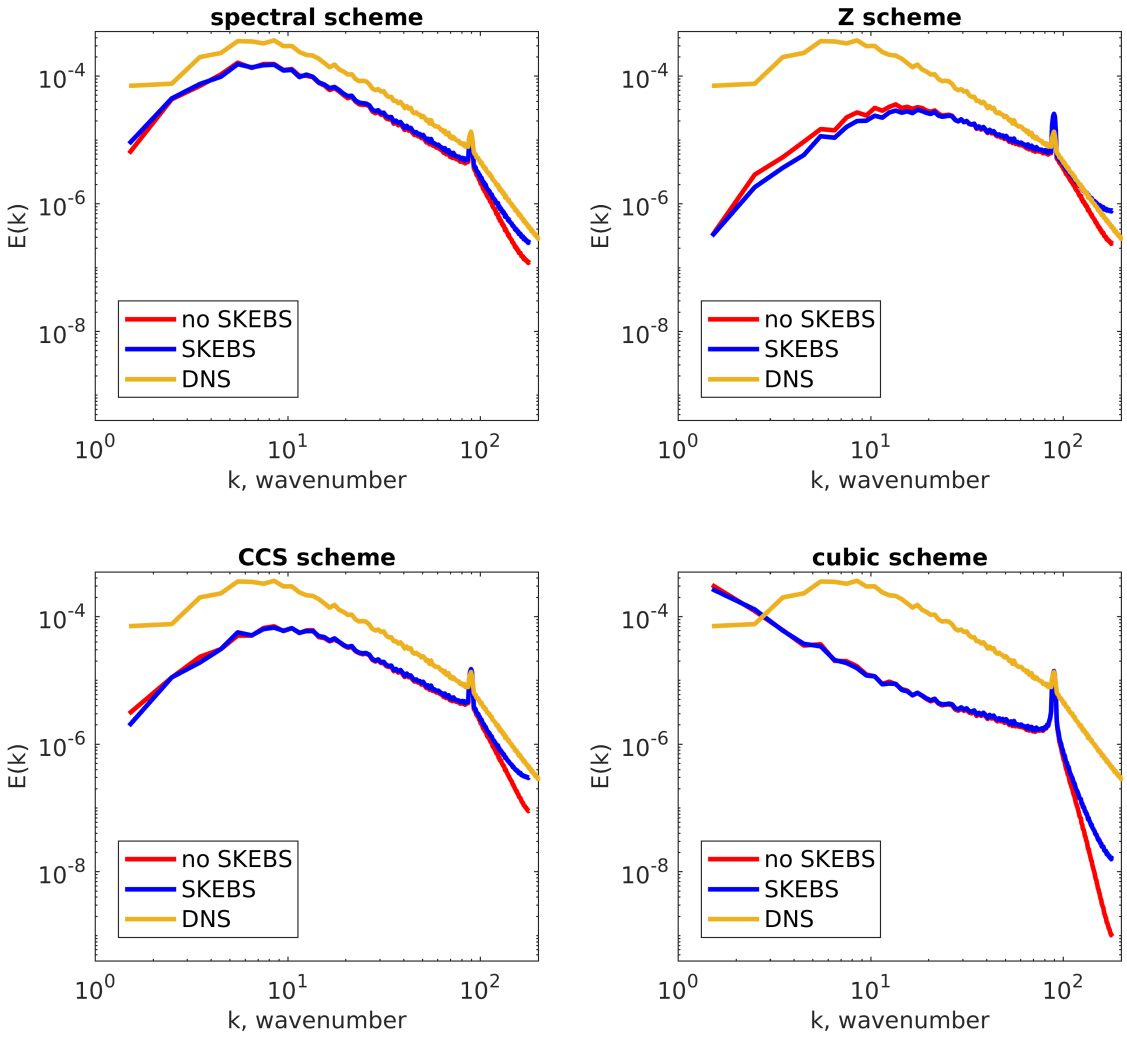

Figure B.1 — Spectral density of energy $E(k)$ in the statistically equilibrium state for four schemes at resolution 360^2. The coarse model without parameterization ("no SKEBS"), with the parameterization switched on ("SKEBS") and the computation at high resolution ("DNS"). "spectral" – pseudospectral scheme [152].

In the work [77] the spectral density of energy influx from the stochastic parameterization is chosen proportional to $k^{0.46}$. Such a spectral slope corresponds to the spectral density of the subgrid forces, as will be shown in Section 6.2 of Chapter 6. In this appendix the stochastic parameterization has spectral power $\sim k^{0.46}$ and is chosen

on the enstrophy inertial interval $(90 \leqslant k \leqslant 180)$, while the energy influx from the parameterization amounts to 30% of the strength of the external forcing ε. As follows from Figure B.1, the parameterization excites small scales $(90 \leqslant k \leqslant 180)$; however, on the scales of the inertial interval of the inverse energy cascade $(0 \leqslant k \leqslant 90)$ the changes of the energy density are insignificant. In this way we have shown that a stochastic excitation located on the enstrophy interval near the grid scale does not allow to restore the inverse energy cascade. In Chapter 3 it is shown that when the stochastic excitation corresponds to the inertial interval of the inverse energy cascade, the spectral density of energy at the large scales can be restored.

Appendix C

Hadamard well-posedness (stability to initial data) for the negative-viscosity parameterization

The diffusion equation with a negative diffusion coefficient is an ill-posed problem. However, in this dissertation we use a negative viscosity coefficient only jointly with the biharmonic viscosity. Such equations are called Kuramoto–Sivashinsky equations [153—155]. In this appendix we shall show that the linear part of the Kuramoto–Sivashinsky equation in the one-dimensional case is stable with respect to initial data on a finite interval of time.

Consider on the periodic interval $\Omega = [0,2\pi)$ the following equation:

$$\partial_t u(x,t) = -\partial_{xx}(\nu_4 \partial_{xx} + \nu_2) u(x,t),\ \nu_4 > 0,\ \nu_2 > 0. \tag{C.1}$$

In Fourier space we obtain:

$$\partial_t u_k(t) = k^2(\nu_2 - \nu_4 k^2) u_k(t) = \lambda(k) u_k(t),\ k \in \mathbb{Z}. \tag{C.2}$$

The function $\lambda(k)$ is bounded above:

$$\lambda(k) \leqslant \frac{\nu_2^2}{4\nu_4},\ \text{for } \nu_4 > 0,\ \nu_2 > 0. \tag{C.3}$$

Let $\delta u(x,0)$ be a perturbation of the initial data. Then the perturbation of the solution at the time moment T in Fourier space is:

$$\delta u_k(T) = \delta u_k(0) e^{\lambda(k)T}. \tag{C.4}$$

In the L_2 norm, $||u(x)||^2 = \sum_{k\in\mathbb{Z}} |u_k|^2$, we have the following inequality:

$$||\delta u(x,T)||^2 = \sum_{k\in\mathbb{Z}} |\delta u_k(0)|^2 e^{2\lambda(k)T} \leqslant \exp\left(\frac{\nu_2^2}{2\nu_4} T\right) ||\delta u(x,0)||^2 \to \tag{C.5}$$

$$||\delta u(x,T)|| \leqslant \exp\left(\frac{\nu_2^2}{4\nu_4} T\right) ||\delta u(x,0)||, \tag{C.6}$$

i.e. on an arbitrary *finite* interval of time the problem is stable with respect to initial data. In turn, the diffusion equation is uniformly stable on an arbitrary interval of time, whereas the diffusion equation with a negative diffusion coefficient is unstable on an arbitrary interval of time.

The characteristic time of divergence of the trajectories for the NEMO model in the Double Gyre configuration at resolution $1/4^o$ is:

$$T = 4\frac{\nu_4}{\nu_2^2} \approx 4\frac{5 \cdot 10^{11}\mathrm{m}^4/\mathrm{s}}{1000^2\mathrm{m}^4/\mathrm{s}^2} \approx 23 \text{ days}, \tag{C.7}$$

which is comparable to the characteristic times of mesoscale eddies ≈ 30 days.

Appendix D

Stochastic parameterization with a time autoregressive process

Here we give a modification of the stochastic parameterization from Section 5.2.2 taking into account the time correlation of the stochastic tendency by means of the use of an AR1 process, as proposed in [77]. We construct a random streamfunction:

$$\hat{\psi}\left(x,y,z,t^n\right) = \varphi\left(x,y,t^n\right) \cdot \sqrt{\max\left(\dot{E}_{diss},0\right)}\,, \tag{D.1}$$

where φ is grid noise white in time and space with distribution $N(0,1)$. According to [67], we construct a correlated stochastic tendency, $\psi(x,y,z,t^n)$, as follows:

$$\psi(x,y,z,t^{n+1}) = \psi(x,y,z,t^n)(1-\frac{\Delta t}{\tau}) + \left[\frac{\Delta t}{\tau}\left(2-\frac{\Delta t}{\tau}\right)\right]^{1/2} \alpha S^{n_s}\left(\hat{\psi}\right). \tag{D.2}$$

The resulting process ψ has correlation time τ. In addition, this form of writing the AR1 process provides correlation without changing the variance, namely:

$$\left\langle \left|\nabla_h^{\perp}\psi\right|^2 \right\rangle = \alpha^2 \left\langle \left|\nabla_h^{\perp} S^{n_s}\left(\hat{\psi}\right)\right|^2 \right\rangle. \tag{D.3}$$

The streamfunction ψ modifies equation (5.2) as follows:

$$\frac{\partial \mathbf{U}_h}{\partial t} = \cdots + \nabla_h^{\perp}\psi. \tag{D.4}$$

Since the energy influx from the tendency ψ equals $\tau\left\langle \left|\nabla_h^{\perp}\psi\right|^2 \right\rangle$, we choose the amplitude α so that the following equality is satisfied:

$$\alpha^2\tau \int \left\langle \left|\nabla_h^{\perp} S^{n_s}\left(\hat{\psi}\right)\right|^2 \right\rangle dxdydz = c_{diss}\int \dot{E}_{diss}dxdydz. \tag{D.5}$$

As in Section 5.2.2, we use the approximation:

$$\int \left\langle \left|\nabla_h^{\perp} S^{n_s}\left(\hat{\psi}\right)\right|^2 \right\rangle dxdydz \approx \int \left|\nabla_h^{\perp} S^{n_s}\left(\hat{\psi}\right)\right|^2 dxdydz. \tag{D.6}$$

Correction of the energy influx. The energy influx for the AR1 parameterization is computed under the assumption that the stochastic tendency is not correlated with the other right-hand sides of the equation. In practice it often turns out that the actual

energy influx, $\left\langle \nabla_h^{\perp}\psi \cdot \mathbf{U}_h \right\rangle$, turns out to be less than the theoretical one, $\tau \left\langle \left| \nabla_h^{\perp}\psi \right|^2 \right\rangle$. We have proposed an automatic amplitude-correction procedure. We leave the way of generating the stochastic tendency described above unchanged, and modify only the final amplitude of the tendency:

$$\frac{\partial \mathbf{U}_h}{\partial t} = \cdots + \beta \nabla_h^{\perp}\psi, \tag{D.7}$$

where β is a number greater than unity. Let us equate the integral energy influx to the dissipation:

$$\beta \int \left\langle \nabla_h^{\perp}\psi \cdot \mathbf{U}_h \right\rangle dxdydz = c_{diss} \int \dot{E}_{diss} dxdydz, \tag{D.8}$$

then one can obtain an estimate of β as follows:

$$\beta(t) = \frac{c_{diss} \int_0^t \int \dot{E}_{diss} dxdydzdt'}{\int_0^t \int \nabla_h^{\perp}\psi \cdot \mathbf{U}_h dxdydzdt'}. \tag{D.9}$$

Here the time-averaging is performed in order to accumulate a sufficient amount of statistics. If the estimated value of β falls outside the interval $(1,3)$, then β is set equal to the boundary values of this interval. For the experiment with the R4 model and the AR1 parameterization, with $n_s = 6$ and $c_{diss} = 0.8$, the graph of $\beta(t)$ is given in Figure D.1. It has been verified experimentally that with such a choice of $\beta(t)$ the time integral over 20 years of the incoming energy differs by approximately 1.5% from the prescribed value, see Figure D.2. The value $\beta = 1.17$ found in this way increases the energy influx by $(1.17^2 - 1) \cdot 100\% \approx 37\%$.

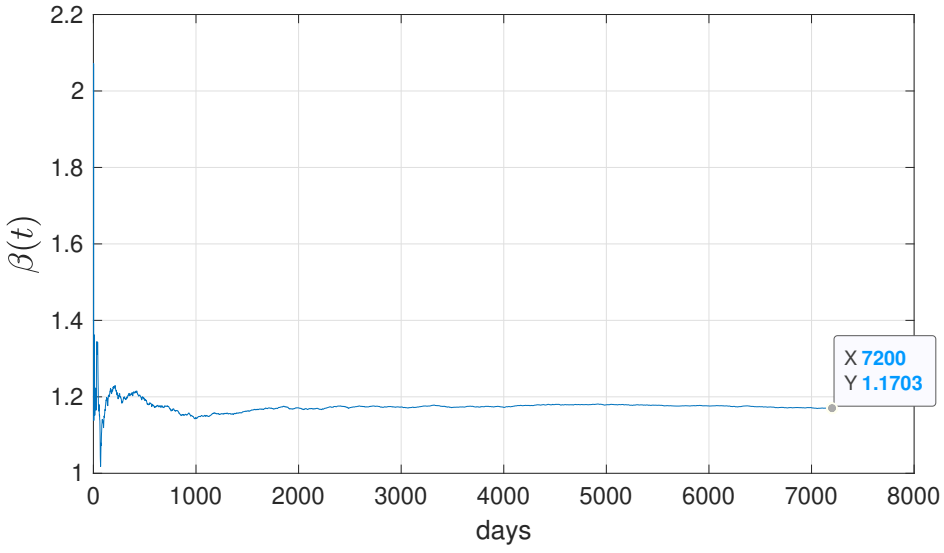

Figure D.1 — $\beta(t)$ for the R4 model at $c_{diss} = 0.8$ and $n_s = 6$.

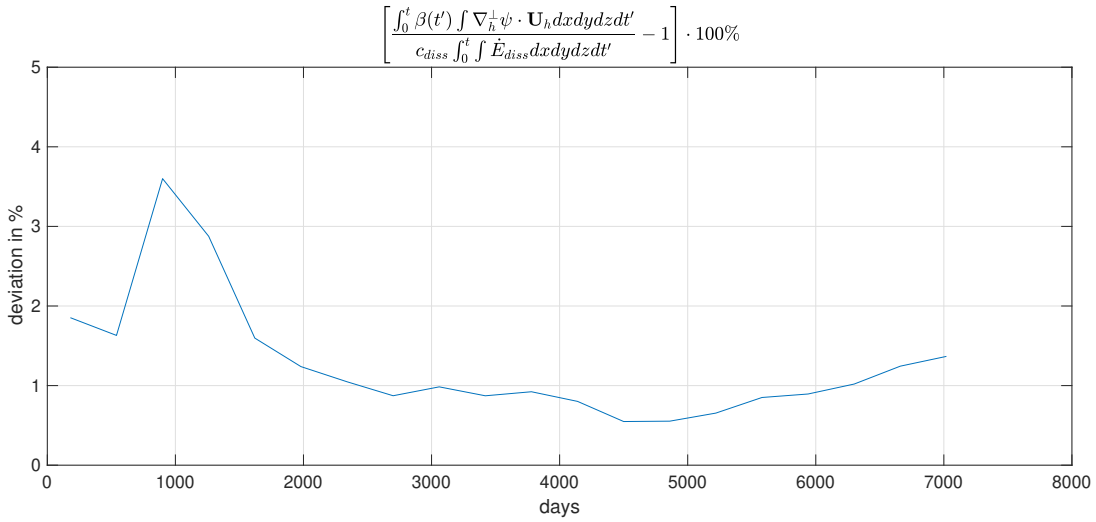

Figure D.2 — Deviation of the energy influx from the prescribed one in percent for the R4 model at $c_{diss} = 0.8$ and $n_s = 6$.

Author's publications on the dissertation topic

1. *Пережогин, П. А.* Равновесные состояния конечномерных аппроксимаций уравнений двумерной идеальной жидкости / П. А. Пережогин, В. П. Дымников // Нелинейная динамика. — 2017. — Vol. 13, no. 1. — P. 55—79.
2. *Пережогин, П.* Моделирование квазиравновесных состояний двумерной идеальной жидкости / П. Пережогин, В. Дымников // Доклады академии наук. — 2017. — Vol. 474, no. 1. — P. 36—40.
3. Comparison of numerical advection schemes in two-dimensional turbulence simulation / P. A. Perezhogin [et al.] // Russian Journal of Numerical Analysis and Mathematical Modelling. — 2017. — Vol. 32, no. 1. — P. 47—60.
4. *Дымников, В.* О системах гидродинамического типа, аппроксимирующих уравнения двумерной идеальной жидкости / В. Дымников, П. Пережогин // Известия Российской академии наук. Физика атмосферы и океана. — 2018. — Vol. 54, no. 3. — P. 272—282.
5. *Perezhogin, P. A.* Stochastic and deterministic kinetic energy backscatter parameterizations for simulation of the two-dimensional turbulence / P. A. Perezhogin, A. V. Glazunov, A. S. Gritsun // Russian Journal of Numerical Analysis and Mathematical Modelling. — 2019. — Vol. 34, no. 4. — P. 197—213.
6. *Perezhogin, P. A.* 2D turbulence closures for the barotropic jet instability simulation / P. A. Perezhogin // Russian Journal of Numerical Analysis and Mathematical Modelling. — 2020. — Vol. 35, no. 1. — P. 21—35.
7. *Perezhogin, P. A.* Testing of kinetic energy backscatter parameterizations in the NEMO ocean model / P. A. Perezhogin // Russian Journal of Numerical Analysis and Mathematical Modelling. — 2020. — Vol. 35, no. 2. — P. 69—82.
8. *Perezhogin, P.* Deterministic and stochastic parameterizations of kinetic energy backscatter in the NEMO ocean model in Double-Gyre configuration / P. Perezhogin // IOP Conference Series: Earth and Environmental Science. Vol. 386. — IOP Publishing. 2019. — P. 012025.

References

9. *Sagaut*, *P.* Large eddy simulation for incompressible flows: an introduction / P. Sagaut. — Springer Science & Business Media, 2006.
10. *Vallis*, *G. K.* Atmospheric and oceanic fluid dynamics / G. K. Vallis. — Cambridge University Press, 2017.
11. *Должанский*, *Ф.* Основы геофизической гидродинамики / Ф. Должанский. — Физматлит, 2011.
12. *Vallis*, *G. K.* Generation of mean flows and jets on a beta plane and over topography / G. K. Vallis, M. E. Maltrud // Journal of physical oceanography. — 1993. — Vol. 23, no. 7. — P. 1346—1362.
13. Scale-aware deterministic and stochastic parametrizations of eddy-mean flow interaction / L. Zanna [et al.] // Ocean Modelling. — 2017. — Vol. 111. — P. 66—80.
14. Seasonality in submesoscale turbulence / J. Callies [et al.] // Nature communications. — 2015. — Vol. 6, no. 1. — P. 1—8.
15. *Callies*, *J.* Interpreting energy and tracer spectra of upper-ocean turbulence in the submesoscale range (1–200 km) / J. Callies, R. Ferrari // Journal of Physical Oceanography. — 2013. — Vol. 43, no. 11. — P. 2456—2474.
16. *Rhines*, *P. B.* Geostrophic turbulence / P. B. Rhines // Annual Review of Fluid Mechanics. — 1979. — Vol. 11, no. 1. — P. 401—441.
17. *McWilliams*, *J. C.* The nature and consequences of oceanic eddies / J. C. McWilliams // Ocean modeling in an eddying regime. — 2008. — Vol. 177. — P. 5—15.
18. *Kraichnan*, *R. H.* Inertial ranges in two-dimensional turbulence / R. H. Kraichnan // The Physics of Fluids. — 1967. — Vol. 10, no. 7. — P. 1417—1423.
19. *Leith*, *C. E.* Diffusion approximation for two-dimensional turbulence / C. E. Leith // The Physics of Fluids. — 1968. — Vol. 11, no. 3. — P. 671—672.
20. *Batchelor*, *G. K.* Computation of the energy spectrum in homogeneous two-dimensional turbulence / G. K. Batchelor // The Physics of Fluids. — 1969. — Vol. 12, no. 12. — P. II—233.

21. *Boffetta*, *G.* Inverse energy cascade in two-dimensional turbulence: Deviations from Gaussian behavior / G. Boffetta, A. Celani, M. Vergassola // Physical Review E. — 2000. — Vol. 61, no. 1. — R29.

22. *Salmon*, *R.* Baroclinic instability and geostrophic turbulence / R. Salmon // Geophysical & Astrophysical Fluid Dynamics. — 1980. — Vol. 15, no. 1. — P. 167—211.

23. Evaluation of climate models / G. Flato [et al.] // Climate change 2013: the physical science basis. Contribution of Working Group I to the Fifth Assessment Report of the Intergovernmental Panel on Climate Change. — Cambridge University Press, 2014. — P. 741—866.

24. *Redi*, *M. H.* Oceanic isopycnal mixing by coordinate rotation / M. H. Redi // Journal of Physical Oceanography. — 1982. — Vol. 12, no. 10. — P. 1154—1158.

25. *Gent*, *P. R.* Isopycnal mixing in ocean circulation models / P. R. Gent, J. C. Mcwilliams // Journal of Physical Oceanography. — 1990. — Vol. 20, no. 1. — P. 150—155.

26. High resolution model intercomparison project (HighResMIP v1. 0) for CMIP6 / R. J. Haarsma [et al.] // Geoscientific Model Development. — 2016. — Vol. 9, no. 11. — P. 4185—4208.

27. Impact of partial steps and momentum advection schemes in a global ocean circulation model at eddy-permitting resolution / B. Bernard [et al.] // Ocean dynamics. — 2006. — Vol. 56, no. 5/6. — P. 543—567.

28. *Maltrud*, *M. E.* Energy and enstrophy transfer in numerical simulations of two-dimensional turbulence / M. E. Maltrud, G. K. Vallis // Physics of Fluids A: Fluid Dynamics. — 1993. — Vol. 5, no. 7. — P. 1760—1775.

29. *Данилов*, *С. Д.* Квазидвумерная турбулентность / С. Д. Данилов, Г. Давид // Успехи физических наук. — 2000. — Vol. 170, no. 9. — P. 921—968.

30. *Ghosal*, *S.* An analysis of numerical errors in large-eddy simulations of turbulence / S. Ghosal // Journal of Computational Physics. — 1996. — Vol. 125, no. 1. — P. 187—206.

31. *Bouchet*, *F.* Statistical mechanics of two-dimensional and geophysical flows / F. Bouchet, A. Venaille // Physics reports. — 2012. — Vol. 515, no. 5. — P. 227—295.

32. *Robert, R.* Statistical equilibrium states for two-dimensional flows / R. Robert, J. Sommeria // Journal of Fluid Mechanics. — 1991. — Vol. 229. — P. 291—310.

33. *Arakawa, A.* Computational design for long-term numerical integration of the equations of fluid motion: Two-dimensional incompressible flow. Part I / A. Arakawa // Journal of computational physics. — 1966. — Vol. 1, no. 1. — P. 119—143.

34. *Frank, J.* A Hamiltonian particle-mesh method for the rotating shallow-water equations / J. Frank, G. Gottwald, S. Reich // Meshfree methods for partial differential equations. — Springer, 2003. — P. 131—142.

35. *Zeitlin, V.* Finite-mode analogs of 2D ideal hydrodynamics: Coadjoint orbits and local canonical structure / V. Zeitlin // Physica D: Nonlinear Phenomena. — 1991. — Vol. 49, no. 3. — P. 353—362.

36. *Abramov, R. V.* Statistically relevant and irrelevant conserved quantities for the equilibrium statistical description of the truncated Burger-Hopf equation and the equations for barotropic flow / R. V. Abramov. — 2002.

37. *Dubinkina, S.* Statistical relevance of vorticity conservation in the Hamiltonian particle-mesh method / S. Dubinkina, J. Frank // Journal of Computational Physics. — 2010. — Vol. 229, no. 7. — P. 2634—2648.

38. *Dubinkina, S.* Relevance of conservative numerical schemes for an Ensemble Kalman Filter / S. Dubinkina // Quarterly Journal of the Royal Meteorological Society. — 2018. — Vol. 144, no. 711. — P. 468—477.

39. *Palmer, T.* Towards the probabilistic Earth-system simulator: a vision for the future of climate and weather prediction / T. Palmer // Quarterly Journal of the Royal Meteorological Society. — 2012. — Vol. 138, no. 665. — P. 841—861.

40. *Chasnov, J. R.* Simulation of the Kolmogorov inertial subrange using an improved subgrid model / J. R. Chasnov // Physics of Fluids A: Fluid Dynamics. — 1991. — Vol. 3, no. 1. — P. 188—200.

41. *Frederiksen, J. S.* Dynamical subgrid-scale parameterizations from direct numerical simulations / J. S. Frederiksen, S. M. Kepert // Journal of the atmospheric sciences. — 2006. — Vol. 63, no. 11. — P. 3006—3019.

42. An energy-conserving restoration scheme for the shallow-water equations / J. Kent [et al.] // Quarterly Journal of the Royal Meteorological Society. — 2016. — Vol. 142, no. 695. — P. 1100—1110.

43. *Frederiksen, J. S.* Eddy viscosity and stochastic backscatter parameterizations on the sphere for atmospheric circulation models / J. S. Frederiksen, A. G. Davies // Journal of the atmospheric sciences. — 1997. — Vol. 54, no. 20. — P. 2475—2492.

44. *Bardina, J.* Improved subgrid-scale models for large-eddy simulation / J. Bardina, J. Ferziger, W. Reynolds // 13th fluid and plasmadynamics conference. — 1980. — P. 1357.

45. *Meneveau, C.* Scale-invariance and turbulence models for large-eddy simulation / C. Meneveau, J. Katz // Annual Review of Fluid Mechanics. — 2000. — Vol. 32, no. 1. — P. 1—32.

46. *Nadiga, B.* Orientation of eddy fluxes in geostrophic turbulence / B. Nadiga // Philosophical Transactions of the Royal Society A: Mathematical, Physical and Engineering Sciences. — 2008. — Vol. 366, no. 1875. — P. 2489—2508.

47. Regularized, parameter free scale similarity type models for Large Eddy Simulation / M. Klein [et al.] // International Journal of Heat and Fluid Flow. — 2020. — Vol. 81. — P. 108496.

48. *Bouchet, F.* Parameterization of two-dimensional turbulence using an anisotropic maximum entropy production principle / F. Bouchet. — 2003.

49. *Maulik, R.* Dynamic modeling of the horizontal eddy viscosity coefficient for quasigeostrophic ocean circulation problems / R. Maulik, O. San // Journal of Ocean Engineering and Science. — 2016. — Vol. 1, no. 4. — P. 300—324.

50. *Bachman, S. D.* A scale-aware subgrid model for quasi-geostrophic turbulence / S. D. Bachman, B. Fox-Kemper, B. Pearson // Journal of Geophysical Research: Oceans. — 2017. — Vol. 122, no. 2. — P. 1529—1554.

51. *Beck, A. D.* Deep neural networks for data-driven turbulence models / A. D. Beck, D. G. Flad, C.-D. Munz // arXiv preprint arXiv:1806.04482. — 2018.

52. Subgrid modelling for two-dimensional turbulence using neural networks / R. Maulik [et al.] // Journal of Fluid Mechanics. — 2019. — Vol. 858. — P. 122—144.

53. *Stolz, S.* An approximate deconvolution procedure for large-eddy simulation / S. Stolz, N. A. Adams // Physics of Fluids. — 1999. — Vol. 11, no. 7. — P. 1699—1701.

54. Approximate deconvolution large eddy simulation of a barotropic ocean circulation model / O. San [et al.] // Ocean Modelling. — 2011. — Vol. 40, no. 2. — P. 120—132.

55. *Maulik*, *R.* A neural network approach for the blind deconvolution of turbulent flows / R. Maulik, O. San // Journal of Fluid Mechanics. — 2017. — Vol. 831. — P. 151—181.

56. *Berloff*, *P. S.* Random-forcing model of the mesoscale oceanic eddies / P. S. Berloff // Journal of Fluid Mechanics. — 2005. — Vol. 529. — P. 71—95.

57. On data-driven augmentation of low-resolution ocean model dynamics / E. Ryzhov [et al.] // Ocean Modelling. — 2019. — Vol. 142. — P. 101464.

58. *Majda*, *A. J.* A mathematical framework for stochastic climate models / A. J. Majda, I. Timofeyev, E. Vanden Eijnden // Communications on Pure and Applied Mathematics: A Journal Issued by the Courant Institute of Mathematical Sciences. — 2001. — Vol. 54, no. 8. — P. 891—974.

59. *Grooms*, *I.* Stochastic superparameterization in quasigeostrophic turbulence / I. Grooms, A. J. Majda // Journal of Computational Physics. — 2014. — Vol. 271. — P. 78—98.

60. *Frank*, *J. E.* Stochastic homogenization for an energy conserving multi-scale toy model of the atmosphere / J. E. Frank, G. A. Gottwald // Physica D: Nonlinear Phenomena. — 2013. — Vol. 254. — P. 46—56.

61. *Gugole*, *F.* Numerical development and evaluation of an energy conserving conceptual stochastic climate model / F. Gugole, C. L. Franzke // Mathematics of climate and weather forecasting. — 2019. — Vol. 5, no. 1. — P. 45—64.

62. *Gugole*, *F.* Spatial Covariance Modeling for Stochastic Subgrid-Scale Parameterizations Using Dynamic Mode Decomposition / F. Gugole, C. Franzke. — 2019.

63. New trends in ensemble forecast strategy: uncertainty quantification for coarse-grid computational fluid dynamics / V. Resseguier [et al.] // Archives of Computational Methods in Engineering. — 2020. — P. 1—82.

64. *Cooper*, *F. C.* Optimisation of an idealised primitive equation ocean model using stochastic parameterization / F. C. Cooper // Ocean Modelling. — 2017. — Vol. 113. — P. 187—200.

65. *Mana*, *P. P.* Toward a stochastic parameterization of ocean mesoscale eddies / P. P. Mana, L. Zanna // Ocean Modelling. — 2014. — Vol. 79. — P. 1—20.

66. Scale-aware deterministic and stochastic parametrizations of eddy-mean flow interaction / L. Zanna [et al.] // Ocean Modelling. — 2017. — Vol. 111. — P. 66—80.

67. *Schumann*, *U.* Stochastic backscatter of turbulence energy and scalar variance by random subgrid-scale fluxes / U. Schumann // Proceedings of the Royal Society of London. Series A: Mathematical and Physical Sciences. — 1995. — Vol. 451, no. 1941. — P. 293—318.

68. *Jansen*, *M. F.* Parameterizing subgrid-scale eddy effects using energetically consistent backscatter / M. F. Jansen, I. M. Held // Ocean Modelling. — 2014. — Vol. 80. — P. 36—48.

69. *Lesieur*, *M.* Turbulence in Fluids / M. Lesieur. — Springer Netherlands, 2008.

70. *Leslie*, *D.* The application of turbulence theory to the formulation of subgrid modelling procedures / D. Leslie, G. Quarini // Journal of fluid mechanics. — 1979. — Vol. 91, no. 1. — P. 65—91.

71. *Leith*, *C.* Stochastic backscatter in a subgrid-scale model: Plane shear mixing layer / C. Leith // Physics of Fluids A: Fluid Dynamics. — 1990. — Vol. 2, no. 3. — P. 297—299.

72. *Mason*, *P. J.* Stochastic backscatter in large-eddy simulations of boundary layers / P. J. Mason, D. J. Thomson // Journal of Fluid Mechanics. — 1992. — Vol. 242. — P. 51—78.

73. *Weinbrecht*, *S.* Stochastic backscatter for cloud-resolving models. Part I: Implementation and testing in a dry convective boundary layer / S. Weinbrecht, P. J. Mason // Journal of the atmospheric sciences. — 2008. — Vol. 65, no. 1. — P. 123—139.

74. *Zidikheri*, *M. J.* Stochastic subgrid parameterizations for simulations of atmospheric baroclinic flows / M. J. Zidikheri, J. S. Frederiksen // Journal of the atmospheric sciences. — 2009. — Vol. 66, no. 9. — P. 2844—2858.

75. *Kitsios*, *V.* Stochastic Subgrid Turbulence Parameterisation of Eddy-Eddy, Eddy-Meanfield, Eddy-Topographic and Meanfield-Meanfield Interactions in the Atmosphere / V. Kitsios, J. Frederiksen // Australasian Fluid Mechanics Conference, 2018. — Australasian Fluid Mechanics Society. 2018.

76. *Shutts*, *G.* A kinetic energy backscatter algorithm for use in ensemble prediction systems / G. Shutts // Quarterly Journal of the Royal Meteorological Society: A journal of the atmospheric sciences, applied meteorology and physical oceanography. — 2005. — Vol. 131, no. 612. — P. 3079—3102.

77. A spectral stochastic kinetic energy backscatter scheme and its impact on flow-dependent predictability in the ECMWF ensemble prediction system / J. Berner [et al.] // Journal of the Atmospheric Sciences. — 2009. — Vol. 66, no. 3. — P. 603—626.

78. *Zurita-Gotor*, *P.* Kinetic energy-conserving hyperdiffusion can improve low resolution atmospheric models / P. Zurita-Gotor, I. M. Held, M. F. Jansen // Journal of Advances in Modeling Earth Systems. — 2015. — Vol. 7, no. 3. — P. 1117—1135.

79. Ocean kinetic energy backscatter parametrizations on unstructured grids: Impact on mesoscale turbulence in a channel / S. Juricke [et al.] // Ocean Modelling. — 2019. — Vol. 138. — P. 51—67.

80. *Held*, *I. M.* A proposal for the intercomparison of the dynamical cores of atmospheric general circulation models / I. M. Held, M. J. Suarez // Bulletin of the American Meteorological society. — 1994. — Vol. 75, no. 10. — P. 1825—1830.

81. Ocean kinetic energy backscatter parametrization on unstructured grids: Impact on global eddy-permitting simulations / S. Juricke [et al.] // Journal of Advances in Modeling Earth Systems. — 2020. — Vol. 12, no. 1. — e2019MS001855.

82. Energy budget-based backscatter in an eddy permitting primitive equation model / M. F. Jansen [et al.] // Ocean Modelling. — 2015. — Vol. 94. — P. 15—26.

83. *Berloff*, *P.* Dynamically consistent parameterization of mesoscale eddies. Part III: Deterministic approach / P. Berloff // Ocean Modelling. — 2018. — Vol. 127. — P. 1—15.

84. *Grooms*, *I.* Numerical schemes for stochastic backscatter in the inverse cascade of quasigeostrophic turbulence / I. Grooms, Y. Lee, A. J. Majda // Multiscale Modeling & Simulation. — 2015. — Vol. 13, no. 3. — P. 1001—1021.

85. NEMO ocean engine / G. Madec [et al.]. — 2015.

86. *Баклановская*, *В. Ф.* Исследование метода сеток для двумерных уравнений типа Навье–Стокса с неотрицательной вязкостью. II / В. Ф. Баклановская // Журнал вычислительной математики и математической физики. — 1984. — Vol. 24, no. 12. — P. 1827—1841.

87. *Юдович*, *В. И.* Нестационарные течения идеальной несжимаемой жидкости / В. И. Юдович // Журнал вычислительной математики и математической физики. — 1963. — Vol. 3, no. 6. — P. 1032—1066.

88. *Marchioro*, *C.* Mathematical theory of incompressible nonviscous fluids. Vol. 96 / C. Marchioro, M. Pulvirenti. — Springer Science & Business Media, 2012.

89. *Robert*, *R.* On the statistical mechanics of 2D Euler equation / R. Robert // Communications in Mathematical Physics. — 2000. — Vol. 212, no. 1. — P. 245—256.

90. *Dritschel*, *D. G.* On the late-time behaviour of a bounded, inviscid two-dimensional flow / D. G. Dritschel, W. Qi, J. Marston // Journal of Fluid Mechanics. — 2015. — Vol. 783. — P. 1—22.

91. *Qi*, *W.* Hyperviscosity and statistical equilibria of Euler turbulence on the torus and the sphere / W. Qi, J. Marston // Journal of Statistical Mechanics: Theory and Experiment. — 2014. — Vol. 2014, no. 7. — P07020.

92. *Kraichnan*, *R. H.* Statistical dynamics of two-dimensional flow / R. H. Kraichnan // Journal of Fluid Mechanics. — 1975. — Vol. 67, no. 1. — P. 155—175.

93. *Abramov*, *R. V.* Statistically relevant conserved quantities for truncated quasi-geostrophic flow / R. V. Abramov, A. J. Majda // Proceedings of the National Academy of Sciences. — 2003. — Vol. 100, no. 7. — P. 3841—3846.

94. *Dubinkina*, *S.* Statistical mechanics of Arakawa's discretizations / S. Dubinkina, J. Frank // Journal of Computational Physics. — 2007. — Vol. 227, no. 2. — P. 1286—1305.

95. *Venaille*, *A.* Violent relaxation in two-dimensional flows with varying interaction range / A. Venaille, T. Dauxois, S. Ruffo // Physical Review E. — 2015. — Vol. 92, no. 1. — P. 011001.

96. *Обухов*, *А. М.* Об интегральных инвариантах в системах гидродинамического типа / А. М. Обухов // Доклады Академии наук. Vol. 184. — Российская академия наук. 1969. — P. 309—312.

97. *Дымников, В. П.* Устойчивость и предсказуемость крупномасштабных атмосферных процессов / В. П. Дымников // М.: ИВМ РАН. — 2007. — Vol. 283.

98. *Salmon, R.* Lectures on geophysical fluid dynamics / R. Salmon. — Oxford University Press, 1998.

99. *Дымников, В.* Информационная энтропия и локальные показатели Ляпунова баротропной атмосферной циркуляции / В. Дымников, Е. Казанцев, В. Харин // Изв. РАН. Физика атмосферы и океана. — 1992. — Vol. 28, no. 6. — P. 563.

100. *Bouchet, F.* Invariant measures of the 2D Euler and Vlasov equations / F. Bouchet, M. Corvellec // Journal of Statistical Mechanics: Theory and Experiment. — 2010. — Vol. 2010, no. 08. — P08021.

101. *Miller, J.* Statistical mechanics of Euler equations in two dimensions / J. Miller // Physical review letters. — 1990. — Vol. 65, no. 17. — P. 2137.

102. *Lisman, J.* Note on the generation of most probable frequency distributions / J. Lisman, M. v. Zuylen // Statistica Neerlandica. — 1972. — Vol. 26, no. 1. — P. 19—23.

103. *Kozlov, V.* Gibbs ensembles and nonequilibrium statistical mechanics / V. Kozlov // RKhD, Moscow. — 2008.

104. *Turkington, B.* Statistical equilibrium measures and coherent states in two-dimensional turbulence / B. Turkington // Communications on Pure and Applied Mathematics: A Journal Issued by the Courant Institute of Mathematical Sciences. — 1999. — Vol. 52, no. 7. — P. 781—809.

105. *Arakawa, A.* Design of the UCLA general circulation model / A. Arakawa. — 1972.

106. *Brown, D.* Accurate projection methods for the incompressible Navier–Stokes equations / D. Brown, R. Cortez, M. Minion. — 2001.

107. *Diansky, N.* Sigma model of global ocean circulation and its sensitivity to variations in wind stress / N. Diansky, A. Bagno, V. Zalesny // Izvestiya. Atmospheric and Oceanic Physics. — 2002. — Vol. 38, no. 4. — P. 477—494.

108. Fully conservative higher order finite difference schemes for incompressible flow / Y. Morinishi [et al.] // Journal of computational physics. — 1998. — Vol. 143, no. 1. — P. 90—124.

109. Simulation of the present-day climate with the climate model INMCM5 / E. Volodin [et al.] // Climate dynamics. — 2017. — Vol. 49, no. 11/12. — P. 3715—3734.

110. *Arakawa*, *A.* Computational design of the basic dynamical processes of the UCLA general circulation model / A. Arakawa, V. R. Lamb // General circulation models of the atmosphere. — 1977. — Vol. 17, Supplement C. — P. 173—265.

111. *Hortal*, *M.* The development and testing of a new two-time-level semi-Lagrangian scheme (SETTLS) in the ECMWF forecast model / M. Hortal // Quarterly Journal of the Royal Meteorological Society: A journal of the atmospheric sciences, applied meteorology and physical oceanography. — 2002. — Vol. 128, no. 583. — P. 1671—1687.

112. *Tolstykh*, *M.* Global semi-Lagrangian numerical weather prediction model / M. Tolstykh // FOP, Obninsk, Moscow, Russia. — 2010. — P. 111.

113. *Williamson*, *D. L.* Two-dimensional semi-Lagrangian transport with shape-preserving interpolation / D. L. Williamson, P. J. Rasch // Monthly Weather Review. — 1989. — Vol. 117, no. 1. — P. 102—129.

114. *Purser*, *R.* An efficient interpolation procedure for high-order three-dimensional semi-Lagrangian models / R. Purser, L. Leslie // Monthly Weather Review. — 1991. — Vol. 119, no. 10. — P. 2492—2498.

115. *Shashkin*, *V.* 3D conservative cascade semi-Lagrangian transport scheme using reduced latitude–longitude grid (CCS-RG) / V. Shashkin, R. Fadeev, M. Tolstykh // Journal of Computational Physics. — 2016. — Vol. 305. — P. 700—721.

116. *McDonald*, *A.* Accuracy of multiply-upstream, semi-Lagrangian advective schemes / A. McDonald // Monthly Weather Review. — 1984. — Vol. 112, no. 6. — P. 1267—1275.

117. *Nair*, *R. D.* Efficient conservative global transport schemes for climate and atmospheric chemistry models / R. D. Nair, J. S. Scroggs, F. H. Semazzi // Monthly weather review. — 2002. — Vol. 130, no. 8. — P. 2059—2073.

118. *Xiu*, *D.* A semi-Lagrangian high-order method for Navier–Stokes equations / D. Xiu, G. E. Karniadakis // Journal of computational physics. — 2001. — Vol. 172, no. 2. — P. 658—684.

119. *Verma*, *S.* An improved bounded semi-Lagrangian scheme for the turbulent transport of passive scalars / S. Verma, Y. Xuan, G. Blanquart // Journal of Computational Physics. — 2014. — Vol. 272. — P. 1—22.

120. Large eddy simulation of two-dimensional isotropic turbulence / S. Sukoriansky [et al.] // Journal of scientific computing. — 1996. — Vol. 11, no. 1. — P. 13—45.

121. *Nadiga*, *B.* Alternating zonal jets and energy fluxes in barotropic wind-driven gyres / B. Nadiga, D. Straub // Ocean Modelling. — 2010. — Vol. 33, no. 3/4. — P. 257—269.

122. *Kitsios*, *V.* Scaling laws for parameterisations of subgrid eddy–eddy interactions in simulations of oceanic circulations / V. Kitsios, J. S. Frederiksen, M. Zidikheri // Ocean Modelling. — 2013. — Vol. 68. — P. 88—105.

123. *Deardorff*, *J. W.* A numerical study of three-dimensional turbulent channel flow at large Reynolds numbers / J. W. Deardorff // Journal of Fluid Mechanics. — 1970. — Vol. 41, no. 2. — P. 453—480.

124. *Laval*, *J.-P.* Nonlocality of interaction of scales in the dynamics of 2D incompressible fluids / J.-P. Laval, B. Dubrulle, S. Nazarenko // Physical review letters. — 1999. — Vol. 83, no. 20. — P. 4061.

125. *Lund*, *T.* On the use of discrete filters for large eddy simulation / T. Lund // Annual Research Briefs. — 1997. — P. 83—95.

126. *Von Storch*, *H.* Statistical analysis in climate research / H. Von Storch, F. W. Zwiers. — Cambridge university press, 2001.

127. *Alvelius*, *K.* Random forcing of three-dimensional homogeneous turbulence / K. Alvelius // Physics of Fluids. — 1999. — Vol. 11, no. 7. — P. 1880—1889.

128. *Shutts*, *G.* A stochastic convective backscatter scheme for use in ensemble prediction systems / G. Shutts // Quarterly Journal of the Royal Meteorological Society. — 2015. — Vol. 141, no. 692. — P. 2602—2616.

129. *Kraichnan*, *R. H.* Eddy viscosity in two and three dimensions / R. H. Kraichnan // Journal of the atmospheric sciences. — 1976. — Vol. 33, no. 8. — P. 1521—1536.

130. *Boffetta*, *G.* Evidence for the double cascade scenario in two-dimensional turbulence / G. Boffetta, S. Musacchio // Physical Review E. — 2010. — Vol. 82, no. 1. — P. 016307.

131. *Galewsky*, *J.* An initial-value problem for testing numerical models of the global shallow-water equations / J. Galewsky, R. K. Scott, L. M. Polvani // Tellus A: Dynamic Meteorology and Oceanography. — 2004. — Vol. 56, no. 5. — P. 429—440.

132. *Griffies*, *S. M.* Biharmonic friction with a Smagorinsky-like viscosity for use in large-scale eddy-permitting ocean models / S. M. Griffies, R. W. Hallberg // Monthly Weather Review. — 2000. — Vol. 128, no. 8. — P. 2935—2946.

133. *Nastrom*, *G.* A climatology of atmospheric wavenumber spectra of wind and temperature observed by commercial aircraft / G. Nastrom, K. S. Gage // Journal of the atmospheric sciences. — 1985. — Vol. 42, no. 9. — P. 950—960.

134. *Arnold*, *L.* Stochastic differential equations / L. Arnold. — New York, 1974.

135. Modifications of gyre circulation by sub-mesoscale physics / M. Lévy [et al.] // Ocean Modelling. — 2010. — Vol. 34, no. 1/2. — P. 1—15.

136. *Eden*, *C.* Towards a mesoscale eddy closure / C. Eden, R. J. Greatbatch // Ocean Modelling. — 2008. — Vol. 20, no. 3. — P. 223—239.

137. *Carati*, *D.* On the representation of backscatter in dynamic localization models / D. Carati, S. Ghosal, P. Moin // Physics of Fluids. — 1995. — Vol. 7, no. 3. — P. 606—616.

138. *Schumann*, *U.* The countergradient heat flux in turbulent stratified flows / U. Schumann // Nuclear engineering and design. — 1987. — Vol. 100, no. 3. — P. 255—262.

139. *Dwivedi*, *S.* Energetically consistent scale-adaptive stochastic and deterministic energy backscatter schemes for an atmospheric model / S. Dwivedi, C. L. Franzke, F. Lunkeit // Quarterly Journal of the Royal Meteorological Society. — 2019. — Vol. 145, no. 725. — P. 3376—3386.

140. *Thuburn*, *J.* Cascades, backscatter and conservation in numerical models of two-dimensional turbulence / J. Thuburn, J. Kent, N. Wood // Quarterly Journal of the Royal Meteorological Society. — 2014. — Vol. 140, no. 679. — P. 626—638.

141. Energy budget-based backscatter in a shallow water model of a double gyre basin / M. Klöwer [et al.] // Ocean Modelling. — 2018. — Vol. 132. — P. 1—11.

142. Toward an energetically consistent, resolution aware parameterization of ocean mesoscale eddies / M. F. Jansen [et al.] // Journal of Advances in Modeling Earth Systems. — 2019. — Vol. 11, no. 8. — P. 2844—2860.

143. Geographical variability of the first baroclinic Rossby radius of deformation / D. B. Chelton [et al.] // Journal of Physical Oceanography. — 1998. — Vol. 28, no. 3. — P. 433—460.

144. *Kjellsson*, *J.* The impact of horizontal resolution on energy transfers in global ocean models / J. Kjellsson, L. Zanna // Fluids. — 2017. — Vol. 2, no. 3. — P. 45.

145. Scales, growth rates, and spectral fluxes of baroclinic instability in the ocean / R. Tulloch [et al.] // Journal of Physical Oceanography. — 2011. — Vol. 41, no. 6. — P. 1057—1076.

146. *Schlösser*, *F.* Diagnosing the energy cascade in a model of the North Atlantic / F. Schlösser, C. Eden // Geophysical research letters. — 2007. — Vol. 34, no. 2.

147. Nonlinear cascades of surface oceanic geostrophic kinetic energy in the frequency domain / B. K. Arbic [et al.] // Journal of Physical Oceanography. — 2012. — Vol. 42, no. 9. — P. 1577—1600.

148. *Sasaki*, *H.* SSH wavenumber spectra in the North Pacific from a high-resolution realistic simulation / H. Sasaki, P. Klein // Journal of Physical Oceanography. — 2012. — Vol. 42, no. 7. — P. 1233—1241.

149. *Deusebio*, *E.* The route to dissipation in strongly stratified and rotating flows / E. Deusebio, A. Vallgren, E. Lindborg // Journal of Fluid Mechanics. — 2013. — Vol. 720. — P. 66—103.

150. *Di Leoni*, *P. C.* Inferring flow parameters and turbulent configuration with physics-informed data assimilation and spectral nudging / P. C. Di Leoni, A. Mazzino, L. Biferale // Physical Review Fluids. — 2018. — Vol. 3, no. 10. — P. 104604.

151. *Di Leoni*, *P. C.* Synchronization to Big Data: Nudging the Navier-Stokes Equations for Data Assimilation of Turbulent Flows / P. C. Di Leoni, A. Mazzino, L. Biferale // Physical Review X. — 2020. — Vol. 10, no. 1. — P. 011023.

152. *Fox*, *D. G.* Inviscid dynamics of two-dimensional turbulence / D. G. Fox, S. A. Orszag // The Physics of Fluids. — 1973. — Vol. 16, no. 2. — P. 169—171.

153. *Gama, S.* The two-dimensional Navier-Stokes-Kuramoto-Sivashinsky equation on the connection machine / S. Gama, U. Frisch // Computing Systems in Engineering. — 1995. — Vol. 6, no. 4/5. — P. 325—329.

154. *Gao, P.* Numerical Simulation of Stochastic Kuramoto-Sivashinsky Equation / P. Gao, C. Cai, X. Liu // Journal of Applied Mathematics and Physics. — 2018. — Vol. 6, no. 11. — P. 2363—2369.

155. *Kalogirou, A.* An in-depth numerical study of the two-dimensional Kuramoto–Sivashinsky equation / A. Kalogirou, E. E. Keaveny, D. T. Papageorgiou // Proceedings of the Royal Society A: Mathematical, Physical and Engineering Sciences. — 2015. — Vol. 471, no. 2179. — P. 20140932.